Master of Science Thesis

Characterisation of damage in composite materials using infrared thermography

NLR

Royal Netherlands Aerospace Centre

UT

University of Twente

UNIVERSITY OF TWENTE.

Author:

L.R. Kalter, BSc
University of Twente
Mechanical Engineering
l.r.kalter@student.utwente.nl

Under supervision of:

Ir. J.S. Hwang
Netherlands Aerospace Centre - Aerospace Verhicles; Gas Turbines & Structural Integrity

Dr. ir. D. Di Maio
University of Twente - Dynamics Based Maintenance

Prof. dr. ir. T. Tinga
University of Twente - Dynamics Based Maintenance

August 12, 2019

Acknowledgements

Before you lies the thesis *Characterisation of damage in composite materials using infrared thermography*. This report is a thorough study into the characterisation capabilities of the different optical IR thermography methods. It is a result of my graduate internship at the Royal Netherlands Aerospace Center (NLR) in Marknesse. The report has been written to fulfil the graduation requirements of the master Mechanical Engineering at the University of Twente. I was engaged in conducting research and writing this thesis from February to September 2019.

This research is supported by the Royal Netherlands Aerospace Center (NLR). Founded in 1919 as *Rijksstudiedienst voor de luchtvaart* (RSL), the goal of the NLR is to increase safety in aviation. While in 1919 the focus was on military aviation, the rapid upswing of civil aviation lead to the the widening of the NLR research [1]. The uprising of the modern computer resulted in new possibilities for the NLR, using all sorts of simulations for scientific research in the national aviation industry. In the twenty-first century, NLR focusses on making the aviation and aerospace industry more sustainable, safer and efficient.

I would like to thank my supervisors Dario di Mario and Tiedo Tinga from the University of Twente and Jason Hwang from the Royal Netherlands Aerospace Center for their support, availability and willingness to provide feedback and help with questions.

I would also like to thank Jacco Platenkamp and Arnoud Bosch for helping me with the experiments in the optical lab of the Aerospace Vehicles Test House. Lastly, I would like to thank my girlfriend for her support during my graduate internship.

L.R. Kalter, BSc
Marknesse, August 2019

Abstract

The Non Destructive Testing (NDT) of large surface composite aerostructures is a very time consuming but critical process. Optical thermography is a relatively fast method for large surface inspection. This method is currently applied as first quick scan after which more detailed inspections are performed with different NDT methods to determine the defect properties and severity. This research is conducted to determine the defect characterisation capabilities of optical thermography as a NDT method for CFRP aerostructures.

In this research firstly, the current state of optical thermography methods is investigated. Two optical thermography methods have been tested experimentally and are investigated further using numerical simulations. Secondly, characteristics in the thermography results that can be used for the identification of the defect properties are identified. Thirdly, all factors that can influence the characteristics of the thermography results are determined. Experiments and numerical simulations are used to determine the sensitivity of the characteristics to these factors One-Factor-at-A-Time (OFAT). Finally, a window of possible values of the characteristics is obtained for three different defects; teflon coated glass, kapton and an air filled delamination. The obtained value windows can be used for defect characterisation.

The thermography methods are divided in two categories; frequency domain analysis thermography and pulse compression analysis thermography. The first applies Fast Fourier Transform (FFT) on the temperature signal of each pixel to obtain the phase at a certain frequency. The phase of a non defect area is then subtracted from the phase of a defect area to obtain the phase difference. This operation is performed for a range of frequencies resulting in the phase difference as a function of the frequency. Four characteristics are identified in this data; the peak phase difference, the peak phase frequency, the blind frequency and the phase transition frequency.

The second category applies Cross Correlation (CC) on the temperature signal of each pixel to obtain the cross correlation value as a function of the time delay. The difference in the normalized peak cross correlation value of the defect area and a non defect area is the first characteristic of this method. The second characteristic is the difference in time delay at which the correlation peak occurs for the defect and non defect area. The third characteristic is the cross correlation phase.

The influence of different heat signals, cameras and lamps on the characteristics is determined firstly after which the influence of the surface, the material and the defect are determined. This process is performed for both thermography method categories.

Two different NDT application scenarios are considered; in production and Maintenance Repair and Overhaul (MRO). In the composite production industry, the information on potential defects (foil and tape inclusions), the thickness and the properties of these materials are known. Even without detailed knowledge on the composite material properties, this makes characterisation of defects with optical thermography possible for the composite industry.

In the MRO industry, the knowledge on material properties of the composite is often limited. The type of sub surface defect expected in MRO inspections are delaminations of which the thickness can vary. However, characterisation of delaminations is possible with frequency domain thermography since the blind frequency characteristic is only marginally influenced by the air gap thickness. The thickness and depth of an air filled delamination can thus be determined within a range.

In conclusion, it can be stated that the best suited method for defect characterisation is frequency domain analysis thermography. The numerical results described in this report allow for decisive characterisation of sub surface defects with the aid of optical thermography without detailed knowledge on the composite material properties but requires knowledge on the potential defects in the sample. The greatest uncertainty in the characterisation of defects with the aid of optical thermography is the lack of detailed knowledge on the composite material properties, which results in a rather large spread of the possible thermography results for a certain defect.

Keywords: *Composite, NDT, non destructive testing, thermography, FFT, pulse compression, CC, IR, infrared, FEM, thermal analysis, heat, thermal waves, sensitivity analysis, defect characterisation, NLR, UT*

Contents

List of Figures

Nomenclature

Acronyms

2D	Two Dimensional
3D	Three Dimensional
ASTM	American Society for Testing and Materials
AVTH	Aerospace Vehicles Test House
BCTWI	Barker Coded Thermal Wave Imaging
BVID	Barely Visible Impact Damage
CC	Cross Correlation
CFRP	Carbon Fibre Reinforced Plastics
DFMTWI	Digital Frequency Modulated Thermal Wave Imaging
DFT	Discrete Fourier Transform
FEM	Finite Element Method
FFT	Fast Fourier Transform
FMTWI	Frequency Modulated Thermal Wave Imaging
GFRP	Glass Fibre Reinforced Plastics
IR	Infrared Radiation
IRLT	Infrared Radiation Lock-in Thermography
LT	Lock-in Thermography
LWIR	Long Wavelength Infrared Radiation
MRO	Maintenance Repair and Overhaul
MWIR	Medium Wavelength Infrared Radiation
NDE	Non Destructive Evaluation
NDI	Non Destructive Inspection
NDT	Non Destructive Testing
NIR	Near Infrared Radiation
NLR	Royal Netherlands Aerospace Center
OFAT	One-Factor-at-A-Time
POD	Probability Of Detection
PPT	Pulsed Phase Thermography
PSL	Peak Sidelobe Level
PT	Pulsed Thermography

QNDE	Quantative Non Destructive Evaluation conference
RDID	Readily Detectable Impact Damage
RGB	Red Green Blue
SNR	Signal to Noise Ratio
SWIR	Short Wavelength Infrared Radiation
VLWIR	Very Long Wavelength Infrared Radiation

Symbols

α	Thermal diffusivity	[m^2/s]
λ	Wavelength (of radiation)	[m]
μ	Penetration depth (or thermal diffusion length)	[m]
ϕ	Initial phase	[rad]
ρ	Mass density	[kg/m^3]
σ_{SB}	Stefan Boltzmann constant	[$Wm^{-2}K^{-4}$]
T	Total time	[s]
τ	Delay time	[s]
φ	Phase	[deg]
A	Amplitude	[K]/[D.I.L.]/[a.u.]
B	Calibrated distance between stereo cameras	[m]
b	Wien's displacement constant	[mK]
C	Material correction factor	[-]
C	Volumetric heat capacity	[J/m^3K]
c	Loss of contrast	[K]/[a.u.]
c_1	First radiation constant	[Wm^2]
c_2	Second radiation constant	[mK]
c_p	Specific heat capacity (at constant pressure)	[J/kgK]
d	Defect depth	[m]
e	Thermal effusivity	[$J/s^{1/2}m^2K$]
E_λ	Spectral blackbody emissive power	[W/m^3]
f	Focal length	[m]
f_0	Starting frequency	[Hz]
f_1	End frequency	[Hz]
f_b	Blind frequency	[Hz]
$g(\tau)$	Cross correlation	[K^2s]/[$(D.I.L.)^2s$]/[a.u.]
$H(\omega)$	Fourier transform of the perceived signal	[Ks]/[(D.I.L.)s]/[a.u.]

$h(t)$	Perceived thermal wave signal	[K]/[D.I.L.]/[a.u.]
$I(x, y, z, t)$	Rate of internal heat generation	[W/m^3]
I_0	Heat flux	[W/m^2]
k	Thermal conductivity	[W/mK]
k_l	Thermal conductivity in the lateral direction	[W/mK]
k_t	Thermal conductivity in the through thickness direction	[W/mK]
$P(x, y, z)$	Position in three dimensions	[m]
q	Complex wave number	[i/m]
R	Reflection coefficient	[-]
$S(\omega)$	Fourier transform of the reference signal	[Ks]/[(D.I.L.)s]/[a.u.]
$s(t)$	Reference signal	[K]/[D.I.L.]/[a.u.]
S_i	Data point i	[K]/[D.I.L.]/[a.u.]
T	Absolute temperature	[K]
t	Time	[s]
x_i	Position of camera i	[m]
Z	Distance to point P(x,y,z)	[m]

Chapter 1: Introduction

In this chapter an introduction to the executed research is presented. To create an overview of testing for aerospace applications, section 1.1 presents an overview of damage types and Non Destructive Testing (NDT) methods for damage detection in the aerospace industry. Section 1.2 presents the scientific context of this research. Section 1.3 describes the objective of this thesis based on the scientific context and gaps in the knowledge on NDT. The objective is formulated in a research question in section 1.4. This chapter concludes with an outline of the remaining chapters in section 1.5.

1.1 Non Destructive Testing

Non destructive testing (NDT) can be described as a term for methods that are used to detect certain features in an object without changing the integrity or properties of the object irreversibly. In the field of aeronautical applications, the features sought after are defects, abnormalities or imperfections in components and structures [2].

In literature, the terms Non Destructive Investigation (NDI), Testing (NDT) and Evaluation (NDE) are commonly used as synonyms [3]. However, the three terms can be interpreted differently. NDI and NDT have an overlapping definition since both terms refer to qualitative measurements, but NDI is most commonly referred to for visual inspection methods. NDT is a wider term that includes the use of a range of different methods to test if an object has certain features. NDE is mostly referred to when the test results are quantitatively evaluated to determine characteristics of the detected features such as defect type, shape and depth. NDE also involves the making of the final judgement based on the test results. In the definition of NDT given by The American Society for Testing and Materials (ASTM), NDT also includes the evaluation of the test results: "*NDT is the development and application of technical methods to examine materials or components in ways that do not impair future usefulness and serviceability in order to detect, locate, measure and evaluate discontinuities, defects and other imperfections; assess integrity, properties and composition; and measure geometrical characteristics.*" [4]. In this report, it is chosen to use the term NDT as defined by the ASTM. The terms NDI and NDE will therefore not be used in this report.

NDT is an important part of the modern aviation and aerospace industry since it plays a crucial role in the safety of structures. One of the primary objectives of the aerospace industry is to increase fuel efficiency of aircrafts. To achieve this, weight reduction if one of the main design goals. This result in the trend of increasing application of Carbon and Glass Fibre Reinforced Polymers as can be seen in Figure 1.1 [5].

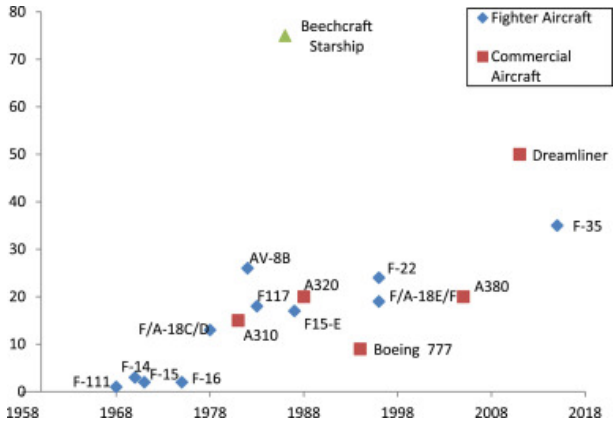

Figure 1.1: *Percentage of aircraft mass comprised of composite materials (in initial configuration) [5].*

Composite materials consist of a matrix material with a reinforcing component. Composite materials are either constructed as solid laminate or a sandwich panel consisting of a low-density core material sandwiched between the two thin (1 - 2mm) panels [2]. The performance of fibre reinforced polymers is greatly influenced by abnormalities in the material. NDT methods are used to look for these abnormalities in the material. Small defects can be acceptable depending on their nature and location. Depending on the size of the defect, it is decided whether or not to reject the object. The type of abnormalities that are potentially present in composite components is dependent on the life stage of the components. The component life can be divided in the production stage and the in-service stage. Aerospace structures are subject to extensive testing and evaluation during both production and the service life [2]. The most common defects obtained during production are resin-starved or resin-rich areas and cavities in the material as a result of entrapment of gasses or material inclusions such as Nylon or other tapes and foils [2].

Other types of defects occur during the service life of a component as a result of exposure to extreme environments, overloading and impact. The properties of composite materials are susceptible to degradation due to exposure to for example certain fluids, engine exhausts, fire and lightning strikes. The exposure to extreme environments may not be visible but can result in seriously degraded properties [2]. Overloading of a composite component may result in crack initiation or disbonding, while impacts cause different types of damage depending on the impact energy.

Composite materials are in general sensitive to impact [2]. Impacts can be caused by, for example, tool drops, flying debris on runways, bird strikes and hail storms. All of these cases result in different impact energies. Depending on the impact energy, impact damages range from easily identifiable holes in the surface to subsurface defects that are barely visible at the surface. In some cases the surface dent caused by low and medium energy impacts is visible directly after the damage is obtained but may become invisible over time [6]. The severity of the damage caused by an impact is dependent on the object shape and size, the impact energy, the laminate properties and thickness. Even a low energy impact (typically smaller than 40 J, see [7]) may result in fibre fracture, matrix cracking, delamination or disbonding of the sheet from the core material [2][8][9]. Although invisible from the outer surface, the internal damage can significantly influence the structural strength [2]. Medium energy impacts often result in a local surface dent with subsurface delaminations and fractures while high energy impacts can penetrate through the object creating a surface hole. The different types of impact damage in a solid laminate composite material are schematically shown in Figure 1.2.

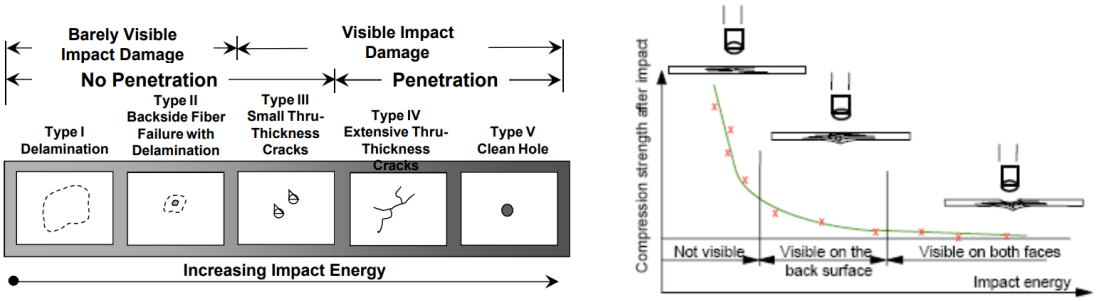

(a) *The type of damage.* (b) *The compression strength after impact.*

Figure 1.2: *Impact damage in composite structures, depending on the impact energy [10].*

Impact damage can be categorized in three categories, the first category is not visible impact damage. This damage can still result in a significant reduction of the strength as can be seen in Figure 1.2b. The second category is Barely Visible Impact Damage (BVID) meaning that this type of damage is very hard or not detectable by general surface inspection. The third category is Clearly Visible Impact Damage (CVID). Although it is hard to define the boundaries of each category, it is commonly defined as the minimum impact damage which is surely detectable by scheduled inspection [11]. Airbus has defined a threshold for this detectability based on the dent depth. The threshold is 1.3 mm surface dent depth for general visual inspection (CVID) while for detailed inspection a surface dent depth of 0.3 mm (BVID) is defined as threshold [11].

The critical size of discontinuities depends heavily on the function and design of the component [4]. Depending on the component and the critical defect type and size, a different NDT method can be applied. Several different methods are available for the testing and detection of defects, each method has its strengths and weaknesses, unfortunately there is no NDT method that is the best for all applications. The results of methods are sometimes combined resulting in a multi domain inspection method, more details on this can be found appendix A. The most commonly used NDT methods are listed below:

- **Visual inspection**: Represents the first step of NDT examination. Has several advantages: simplicity, rapidity, low cost, minimal training and equipment requirements and the possibility to be performed while the part is being used or processed. However, the detection range is limited to the visible areas. Digital 3D scanners are also applied, more details on this technique can be found in appendix B.
- **Liquid penetrant**: Makes use of a bright coloured fluid (the penetrant) that seeps into surface-breaking discontinuities. The visibility of these discontinuities is enhanced by the penetrant after removing the excess penetrant from the surface.
- **Electromagnetic methods**: Uses electromagnetic sensors to detect disturbances caused by abnormalities in the object, in the magnetic field imposed on a conductive material.
- **Ultrasonic methods**: Detects abnormalities based on the transmission or reflection of high frequency sonic waves (bandwidth 0.5-50 Mhz) through an object and measuring the amplitude, frequency and/or time of arrival of the returned echoes.
- **Thermography**: Measures the surface temperatures of an object with an IR camera, combined with heat deposition on the object (active) or without heat deposition (passive). Disturbances in the heat flow caused by subsurface defects can be derived from the surface temperature over time.
- **Acoustic methods**: Uses acoustic waves to detect defects. Ranges from the well-known 'coin-tap' testing to acoustic resonance testing equipment.
- **Radiography**: Makes use of radiation that is passed through an object and is projected onto a recoding medium to detect defects.
- **Shearography**: Uses interference of laser speckle patterns to measure variations in the strain of the surface with cameras.

1.2 Research context

The inspection of aircraft components during and after manufacturing is a critical stage of the manufacturing process. Currently, ultrasonic NDT methods are mostly applied in production facilities to inspect the produced parts. This is a costly and time consuming process. On the other hand, airlines and the Maintenance Repair and Overhaul (MRO) industry have great interest in the automation and improvement of inspection methods for large surfaces to reduce both the planned ground time for periodic inspections and the unplanned ground time caused by for example impact damage.

Periodic inspections of aircrafts in the MRO industry are split in A, B, C and D checks. A lot of NDT is performed during these checks. The manufacturer of the aircraft provides the operator with a schedule for these inspections. The A check is a routine light maintenance consisting of visual inspection and testing of certain systems. This check is performed every 300-600 flight hours and takes approximately 10 hours. The B check is more detailed but is frequently split and integrated in the A and C checks. The C check is a more detailed and labour intensive check including structural inspection of the aircraft and panels. This check is performed every 3000-6000 flight hours or every 18 to 20 months and takes at most a week. The D check is the most time consuming check which requires the airplane to be grounded for 1-2 months after 4-8 years. This check requires a lot of components to be disassembled from the airplane and it is commonly combined with an overhaul of the aircraft. The D check takes up to 50,000 man hours and approximately 2 months to complete, depending on the size of the aircraft. The costs of a D check surpasses one million dollar for most commercial aircrafts [12][13][14].

The occurrence of certain events as a hail storm may result in the airplane being grounded for detailed impact damage inspection. The aircraft is visually inspected and detected damage is measured and evaluated. The administrative activities and more detailed checks required after visual inspection are labour-intensive. This results in very long inspection times (3-5 hours per square meter [15]). Visual inspection is limited to RDID and BVID while impact damage can cause subsurface damage that is not detectable with visual surface inspection. More detailed checks of suspected damage regions are therefore required, this can for example be done using hand-held ultrasonic equipment. Since abnormalities greatly influence the structural integrity and thus the safety, early detection is of great importance. When an abnormality is detected, it can either be accepted when the safety is not compromised or considered a 'defect' when the abnormality is not acceptable. The acceptance and rejection criteria are part of the damage tolerant design philosophy, this philosophy addresses the ability of components and structures to tolerate a certain density of specific damages while maintaining safe operation [4]. Both composite aircraft component manufacturers and the MRO industry are thus interested in fast and reliable inspection of composite parts.

The area of interest of this research is the effective inspection of large surfaces. Most NDT methods require contact with the test object while a contactless method is favourable for large surface inspection since it requires less set-up time and no complicated mounting on the object is required. While most NDT methods focus on a relatively small area and small defects, both visual inspection and thermography are contact-less methods and both methods have the potential to be used to efficiently test large surface areas. These methods complement each other in the way that visual inspection is able to detect surface abnormalities while thermography is able to detect subsurface abnormalities. These methods are suitable for typical thin skin-stiffener aerospace structures.

The possibilities for combining computerized visual inspection and thermography have been investigated, see [16]. Computerized visual inspection can be used to detect defects with a surface dent or penetration. Three dimensional data acquisition is far evolved over the past two decades. Several techniques are available to effectively acquire a three-dimensional geometry. An overview of the recent developments in three dimensional data acquisition can be found in appendix B. Combining three dimensional data with thermography requires a lot of work to implement both methods efficiently. However, commercial software is available to map the two-dimensional thermography data on the three-dimensional geometry.

Thermography is an extensively researched field. Thermography is applied in numerous scientific fields including thermo-fluid dynamics, medicine, agriculture, building inspection, inspection of electrical components and NDT [17][18]. Thermography can be performed passively or actively with a heat source to actively deposit heat on the test object. Passive thermography is often applied to objects that generate heat internally such as electrical components. Aerospace structures often require an external heat source to generate sufficient temperature differences. A collection of active thermography methods have been developed; Pulsed Thermography (PT), Pulsed Phase thermography (PPT), Lock in thermography (LT), Frequency Modulated Thermal Wave Imaging (FMTWI) and Barker Coded Thermal Wave imaging (BCTWI) [2][19][20]. The thermography methods differ in the type of signal used for the heat deposition and the processing method of the perceived temperature signal. This results in different depth ranges and detectability.

The current state of work on optical thermography does not offer an adequate method for quantifying the detected abnormalities. The quantitative evaluation of thermography data is the biggest challenge in developing an effective multi domain inspection method using both 3D data acquisition and thermography. Common practice is to perform thermography measurements to locate defects and use other NDT methods to characterize the defect. The characterization of defects with thermography requires further attention. The characterisation consists of determining the (depth)position, dimensions and type of defect. This information is very useful in deciding whether the component needs repair or replacement and in case of reparation, to determine how to repair the defect.

1.3 Research objective

Thermography is mainly applied as a quick method to locate subsurface defects, after which another NDT method such as ultrasonic scanning is used for defect characterisation. This characterisation consists of determining all the properties of the defect including the material, lateral size, thickness and depth location. The identified gap in thermography research is the characterisation of defects. Characterisation of defects with thermography enables the user to determine the nature and severity of a defect without having to apply other NDT methods on the sample.

The research objective is to determine the possibilities of using optical thermography to characterise defects in Carbon Fibre Reinforced Plastic (CFRP) aerostructures. This requires exploration of the characterisation capabilities of thermographic imaging techniques for both production and in-situ inspection of composite aerospace structures.

As mentioned in section 1.1, the type of damages expected in a production and in-situ inspection are different. Also the environment and conditions under which these inspections are performed are different. The first types of defects are found in a controlled production environment while the second type of defects are found in the field during MRO inspection. Although both types of defects can occur within the same type of components, these types of defects are considered separately in this research since the conditions and knowledge on the inspected parts differ between the two environments.

1.4 Research questions

Based on the research objective described in section 1.3, the following main research question is formulated:

How and to what extend can damage in aerospace composite materials be characterised with the aid of optical thermography?

In order to answer this question, several subquestions have to be answered first, these questions are listed below:

- *What is the influence of the (partly unknown) composite material properties on the thermography results?*
- *What is the influence of the different types of defects on the thermography results?*
- *What is the influence of noise on the thermography results?*
- *Which optical thermography method is the most conclusive in determining defect characters?*

1.5 Research outline

The current state of thermography techniques, theory on Infrared Radiation (IR) and heat transfer is reviewed in chapter 2. The methodology used in this research can be found in chapter 3. In this chapter both the experimental and numerical methods applied in this research are discussed. The validation of the numerical analysis is shown in chapter 4. The results on the characterisation with the different thermography methods is discussed in chapter 5 and 6. The conclusion and discussion of the obtained results and the formulation of the research question answer can be found in chapter 7. Recommendations for further research are made in chapter 8.

Chapter 2: Theory on thermography

This chapter aims to create a thorough overview of the knowledge relevant to this research. Optical thermography uses Infrared Radiation (IR) to determine the surface temperature. The physical theory of Infrared Radiation (IR) is described in section 2.1. Since only the surface temperature can be measured, the internal heat flow is important for subsurface defect detection. The heat flow in the test object can be described by thermal waves as is explained in section 2.2. The theory and recent advances in different optical thermography methods are described in section 2.3. This final section concludes with an overview of the advantages and disadvantages of the different thermography methods.

2.1 Infrared Radiation

Sir William Herschel discovered thermal radiation in the early 1800s, this discovery was first called Calorific Rays since the rays contained (thermal) energy. In the following two centuries, many other scientists (amongst them Macedonio Melloni, Gustav Kirchhoff, James Clerk Maxwell, Joseph Stefan, Ludwig Boltzmann, Max Planck)[18] worked on the theory of IR developing it into the knowledge of today.

Any object at a temperature above absolute zero emits electromagnetic radiation in the IR section of the electromagnetic spectrum. An overview of the electromagnetic spectrum is shown in Figure 2.1. The types of electromagnetic radiation can be classified by their wavelength in vacuum:

- Short Wavelength Infrared Radation band (SWIR): from 0.76 to 2 µm
- Medium Wavelength Infrared Radiation Band (MWIR): from 2 to 4 µm
- Long Wavelength Infrared Radiation band (LWIR): from 4 to 14 µm
- Very Long Wavelength Infrared Radation band (VLWIR): from 14 to 1000 µm

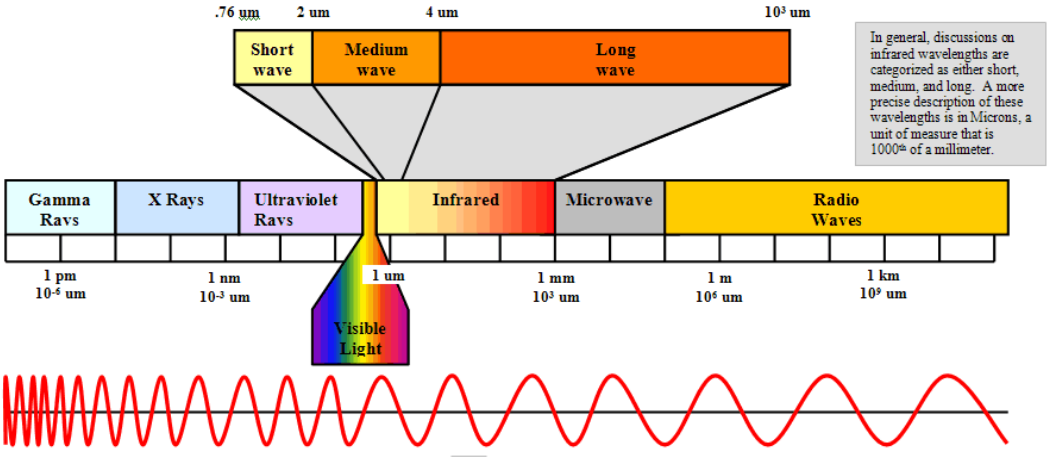

Figure 2.1: *The electromagnetic spectrum with the IR bandwidth [21].*

The spectral emittance of the electromagnetic radiation E_λ can be described by Planck's law in Equation 2.1 [22]. In Plank's law, c_1 and c_2 are the first and second radiation constant, λ is the wavelength of the radiation and T is the absolute temperature of the black body.

$$E_\lambda = \frac{c_1}{\lambda^5(e^{c_2/\lambda T - 1})} \tag{2.1}$$

The maximum spectral radiance at a given temperature is given by Wien's displacement law which is shown in Equation 2.2. In this equation b is the Wien's displacement constant ($\approx 2,898$ µm $\cdot$ K).

$$\lambda_{max} = \frac{b}{T} \tag{2.2}$$

Integration of Planck's law over the entire spectrum results in the total hemispherical radiation intensity in Equation 2.3 in which σ_{SB} is the Stefan-Boltzmann constant ($\approx 5.67 \cdot 10^{-8}$ W $\cdot$m$^{-2}\cdot$K^{-4}).

$$E_b = \sigma_{SB} T^4 \tag{2.3}$$

The equations stated above are applicable to blackbodies. Real objects are referred to as gray bodies since real objects only emit and absorb a fraction of this energy. The fraction of the emitted energy is called the emissivity of a material while the fraction of the incident flux that is absorbed by a object is called the absorbance. Next to the absorbed energy, a part of the energy is reflected. The emissivity, absorbance and reflectivity are dependent on the material, surface roughness and wavelength of the light [23].

Practical applications using the IR spectrum date back to the nineteenth century [24]. Many more ideas of IR applications are formed in the beginning of the twentieth century. Some of these applications were detecting icebergs in 1914 [25] and monitoring forest fires in 1934 [26]. Applications on material analysis started by measurements of thermophysical properties of materials. The basic idea of this technique dates back to 1937 by Vernotte who also described the effusivity of a material [27].

Effusivity is one of the material properties of importance in thermography as it describes the ability of a material to exchange thermal energy with its surroundings. The thermal effusivity is related to the thermal conductivity k, the mass density ρ and the specific heat capacity c_p as is described by Equation 2.4.

$$e = \sqrt{k \rho c_p} \tag{2.4}$$

The first infrared camera was invented in 1929 for application in the anti-aircraft defence in Britain. In the 1940s the first thermographic camera in the form of infrared line scanners was developed by the U.S. military. This technique took one hour to produce a single image. It took until the 1960s for the first real-time thermographic camera to be commercially available, this type of camera used a cooled photoconductor [28]. A photoconductor directly detects photons and translates this into electrons. This results in either a current flow or a change in conductivity which is proportional to the radiance of the measured surface. This technique is still used for high-end cryogenic cooled cameras. A small Stirling cooler is used to keep the detector at a constant temperature of 77 K, resulting in a high sensitivity and less influence of stray radiation. Nowadays many different materials are applied in photoconductive detectors: amongst others PbSe, HdCdTe, InSb and PtSi [29]. In the 1990s, uncooled microbolometer cameras became available on the commercial market, making IR technology more available and affordable [30]. In the recent years the detection frequency and resolution of IR cameras has improved rapidly [23].

IR cameras can detect Short Wave IR radiation (SWIR) or Long Wave IR radiation (LWIR). In the LWIR band, the absorbance of IR radiation by CO_2 in the bandwidth of 4 to 4.5 µm and the absorbance by H_2O in the bandwith of 5.5 to 7.5 µm influences the measurements. The absorbance of the IR spectrum by atmospheric gasses can be seen in Figure 2.2. Since this absorbance is in the range of IR cameras, it can influence the results.

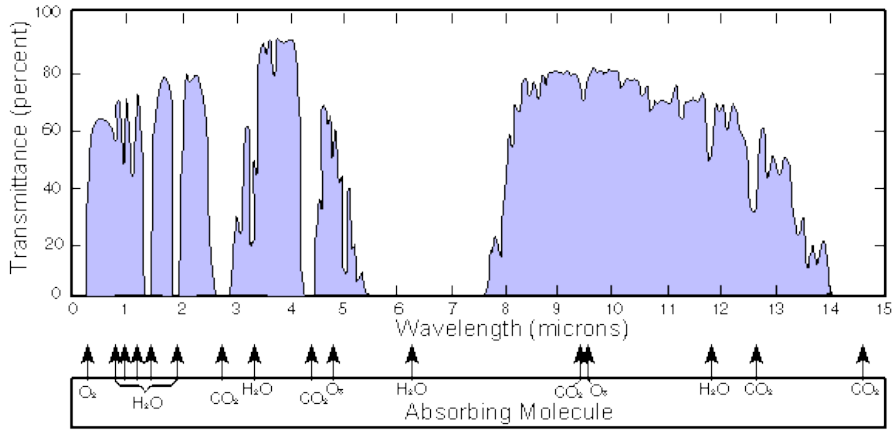

Figure 2.2: *The absorbance of the electromagnetic radiation in the atmosphere [31].*

2.2 Thermal waves

Three dimensional heat flow in a solid object is the basis of the indirect measurements performed with thermography. The three dimensional heat flow in a solid object can be described by the parabolic diffusion equation given in Equation 2.5.

$$\frac{\partial}{\partial x}\left(k_x\frac{\partial T(x,y,z,t)}{\partial x}\right)+\frac{\partial}{\partial y}\left(k_y\frac{\partial T(x,y,z,t)}{\partial y}\right)+\frac{\partial}{\partial z}\left(k_z\frac{\partial T(x,y,z,t)}{\partial z}\right)+I(x,y,z,t)=C\frac{\partial T(x,y,z,t)}{\partial t} \tag{2.5}$$

In this equation k_i is the thermal conductivity in direction i, $I(x,y,z,t)$ is the rate of internal heat generation, which is zero for structural components and C is the volumetric heat capacity of the object. The equation can be simplified if we assume an isotropic homogeneous semi-infinite solid object, resulting in the one dimensional out-of-plane heat transfer described by Equation 2.6.

$$\frac{\partial^2 T}{\partial x^2}-\frac{1}{\alpha}\frac{\partial T}{\partial t}=0 \tag{2.6}$$

In this equation α is the thermal diffusivity and equals the ratio between the thermal conductivity k and the heat capacity C. The thermal diffusivity is a measure for the rate of transfer of heat in a material from hot to cold regions. The assumption of an isotropic homogeneous semi-infinite solid object is not valid for composite material samples. The one dimensional approach does however provide insight in the behaviour of heat flow. By assuming the only heat flow with the surrounding of the sample is described by the boundary condition in Equation 2.7 which describes the heat deposited on the top surface by a frequency modulated heat source, one can obtain the temperature distribution within the solid.

$$-k\frac{\partial T(x,t)}{\partial x}\bigg|_{x=0}=\frac{I_0}{2}\mathrm{Re}\Big[(1+\exp(i\omega t))\Big] \tag{2.7}$$

The heat deposition on the top surface consists of two factors. The first factor is the time independent temperature rise, described by the first term in the square brackets of Equation 2.7. The second factor is the periodic temperature oscillation described by the second term in the brackets of Equation 2.7. As will be explained in section 2.3, the term of interest for most thermography methods is the periodic temperature oscillation. "*The temperature oscillations resulting from the periodical heating of the surface, can be described by thermal waves. Thermal waves are often described as the solution of the parabolic heat diffusion equation* (Equation 2.6) *in the presence of a periodical time varying heat source modulated in intensity at a given frequency.* " [32]

Equation 2.6 can be solved for the periodic oscillating boundary condition by substitution of Equation 2.8 resulting in Equation 2.9 [33][34][35].

$$T(x,t)=\theta(x)\exp(i\omega t) \tag{2.8}$$

$$\frac{\partial^2\theta(x)}{\partial x^2} - q^2\theta(x) = 0 \tag{2.9}$$

In this equation, q is the complex wave vector given by Equation 2.10.

$$q = \frac{1+i}{\mu} \tag{2.10}$$

In this equation, the penetration depth μ is the distance over which heat is transported in the sample during one modulation cycle. The penetration depth (or thermal diffusion length) is inversely proportional to the modulation frequency as is described by Equation 2.11.

$$\mu = \sqrt{\frac{\alpha}{\pi f}} \tag{2.11}$$

From the relation between the penetration depth μ and the frequency f of the heat deposition in Equation 2.11, it can be concluded that lower frequencies penetrate deeper in the sample material. From Equation 2.9, the following solution for the temperature distribution can be derived [35]:

$$T(x,t) = \frac{I_0}{2e\sqrt{\omega}} \exp\left(-\frac{x}{\mu}\right) \cos\left(\frac{x}{\mu} + \omega t + \frac{\pi}{4}\right) \tag{2.12}$$

This solution is a highly damped plane wave propagating in the x-direction. The heat flow in an object resulting from periodically oscillating energy deposition can thus be described as highly damped plane waves, although it is not an actual wave equation since it does not have the second-order time derivative of a wave equation. An example of the thermal waves in a CFRP sample subject to periodical heating can be seen in Figure 2.3.

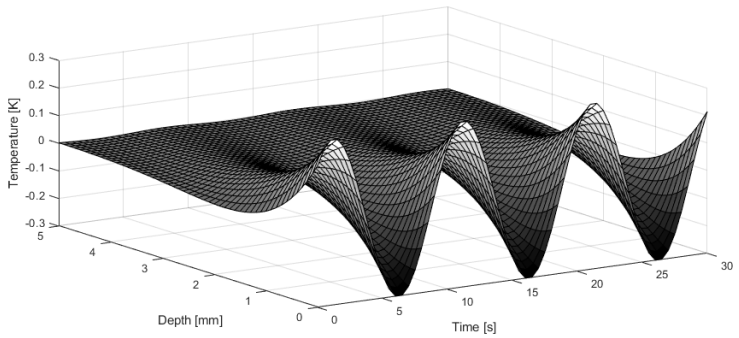

Figure 2.3: *One dimensional thermal waves in a CFRP sample ($k_t = 0.7$ W/mK, $\rho = 1,528$ kg/m^3, $c_p = 1,100$ J/kgK) at a frequency of 0.1 Hz.*

The thermal wave propagates in this manner until an interface is reached. At an interface, thermal waves are reflected and refracted. To solve the temperature distribution over an interface, the temperature and heat flux must be consistent at the interface. Taking the continuity of the temperature and heat flux as boundary condition at the interface, the reflection coefficient R of the thermal waves travelling from material 1 to material 2 in Equation 2.13 is obtained [33][34][35].

$$R_{12} = \frac{e_1 - e_2}{e_1 + e_2} = \frac{\sqrt{k_1\rho_1 c_{p1}} - \sqrt{k_2\rho_2 c_{p2}}}{\sqrt{k_1\rho_1 c_{p1}} + \sqrt{k_2\rho_2 c_{p2}}} \tag{2.13}$$

The reflection of thermal waves at an interface is an important phenomenon for the detectability of subsurface defects using thermal waves. Thermal waves reflect on subsurface features such as delaminations. The reflected thermal waves propagate back to the surface where the wave superposes on the incident wave. Thermography measures the surface temperature over time, enabling detection of the reflected thermal waves and thus of subsurface features. The different thermography methods are discussed in section 2.3.

2.3 Thermography techniques

Thermography is the measurement of the surface temperature of an object using an IR camera that detects IR and produces images of the radiation intensity. Thermography methods can be split in two categories, active and passive methods. In passive methods, no external excitation is applied while in active methods an external excitation is applied in the form of a heating or cooling source. Although both active and passive thermography are applied in the field of NDT, active thermography is more common [23]. Passive thermography is often applied to objects that generate heat internally, for example the detection of hot spots on integrated circuit boards [2]. The lack of temperature differences in defects in composite materials results in a low sensitivity for defects with passive thermography, thus limiting the application for damage detection [2]. However, active thermography is frequently applied in damage detection in composite materials since an external energy source is used to increase the temperature, enlarging the difference between the defect and non defect regions. Commonly used methods for excitation are optical and ultrasound. In this report the focus is put on optical excitation since this method is better applicable to large surfaces. The schematic set-up of an active optical thermography method can be seen in Figure 2.4.

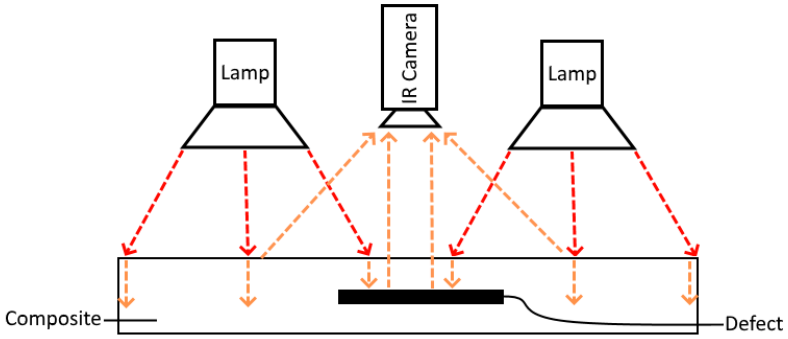

Figure 2.4: *Schematic set-up of active thermography on a testobject with a subsurface defect.*

Local differences in the surface temperature can be caused by several factors including both external and internal factors. The external factors can be considered disturbances to the thermography process since the accuracy of the method is decreased by these influences. The external factors that can influence the surface temperature are amongst others, the heating source, humidity and air flow. The internal factors are related to the heat flow of the material. The heat flow is affected by internal features of the material. Next to the thermal properties of the material, these features can be different kind of abnormalities; delaminations, moisture ingress, spurious material inclusions, resin rich regions or fibre distortions, but also the geometry of the object.

The disadvantage of thermography is the limited depth-penetration capability of the technique. The maximum detectable defect depth is dependent on the thermal properties of the material. Defects in GFRP for example are proven to be detectable up to 6 mm [36], but detectability is highly dependent on the defect size, defect thickness and the thermal properties of both the defect and the sample material. For other materials a larger depth can be inspected depending on the thermal properties of the material.

Multiple methods of active optical thermography are applied in the NDT field [2][19][20].

- Pulsed Thermography **(PT)**: A widely applied method, the reason for the popularity of PT is the short inspection time. The method relies on a short thermal excitation in the form of pulsation of a high power flash lamp. The analysis is done in the time domain.
- Pulsed Phase Thermography **(PPT)**: Uses a pulse signal from high power flash lamps. The analysis is done in the frequency domain to obtain the amplitude and phase.
- Lock in Thermography **(LT)**: Uses a sinusoidal signal to deposit heat over a longer time period. Analysed in the frequency domain to obtain the amplitude and phase at a certain frequency.

- Frequency Modulated Thermal Wave Imaging **(FMTWI)**: Uses a chirp signal to deposit heat over a longer time period spread over multiple frequencies. The analysis can either be done in the frequency domain or by applying Cross Correlation (CC).
- Barker Coded Thermal Wave Imaging **(BCTWI)**: Uses a 7-bit Barker code signal to deposit heat. This signal is specially developed for the application in CC.

These method differ in signal used for heat deposition on the surface and in the way the perceived signal is analysed. Since some of these methods use either the same signal or the same signal processing method, an overview of the methods is given in Table 2.1.

Table 2.1: *Overview of the heat source, heat signal and data processing method of the different optical thermography methods.*

Method	**Heat source**	**Heat signal**	**Data processing method**
PT	Flash lamp(s)	(Dirac) pulse	Time domain
PPT	Flash lamp(s)	(Dirac) pulse	Frequency domain (FFT)
LT	Lamp(s) / laser	Sine wave	Frequency domain (FFT/Lock-in)
FMTWI	Lamp(s) / laser	Chirp	Frequency domain (FFT)/Pulse compression (CC)
BCTWI	Lamp(s) / laser	7-bit Barker code	Pulse compression (CC)

These methods have been studied extensively over the past 20 years by a large group of scientists. The different methods are split based on the data processing method used since this determines the results of the thermography methods. The application of time domain analysis, frequency domain analysis (using lock-in/FFT) and pulse compression analysis (using Cross Correlation (CC)) in thermography are explained in the subsection 2.3.1, 2.3.2 and 2.3.3 respectively. In each of these subsections the suitable heat sources and heat signals for each type of analysis are also discussed. Lastly, subsection 2.3.4 summarizes the differences of the thermography methods.

2.3.1 Time domain analysis

The analysis in the time domain relies on a short thermal excitation in the form of a pulsation from a high power flash lamp. The lamp deploys heat to the surface of the object for a duration of a few milliseconds. After the heating period the surface temperature is measured with an IR camera to obtain the temperature decay curve. The temperature decay of the front surface is caused by propagation of the thermal wave front, radiation at the surface and convection at the surface. Subsurface abnormalities influence the propagation of heat inside the material resulting in a different surface temperature above the abnormality with respect to non defect regions as can be seen in the typical surface temperature decay curve in Figure 2.5.

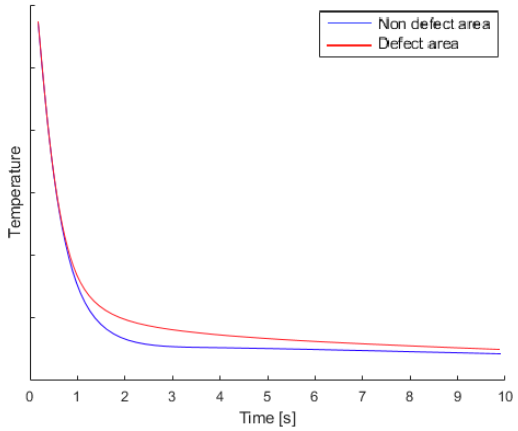

Figure 2.5: *Typical plot of the surface temperature decay of defect and non-defect regions after a pulse heat deposition.*

Since the detection of abnormalities is dependent on the thermal propagation in the material, deeper defects are observed later than shallow defects. The deeper defects have a reduced contrast due to the attenuation of the thermal wave in the depth direction and the lateral heat dissipation. The observation time t and the contrast c are be described by Equation 2.14 and 2.15 respectively [23].

$$t \approx \frac{d^2}{\alpha} \tag{2.14}$$

$$c \approx \frac{1}{d^3} \tag{2.15}$$

In these equations, d is the defect depth and α is the thermal diffusivity. Time domain analysis (Pulse Thermography) is very sensitive to variations of test conditions [2]. Uneven heating or reflection on the surface influences the surface temperature distribution and thus directly influence the results. This limits the applicability of the method to controllable environments in which even distribution of the heat source over the surface is possible.

2.3.2 Frequency domain analysis

The temperature of the surface is measured during the heating process using an IR camera. This time-domain data can be transferred to the frequency domain by using a lock-in amplifier or by using a Discrete Fourier transformation (DFT) from Equation 2.16 for each pixel separately [2][37][38].

$$F_n = \sum_{k=0}^{N-1} T(k) e^{-2\pi i k n/N} = \mathrm{Re}_n + i\mathrm{Im}_n \tag{2.16}$$

After transferring the data to the frequency domain, the amplitude A and phase φ can be obtained for each pixel n using Equation 2.17 and 2.18 respectively.

$$A_n = \sqrt{\mathrm{Re}_n^2 + \mathrm{Im}_n^2} \tag{2.17}$$

$$\varphi_n = \tan^{-1}\left(\frac{\mathrm{Im}_n}{\mathrm{Re}_n}\right) \tag{2.18}$$

By analysing the data for each pixel separately, amplitude and phase images are obtained as is schematically shown in Figure 2.6. The amplitude image is sensitive to inhomogeneities of the test surface, the emissivity and the distribution of the applied heat [2]. In the phase image, each of these effects is eliminated by processing the data on pixel level [2]. This is very useful for practical applications of thermography in aerospace industry since the surfaces are curved and large, making uniform heating very hard to achieve.

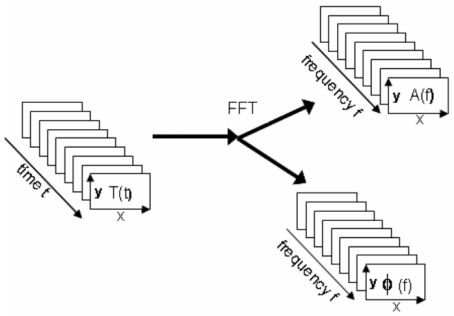

Figure 2.6: *Schematic representation of the image processing of frequency domain analysis [39].*

When the top surface of an infinitely large sample is exposed to uniform heat deposition and no abnormalities are present, the thermal wave propagates as a plane into the material. This would result in uniform phase and amplitude images. Abnormalities will however disturb the heat flow. If the thermal waves strike on an interface, for example a delamination, the incident wave is partly reflected. The incident thermal wave and the reflected wave therefore interfere resulting in a change in amplitude and a phase shift.

Three different heat signals can be used for frequency domain analysis in thermography, the first is a pulse signal, the second is a periodical sine wave signal and the third is a linear chirp signal. Using a pulse signal in combination with frequency analysis is referred to as Pulsed Phase Thermography (PPT). Using a sine wave in combination with frequency domain analysis is called Lock-in Thermography (LT) and lastly the combination of a linear chirp signal with frequency domain analysis is called Frequency Modulated Thermal Wave Imaging (FMTWI). Each of the three methods is explained in more detail.

Pulsed Phase Thermography (PPT) uses a pulse signal (similar to PT) for the energy deposition on the test object surface. An ideal pulse of null duration has a frequency spectrum with uniform energy distribution over all frequencies. Real pulses have a finite duration and amplitude, the signal contains different energy at different frequencies. The energy distribution over frequencies is determined by the pulse duration, longer pulses concentrate energy in lower frequencies. The inspection of deeper regions requires lower frequencies as is clear from Equation 2.11, thus the pulse duration must be increased. This spreads the available energy over the frequencies resulting in lower energy at high frequencies and thus increased influence of noise at these frequencies [2]. The available energy is limited due to the short period of time heat is applied to the surface and the maximum power of the source. For accurate testing at different depths, multiple measurements with varying pulse lengths must be performed [2].

Lock in Thermography (LT) uses a sinusoidal power modulation of the heat source to deposit heat on the test object surface. The heat is applied using an optical source, in most cases one (or multiple) halogen lamp(s). In some cases a laser is used as a heating source. The temperature modulation results in a periodical transfer of heat to the surface. The heat propagates into the test object as a thermal wave. Since the signal is a sine-wave, the phase φ and amplitude A can also be found by using the four-point algorithm using Equation 2.19 and 2.20 respectively. Using more points reduces the influence of the noise. In these equations, S_1 to S_4 are equidistant signal data points as shown in Figure 2.7a. Practical heat sources are however unable to cool the object, resulting in an increasing global trend of the surface temperature. The sample is heated for several cycles until a near equilibrium DC temperature has been reached as can be seen in Figure 2.7b. A multiple (1-10) of cycles are measured after the DC temperature has reached an equilibrium to obtain accurate results using Equation 2.19 and 2.20. This results in a cycle time of several minutes for lower frequencies. An alternative method is de-trending the signal to obtain the AC component.

$$\varphi = \tan^{-1}\left(\frac{S_1 - S_3}{S_2 - S_4}\right) \tag{2.19}$$

$$A = \sqrt{(S_1 - S_3)^2 + (S_2 - S_4)^2} \tag{2.20}$$

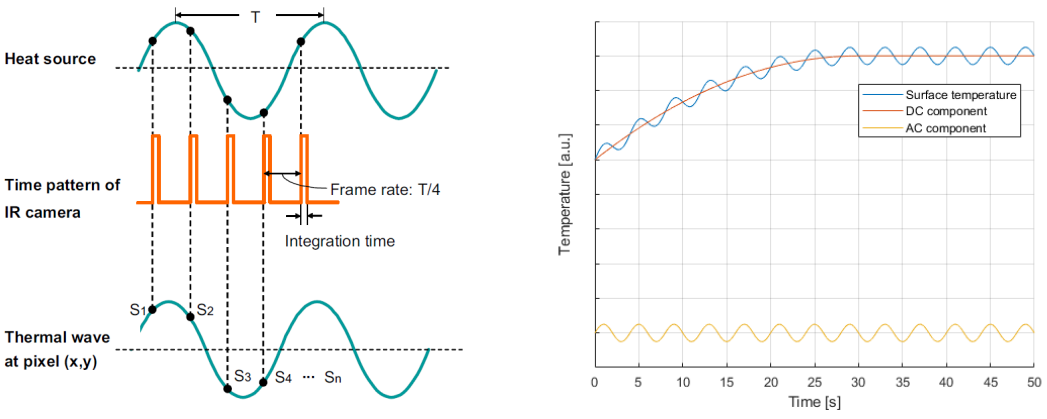

(a) *Data points used in LT [40]*

(b) *Typical surface temperature of test object with LT at 0.25Hz*

Figure 2.7: *Plots of the temperature over time with lock in thermography.*

For the LT analysis, the energy is concentrated around the frequency of the excitation source whilst a pulse contains a broader frequency spectrum. This increases the contrast with respect to PPT where the limited energy is spread over a range of frequencies. For Carbon Fibre Reinforced Plastic (CFRP) materials, the excitation frequency is normally within the range from approximately 0.001 Hz - 5 Hz [41][42]. For high conductive materials like metals, higher frequencies are commonly used in the range up to 50 Hz [43].

All defects have a blind frequency f_b, which is a frequency at which the defect region has no phase shift with respect to non defect regions and the defect can thus not be identified using the phase data. For frequencies above the blind frequency, the phase difference is small and approaches zero with increasing frequency. A plot of the phase shift for different excitation frequencies is shown in Figure 2.8, in this plot the blind frequency is highlighted with a red circle. Theoretically the blind frequency can be predicted when the material properties, defect depth and location are known [44][45]. Experiments by several authors suggests that the blind frequency correlates to 1.5 to larger than 2 times the penetration depth at that frequency [46][47][48]. This can be described by Equation 2.21.

$$d = C\mu = C\sqrt{\frac{\alpha_t}{\pi f_b}} \tag{2.21}$$

In this equation C is the material correction factor (1.5 to 2+), d is the defect depth, α_t is the thermal diffusivity and f_b is the blind frequency. In practical NDT applications, the properties C and α_t are not exactly known. It is therefore necessary to always test on multiple frequencies resulting in long measurement times. This is one of the main limitations of LT and led to the application of a chirp signal.

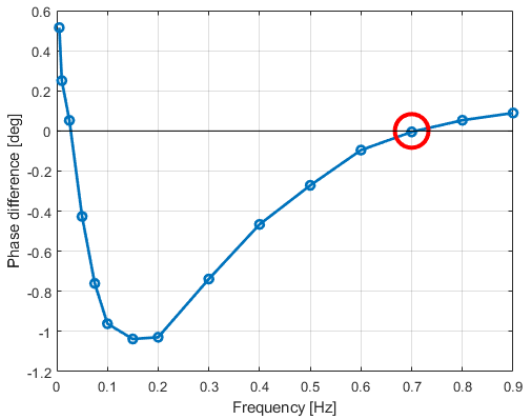

Figure 2.8: *Phase difference between defective and non-defective area as a function of the excitation frequency with highlighted blind frequency f_b (simulated for NTP-A2 panel defect $T_{3,1}$).*

Frequency Modulated Thermal Waves Imaging (FMTWI) uses a chirp signal with which the surface heating is done with a range of frequencies. This range of frequencies can be chosen based on the test subject and its properties. The signal is a low peak-power, long duration modulated wave signal. The linear chirp signal is described in time by Equation 2.22 and is shown in Figure 2.11a.

$$s(t) = A\cos\left(2\pi\left(\frac{f_1 - f_0}{2\mathrm{T}}t + f_0\right)t + \phi\right) \tag{2.22}$$

In Equation 2.22 A is the amplitude of the signal, f_0 is the start frequency, f_1 is the end frequency, T is the total signal time and ϕ is the initial phase. The advantage of using a linear chirp signal is that a range of frequencies is covered, the phase can thus be determined for multiple frequencies using the data from one measurement. This requires significantly less measurement time and only a single measurement to obtain the data in Figure 2.8 for a defect [49].

The limited signal to noise ratio obtained with the phase in the frequency domain analysis led to the development of pulse compression analysis for thermography as is discussed in the following subsection.

2.3.3 Pulse compression analysis

In the search for higher sensitivity and resolution, using pulse compression is proposed as processing method [50]. Pulse compression is a technique that is often used in radar systems since it is designed to enhance the detection sensitivity, resolution and reduce noise. The cross correlation $g(\tau)$ of the reference signal $s(t)$ and the perceived signal $h(t)$ can be determined by Equation 2.23 or 2.24. The first is in the time domain while the latter is in the frequency domain.

$$g(\tau) = \int_{-\infty}^{\infty} s(t)h(\tau + t)dt \tag{2.23}$$

$$g(\tau) \propto \mathcal{F}^{-1}[S(\omega) * H(\omega)] \tag{2.24}$$

As an explanatory example, the Cross Correlation (CC) of a sine signal and a cosine signal is shown in Figure 2.9. With increasing time delay τ, the red cosine signal is shifted to the right resulting in different values for the correlation. The resulting correlation value is shown in Figure 2.9b. Since these signals are periodical in nature, the cross-correlation is also periodical. The period of the signals is set to 2 s, the time shift between the sine and cosine signal is thus 0.5 s. This results in a peak in the cross correlation at a delay time of 0.5 and 2.5 s. The length of the signals is limited, resulting in a value of zero if the time delay τ is larger than the duration of the reference signal $s(t)$. Non-periodical signals are more suitable for CC since these signals have one cross correlation peak instead of a periodical peak value as can be seen in Figure 2.10.

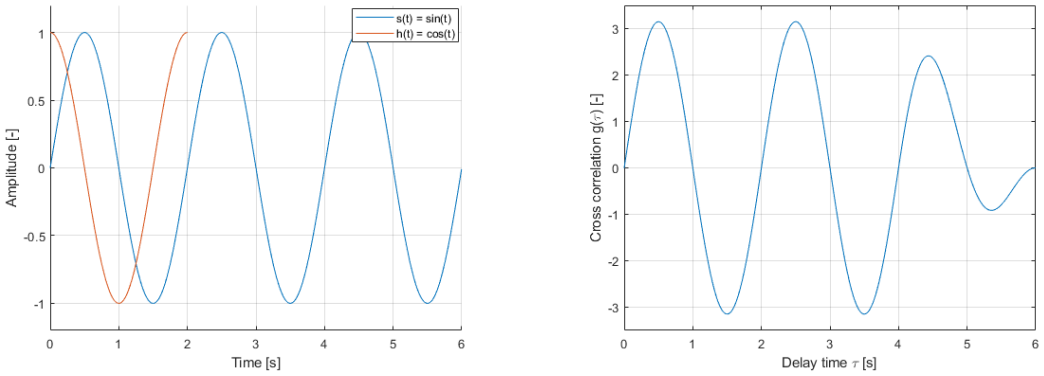

(a) *Sine signal with a length of 6 s and a cosine signal with a length of 2 s.*

(b) *The Cross Correlation of the signals in Figure 2.9a.*

Figure 2.9: *Graphical explanation of Cross Correlation (CC).*

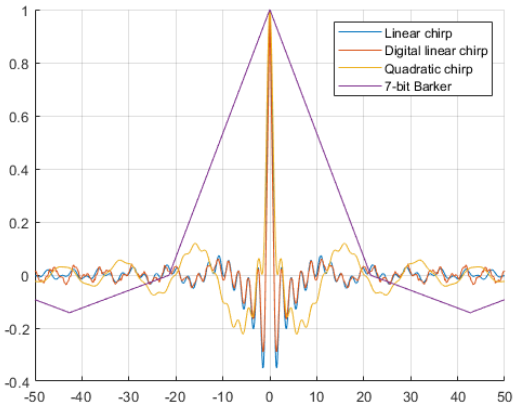

Figure 2.10: *The auto correlation of different signals with a length of 150 s.*

The time delay and value of the cross correlation main peak are the characteristics that can be determined for each pixel resulting in a peak correlation image and a peak delay image respectively. The time delay of the main peak is determined using Equation 2.25.

$$\tau_{CCpeak} = \tau|_{\{g(\tau)=\max(g(\tau))\}} \tag{2.25}$$

The CC peak value is dependent on the magnitude of both the perceived signal $h(t)$ and the reference signal $s(t)$. The amplitude of the reference signal can be set to one. However, the amplitude of the measured signal is directly dependent on the heat distribution on the surface. Uneven heating therefore greatly influences the CC peak value. In 2011, Tabatabaei et al. suggested the cross correlation phase as a method to normalize the CC peak value [51]. The cross correlation phase can be obtained by dividing the cross correlation of the signal and the reference by the cross correlation of the signal and the quadrature of the reference as is shown in Equation 2.26. The quadrature of the reference signal is determined by performing a Hilbert transform which is the term between square brackets in the denominator of Equation 2.26.

$$\varphi_{CC} = \left.\frac{\mathcal{F}^{-1}(S(\omega) * H(\omega))}{\mathcal{F}^{-1}([-i\ \mathrm{sgn}(\omega)S(\omega)] * H(\omega))}\right|_{\tau=0} \tag{2.26}$$

Both the time shift, the magnitude of the CC peak and the CC phase can be a measurement of the defect depth [50][51]. In recent years, several experiments have been conducted on CC as analysis method for thermography, all showing the improved Signal to Noise Ratio (SNR) in comparison with LT [52][53][54]. Applications have expanded to concrete inspection [55] and human breast cancer inspection [56].

All non periodical signals are in theory suitable for pulse compression using CC. However there are several signals which result in a good Peak Sidelobe Level (PSL). The Peak Sidelobe Level (PSL) can be determined using Equation 2.27.

$$\mathrm{PSL} = 20\ \log(\frac{\text{Side lobe peak}}{\text{Main lobe peak}})\ \mathrm{dB} \tag{2.27}$$

Several signals have been applied in thermography:

- Linear chirp signal (Figure 2.11a)
- Digital chirp signal (Figure 2.11b)
- Quadratic chirp signal (Figure 2.12a)
- 7-bit Barker signal (Figure 2.12b)

The auto correlation function of a chirp signal is shown in Figure 2.10. It can clearly be seen that the side lobes around the correlation peak are relatively large. Reduction of the side lobe amplitude results in improved detection performance and depth resolution [57][58]. Three options for reducing the side lobe energy are proposed [20][59]. The first method is replacing the linear chirp with a digitized chirp signal (DFMTWI) as Mulaveesala proposed in 2016 [60]. In DFMTWI the input signal is converted into the digital form that can be seen in Figure 2.11b. The advantage of using a digitized form of the chirp signal is the higher amount of energy injected at the fundamental frequency leading to an increased amplitude of the reflected signal [60]. The second method is replacing the the linear chirp signal with a quadratic chirp while the third method is to use a 7 bit Barker coded signal. Both signals are shown in Figure 2.12. Barker coded signals are widely used in radar and ultrasonic systems, in 2011 the use of this binary phase code has been implemented for NDT purposes by Tabatabaei and Mandelis [20]. Seven different Barker codes are known. A Barker code has a maximum cross correlation side lobe peak of one. In total 11 different Barker codes are known. The 7-bit Barker code is the optimal length for optical thermography [20].

The result of the quadratic chirp and the 7-bit Barker code signals on the correlation function is shown in Figure 2.10. The reduced PSL in theory results in a higher SNR leading to a high contrast between defective and non-defective regions [59][61].

Many efforts have been put into the use of a Barker sequence codes in NDT over the past 10 years [20][52]. In 2018, Fei Wang et al. used a truncated-correlation of a pulsed chirp signal with a laser heat source for qualitative three-dimensional visualization of surface cracks by changing the reference signal delay time [62]. BCTWI has been applied to CFRP and GFRP materials, verifying the detectability of defects with this method and the superiority of the method in comparison with LT [20][52][53][63][64]. However no effort has been done to link the thermography results to defect characters and further research is required on this subject.

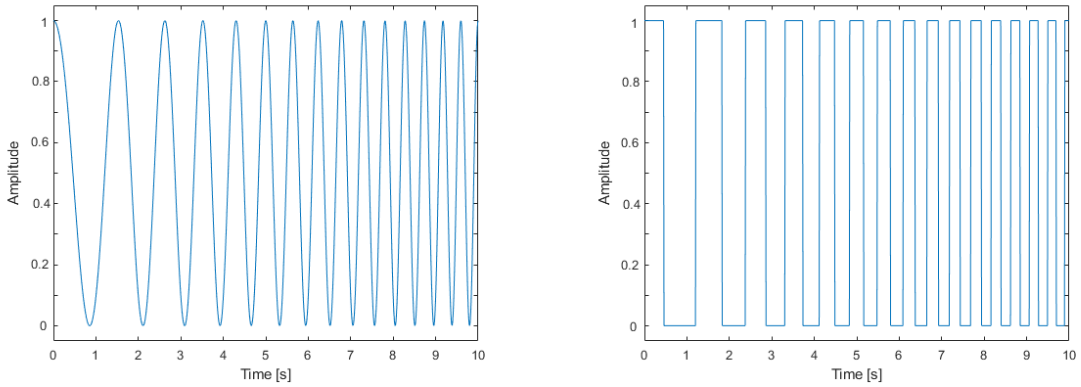

(a) *Linear chirp signal* (b) *Digital chirp signal*

Figure 2.11: *Chirp signals (frequency from 0.5 Hz to 2.5 Hz in 10 sec).*

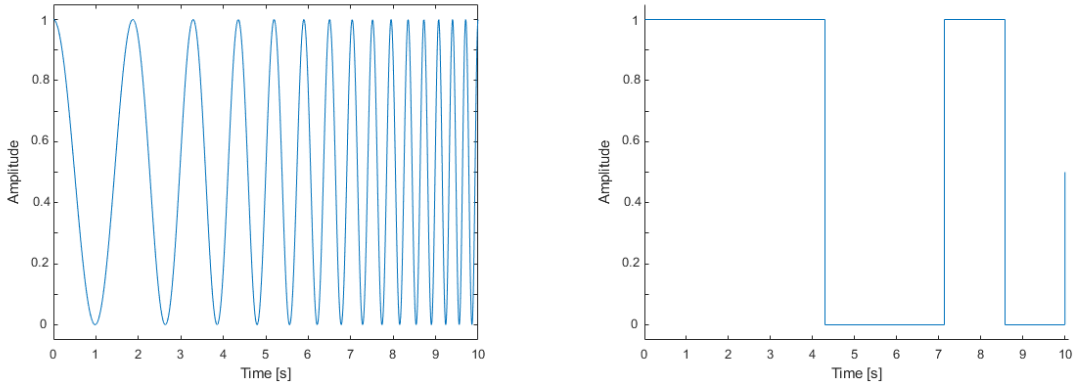

(a) *Quadratic up chirp signal* (b) *7 bit Barker signal*

Figure 2.12: *Signals used for pulse compression.*

2.3.4 Comparison of the optical thermography methods

As discussed in the previous subsections, different methods are available for optical IR thermography. The methods differ in the heat source and the heat signal used for the heat deposition and the processing method for the measurement data. An overview of these differences has been provided in Table 2.1.

Due to the fundamental differences between the methods, the results obtained also differ. PT and PPT deposit heat on the object using a pulse signal. PT is sensitive to uneven heating and reflections of the surface making it unsuitable for large surface in-situ inspections. PPT is less sensitive to these factors since the phase is analysed for each pixel separately. PPT is however limited in the amount of heat that can be deposited on the surface due to the pulse length. Both PT and PPT require very high powered lamps in order to deposit enough heat on the surface in a few millisecond duration flash.

Frequency domain analysis with a sine wave or a chirp signal spreads the energy deposition over a longer time. The long duration low peak power heat deposition makes deeper defects detection possible without overheating the object and with only a limited peak power required from the lamps. The pulse compression analysis also uses low peak power long duration signals, but these signals are processed using CC resulting in different thermography results. The pulse compression analysis results in a higher SNR than the frequency domain analysis.

The time domain analysis is known to be sensitive to the environmental conditions. The high power flash lamps are inferior in reaching deeper defects without overheating the test object. Therefore in this research the focus is on frequency domain analysis and pulse compression analysis with low peak power long duration signals. These analysis methods have more defect detection potential at larger depths and require less power from the lamps.

Chapter 3: Methodology

This chapter elaborates on the methodology used in this research in order to answer the research question. The research question (see section 1.4) is split in four sub questions. The sub questions are repeated here for the convenience of the reader:

- *What is the influence of the (partly unknown) composite material properties on the thermography results?*
- *What is the influence of the different types of defects on the thermography results?*
- *What is the influence of noise on the thermography results?*
- *Which optical thermography method is the most conclusive in determining defect characters?*

Thermography is a secondary method, meaning that the method does not directly measure defect properties but only the temperature of the top surface. From this temperature, different results are obtained depending on the thermography method. Therefore the results and characteristics of each method must be determined. From these results, relevant features need to be determined regarding the subsurface defect. Due to secondary nature of the thermography measurement, several factors influence the results. An overview of these factors and their parameters is shown in section 3.1. In this section, the method for determining the influence of each factors is discussed.

The samples available for this research are limited to a single CFRP material and teflon coated glass inserts as is discussed in section 3.2. The samples are not sufficient to answer the first and second research question. Numerical simulations are therefore used to vary the properties of influence to the thermography results. The experiments are used to validate the simulation model and determine the influence of noise on the thermography results. In section 3.2 details on the experimental set-up and the CFRP samples used in this research are provided.

Numerical simulations are used to vary properties, such as the thermal conductivity of the material, that are difficult to vary in real samples. Section 3.3 shows the details of the simulation model. The simulations are used to determine the sensitivity of the process to different properties and provide insight in how the techniques work under ideal circumstances without noise. The data obtained from both the simulations and the experiments require processing. The data processing method differs for the different thermography methods. The data processing in the frequency domain analysis and the pulse compression analysis are discussed in section 3.4.

To provide an answer to the last question, the steps above are executed for the frequency domain analysis and the pulse compression analysis and processed separately in chapter 5 and 6 respectively. Conclusions to each of the questions stated above are formulated in chapter 7.

3.1 Influencing factors and their parameters

Thermography methods use the surface temperature to detect subsurface abnormalities, the result obtained by any thermography method is thus indirect. A number of factors influence the thermography results. For quantitative analysis of thermography results, the influence of each of these factors needs to be determined. The influences can be split in six factors; the thermography method, the lamps, the camera, the surface, the sample material and the defect. Each of these factors has several process parameters that are either determined by the test object or by the set-up used. A schematic representation in the form of an Ishikawa diagram (also known as fishbone diagram) of the influencing factors and their parameters is given in Figure 3.1. The green boxes in this figure represent the factors that can be influenced by the set-up or the operator while the red boxes are the factors that are determined by the object under inspection. The parameters of each factor are shown next to the arrows.

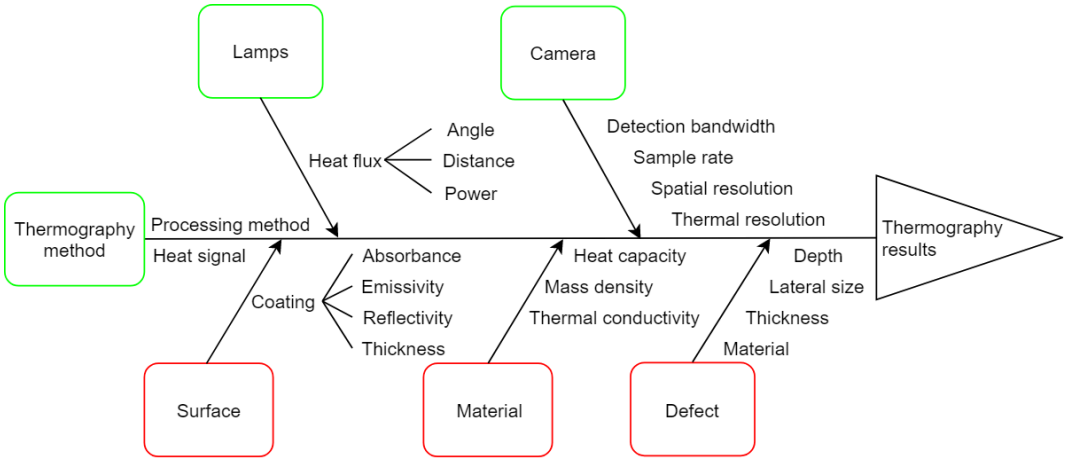

Figure 3.1: *Ishikawa diagram showing the influencing factors (in the boxes) and their parameters on thermography results. Green boxes indicate that the factors can be influenced by the set-up or the operator. Red boxes indicate that the factors can not be influenced.*

It is clear that the thermography results are not only influenced by the properties of the defect. In order to characterize defects with the thermography results, either the value of the parameters or the sensitivity of the results to the parameters in Figure 3.1 needs to be known. Since often not all parameters are known, the sensitivity of the results to the parameters is determined using a One-Factor-at-A-Time (OFAT) analysis. This type of analysis determines the influence of several factors one at a time instead of testing the influence of multiple factors simultaneously. This provides a clear view of the influence of each parameter. However, the interaction between the influence of different factors is not included in an OFAT analysis. This is overcome by combining the influence of each of the parameters to obtain a set of parameters that result in the boundary values for the thermography results. The parameters will be elaborated here for each factor, starting with the factors in the green boxes from Figure 3.1 and ending with the factors in the red boxes.

Thermography method This research focusses on two signal processing methods as is discussed in subsection 2.3.4. The different data processing methods generate different results. Frequency domain analysis provides a phase and amplitude value for each pixel at different modulation frequencies. Pulse compression analysis results in a peak correlation value, peak delay time and cross correlation phase for each pixel. The characteristics of these signals are determined and the sensitivity of these characteristics to variations in all other parameters is obtained by varying the parameters one at a time. Since different signals can be used for both methods, the difference in heat signals is also a parameter that can influence the thermography results.

Lamps The halogen lamps can vary the process in several ways; the total power, the distance from the surface and the angle towards the surface. The result of varying these parameters is a different heat flux at the surface of the sample. As a 5 W heat flux does not result in a significant temperature increase while a 50 kW heat flux would result in overheating the component and damaging it, the total heat flux can influence the detectability of defects and the results. The amount of heat absorbed by the sample is measured and the sensitivity of the results to variations of this heat flux are determined by increasing and decreasing the lamp power in both experiments and numerical simulations.

Camera The camera used for the thermography measurements has an effect on the detectability of defects. The sample rate of the camera directly determines the amount of data obtained by the measurement. The processing of the data is limited to this discrete step size. The detection bandwidth and thermal and spatial resolution limit the detectability of defects. These limitations are taken into account in the comparison of the simulations and the experiments.

Surface The surface of the test object is commonly covered by a coating. This coating can vary in thickness depending on the application. The surface roughness and colour of the coating result

in variations of the emissivity, the absorbance and the reflectivity. These three properties influence the amount of heat that is absorbed and the amount of heat that is transmitted. The absorbed heat is already varied in order to determine the influence of the lamps. The amount of radiative heat transmittance directly influences the magnitude of the temperature measurement with the IR camera. This magnitude is however not of direct influence to the results as is discussed in section 2.3. A reflective surface might increase the influence of noise. To prevent this, two precautions are taken. The first is a filter in front of the halogen lamps to block the IR camera detection bandwidth to block direct reflections of the heat source. The second precaution is an IR absorbing screen behind the set-up to prevent other IR sources reflecting on the surface.

Material Thermography relies on a difference in thermal properties between the defect material and the sample material to detect the defects. The thermal properties of a sample are more likely to be known in production environments while in in-situ inspections, the knowledge of these properties is often limited. In production environments, these properties can also be determined more easily since a test sample can be made from the same material and both sides of the samples can be reached allowing for through transmission measurements. The range of the properties of CFRP and the properties of the other materials obtained from literature is listed in Table 3.1. The influence of the wide range of CFRP properties on the thermography results is determined by performing numerical simulations with different material properties. Combinations of CFRP properties resulting in the boundary thermography result values can then be composed. By performing simulations with these combinations of CFRP properties, the range of thermography results for a specific defect can be determined.

Defect A subsurface abnormality in a composite part is defined as a defect in this research. A defect can vary in four different parameters. The first is the depth at which the defect is located. Since heat propagation is highly dissipative, deeper defects are harder to detect. The second parameter is the defect material. Composite panels can contain various sorts of defects as is discussed in section 1.1. The expected type of defects depends on the environment. In production environments, the main defects occurring are resin-starved areas, resin-rich areas and foreign material inclusions, such as teflon or kapton. In in-situ inspections, the main defects of interest are delaminations. The properties of several different materials are shown in Table 3.1. The third and fourth parameters are the size of defects in lateral and thickness direction respectively. All four parameters can heavily influence the thermography results. The defect lateral size and depth are varied in the samples. The thermal properties of the sample and defect and the thickness of the defect are not varied within the samples. The influence of these properties is evaluated using numerical simulations for each thermography method.

Table 3.1: *CFRP and defect material properties from literature and the NTP samples.*

Material	**Property**	**Min.**	**Nom./sample**	**Max.**	**Unit**
CFRP [65][66][67] [68][69][70][71]	Density	1,150	1,528	2,250	kg/m^3
	Thermal capacity	1,000	1,100	1,200	J/kgK
	Thermal conductivity in-plane	2	7	12	W/mK
	Thermal conductivity out-of-plane	0.3	0.7	1	W/mK
Teflon coated glass [66][72]	Density		2,200		kg/m^3
	Thermal capacity		1,000		J/kgK
	Thermal conductivity		0.26		W/mK
Kapton tape [73]	Density		1,420		kg/m^3
	Thermal capacity		1,090		J/kgK
	Thermal conductivity		0.12		W/mK
Air (thin gap) [70][74]	Density		1.2		kg/m^3
	Thermal capacity		1,005		J/kgK
	Thermal conductivity		0.07		W/mK
Water [70]	Density		1,000		kg/m^3
	Thermal capacity		4,193		J/kgK
	Thermal conductivity		0.586		W/mK
Top coating (on NTP panels)	Density		1,600		kg/m^3
	Thermal capacity		1,800		J/kgK
	Thermal conductivity		0.35		W/mK

3.2 Experiments

The experimental set-up consists of a FLIR SC7600 IR camera, two 2 kW halogen lamps, a signal generator and a computer for data logging. The set-up is shown in Figure 3.2. During the experiments, a large ($\approx$ 3000 x 2000 mm) polycarbonate screen is placed behind the IR camera to prevent IR reflections on the sample surface. The FLIR SC7600 camera has a resolution of 640x512 pixels and can record with a frame rate of 100 Hz. The camera detects IR radiation in the band of 3.4 to 4.9 µm and the reading can thus be influenced by CO_2 in the atmosphere. The full list of specifications of the FLIR SC7600 is shown in appendix C. The signal generator is controlled by the computer with the DisplayImg software from Edevis GmbH. This software is also used to record the IR data during the experiment. The experiments are conducted at NLR Marknesse in the Aerospace Vehicles Test House (AVTH) Optical Lab.

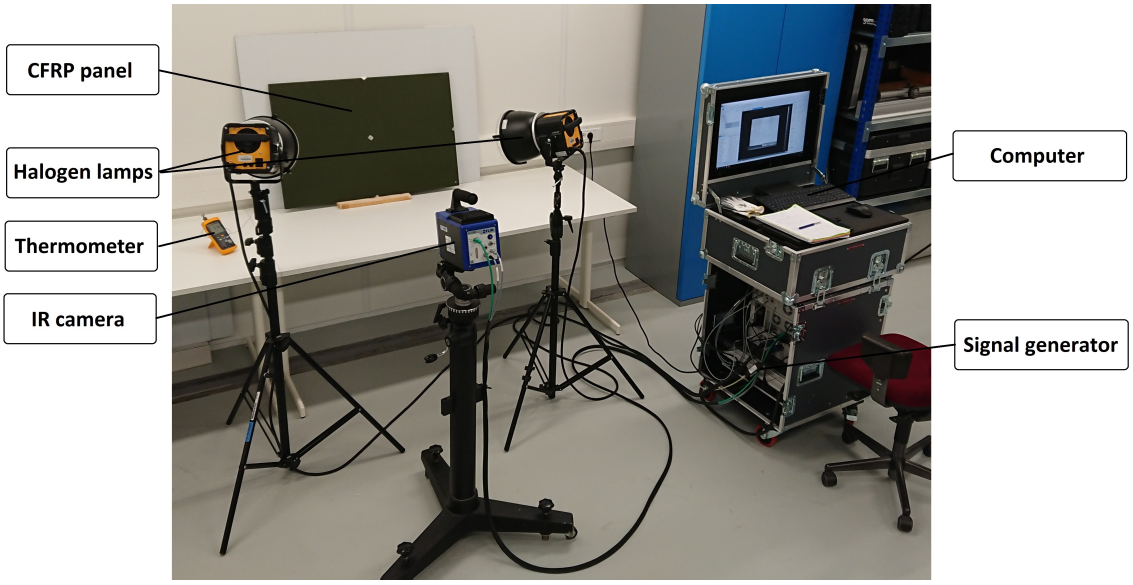

Figure 3.2: *The experimental set-up.*

The spatial resolution of IR thermography is theoretically limited by the wavelength of the detected light [75]. However, for the aerospace NDT application of inspecting large surfaces this is no real limitation since 3.4 to 4.9 µm is far smaller than needed for an acceptable defect detection. The resolution of the IR camera and the distance to the test sample limit the spatial resolution of the images. With the FLIR SC7600 camera, the spatial resolution is approximately 0.6 mm at 1000 mm distance. In order to scan the entire sample, a distance of 2250 mm is required resulting in a spatial resolution of approximately 1.35 mm.

The NTP-A1 and NTP-A2 samples used in the experiments are made from Hexcel HexPly M18/1 G939 prepreg. This material has a mass density of approximately 1,528 kg/m^3 with a fibre volume percentage of 55% after curing [76]. The exact thermal properties of the material are unknown. The dimensions, defects and inserts of the NTP-A1 and NTP-A2 samples can be seen in Figure 3.3a and 3.3b respectively. The samples contain both artificial defects consisting of teflon coated glass inserts (Tygavac TFG 075/1) and impact damages. Teflon coated glass fabric is a relatively hard to detect material in a CFRP panel since the (thermal) properties are similar to the properties of the CFRP. Detecting tape or foil inclusions is primarily of importance in a production environment. Since teflon inserts are relatively hard to detect, it can be considered a good performance indicator for thermographic NDT methods.

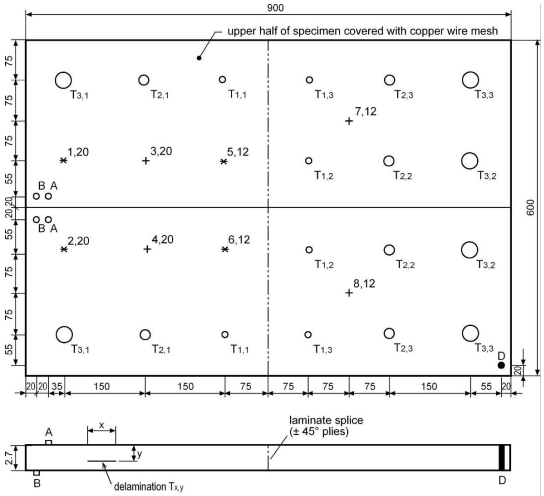

Defect type	
Delamination Tx,y	x = 1, 2 or 3 Diameter 0.25; 0.5 or 1.0 inch y = 1, 2 or 3 Depth 0.7; 1.4 or 2.0 mm
Impact +x,y *x,y	+/* Impactor tup diameter 0.5/1.0 inch x = Impact number; y = Impact energy [J]
Adhesive sticker	A ∅ 8 mm on top side of laminate B ∅ 8 mm on bottom side of laminate
Hole D	∅ 8 mm

(a) Description of the NTP-A1 sample.

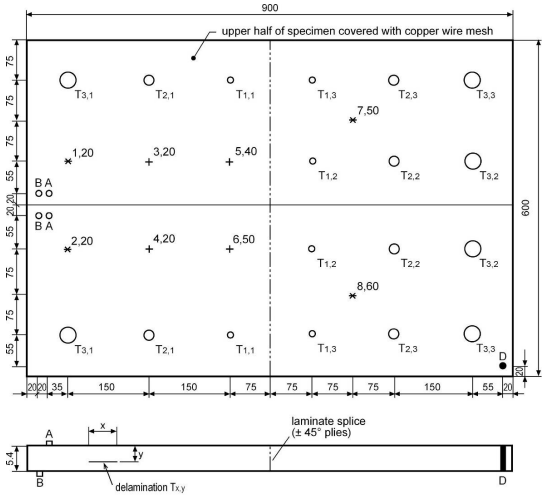

Defect type	
Delamination Tx,y	x = 1, 2 or 3 Diameter 0.25; 0.5 or 1.0 inch y = 1, 2 or 3 Depth 0.7; 3.4 or 4.7 mm
Impact +x,y *x,y	+/* Impactor tup diameter 0.5/1.0 inch x = Impact number; y = Impact energy [J]
Adhesive sticker	A ∅ 8 mm on top side of laminate B ∅ 8 mm on bottom side of laminate
Hole D	∅ 8 mm

(b) Description of the NTP-A2 sample.

Figure 3.3: *The solid CFRP panel samples.*

Experiments are conducted for each thermography method. However, not all parameters from Figure 3.1 can be varied experimentally, numerical simulations are therefore required. These simulations are discussed in section 3.3.

3.3 Simulations

Since the differential equation describing the three dimensional heat flow (Equation 2.5) is too complex to solve analytically, a numerical analysis is used. The numerical analysis is conducted using implicit FEM simulations in Abaqus from Dassault Systemes [77]. All teflon insert defects in the NTP-A1 and NTP-A2 samples are circular as can be seen in Figure 3.3. By using the double symmetry of a circular defect, the model can be restricted to a quarter of the defect. Different geometry sizes have been compared, resulting in no significant difference in temperature and phase. To save computational time, the smallest geometry is used with a size of 25x25x5.4 mm. A transient heat transfer model is used with 8-node linear brick elements.

The defect is modelled with four layers of elements with the material properties of either teflon coated glass, kapton tape or a thin air gap from Table 3.1. The tape or foil inserts are consolidated in the composite due to the curing process, resulting in a solid connection to the composite. The air gap is also modelled as a solid since the Knudsen number N_{kn} is much smaller than 1, allowing the gas gap to be modelled with Fourier's law of heat conduction [78]. The Knudsen number N_{kn} is described by the ratio between the mean free length of the gas molecules (= 0.064 µm for air [78]) and the mean gap thickness (taken at 37.5, 75 and 150 µm in the simulations).

The rest of the elements are modelled with orthotropic material properties with a lower thermal conductivity in the thickness (x) direction to simulate the orthotropic behaviour of the composite material. To simulate the process on the painted front side of the samples, the surface coating is integrated in the model by adding two layers of elements to the top surface with the material properties of the coating that are listed in Table 3.1. The coating has a total thickness of approximately 30 µm. The exact coating specifications of the samples are classified due to military applications.

Different meshes are used for the different defect sizes and depths. The sizes (⌀6.35, ⌀12.7 and ⌀25.4 mm) and depths (0.7, 1.4, 2.0, 3.4 and 4.7 mm) of the NTP-A1 and NTP-A2 samples are used. The model for defect $T_{3,1}$ of sample NTP-A2 (⌀25.4 mm teflon insert at a depth of 0.7mm from the coated front surface) is meshed with 178,560 8-node elements with in total 188,595 nodes. This mesh and the coordinate system orientation is shown in Figure 3.4.

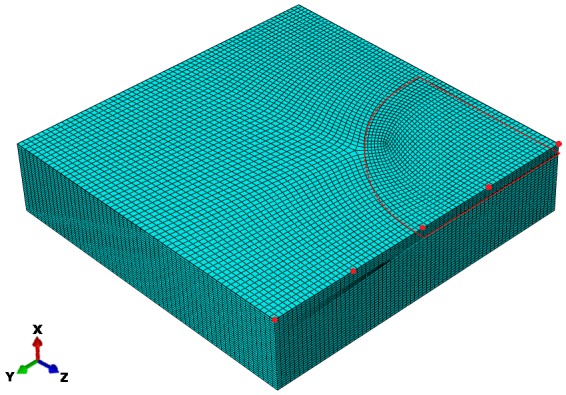

Figure 3.4: *The FEM mesh used in the simulations. The defect is highlighted with the red dashed line and the measurement locations with the 5 red dots.*

In the simulation model, the initial condition of all nodes is set to 20 °C, being approximately equal to the temperature in the experimental environment. The top surface is used for the heat deposition using a time dependent heat flux. The time dependent heat flux signal differs for the different thermography methods.

All other boundaries of the sample are considered isolated meaning that no heat flux is present perpendicular to the boundary surfaces. This is a valid assumption for the two symmetry planes. In reality the heat at the rear side of the object will be transferred to the environment, either connected objects or air through radiation, conduction and convection. The other boundaries can be assumed isolated since the distance to the defect is large enough for the lateral heat flow to be negligible at these boundaries. With uniform heating of the front surface the heat theoretically only flows in the thickness direction in areas without defects.

The result of the simulation is the temperature of all nodes as a function of time. The nodes of the top surface represent the temperature of the top surface measured by the IR camera. Only the relevant nodes are evaluated as is indicated with red dots in Figure 3.4. The 5 relevant nodes on the top surface are:

- Center of the defect
- Half the radius of the defect
- Edge of the defect
- Middle between edge defect and edge object
- Edge of the object

Concluding on the model, the following assumptions are made in the numerical simulation model:

- Orthotropic heat conductivity in the composite material. High conductivity in plane (fiber direction) and low conductivity in through-thickness direction.
- Heat deposited by the halogen lamps is a uniform heat flux at the top surface of the sample.
- Isolated sample, no heat transfer (radiation, convection and conduction) with the surrounding (with the exception of the inwards heat flux at the top surface).
- The defect shape is double symmetric, therefore only 1/4th of the defect and surrounding is modelled.

- The temperature change in the material is in the range of 1-20 K, therefore the temperature dependency of the material properties is neglected.
- The connection between the defect material and the CFRP is assumed to be consolidated perfectly.
- The air gap is modelled as solid according to Fourier's law of heat conduction since the Knudsen number N_{kn} is much smaller than 1.

3.4 Data processing

The data processing of the experiments and simulations is relatively similar. The main difference is the amount of data that is used. During the experiments, the data is collected in the form of a multi-page TIFF file. Each page in the TIFF file contains one IR image with a resolution of 640x512 pixels. The experiments are performed at a sampling frequency of 10 Hz. Since the data processing is done for each pixel separately, this results in 327,680 datasets with a length of 10 times the total measurement duration. From the simulations, the temperature signal is only extracted for 5 spatial points on the top surface. The simulation step time is varied based upon the modulation frequency used to limit the computational effort required.

Reference regions are selected manually to obtain a difference in the characteristics between a defect and a non defect region. In the experiments four reference regions are taken directly surrounding the defect (an example can be seen in Figure 4.3a). In the simulations, the two data points outside the defect region are used as reference region.

The data of both the experiments and the simulations is processed using MATLAB. For the different thermography methods, the data is processed using different algorithms. The two main techniques used are the Fast Fourier Transform (FFT) and Cross Correlation (CC). Both techniques are applied on pixel-level, evaluating each pixel separately. A schematic overview of the data processing steps can be seen in Figure 3.5 and 3.6 for FFT and CC respectively. In both methods, a reference signal $s(t)$ is used to perform a measurement (either a simulation or experiment) resulting in the perceived signal $h(t)$.

The surface temperature of the test object increases with an AC and a DC component as can be seen schematically in Figure 2.7b. For the analysis of the data, we are only interested in the AC component since this component contains the frequency information. By using a least-squares polynomial fit, a second order polynomial is removed from the data to obtain the de-trended signal.

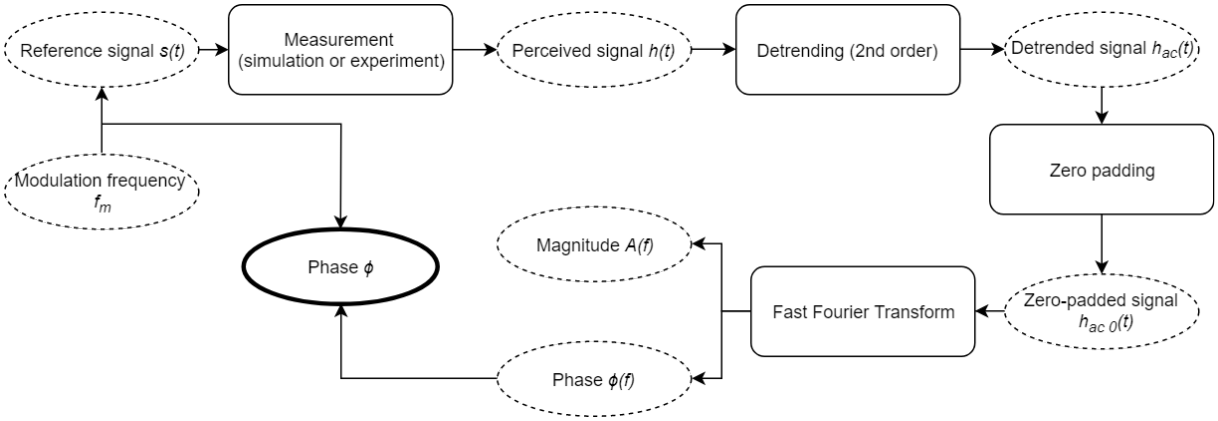

Figure 3.5: *The steps in the data processing of frequency domain analysis.*

The Fast Fourier Transform is an efficient algorithm for calculating the Discrete Fourier Transformation of a finite discrete signal. Using the FFT algorithm requires the discrete signal to have N data points with N being a power of 2. Since round sample frequencies and measurement durations are used in

both the experiments and the simulations, a method called zero padding is applied. This method refers to adding zeros to the end of the time-domain data to increase the amount of data points. By increasing the amount of data points, the FFT frequency resolution is improved. The data obtained from the FFT is the phase and the magnitude of one pixel for a range of different frequencies. LT uses one frequency for the heat deposition, therefore we are interested in the phase and magnitude of each pixel at this frequency. In the chirp signal used in FMTWI, a range of frequencies is present. The phase and magnitude of each pixel can therefore be analysed at every frequency within the modulated range.

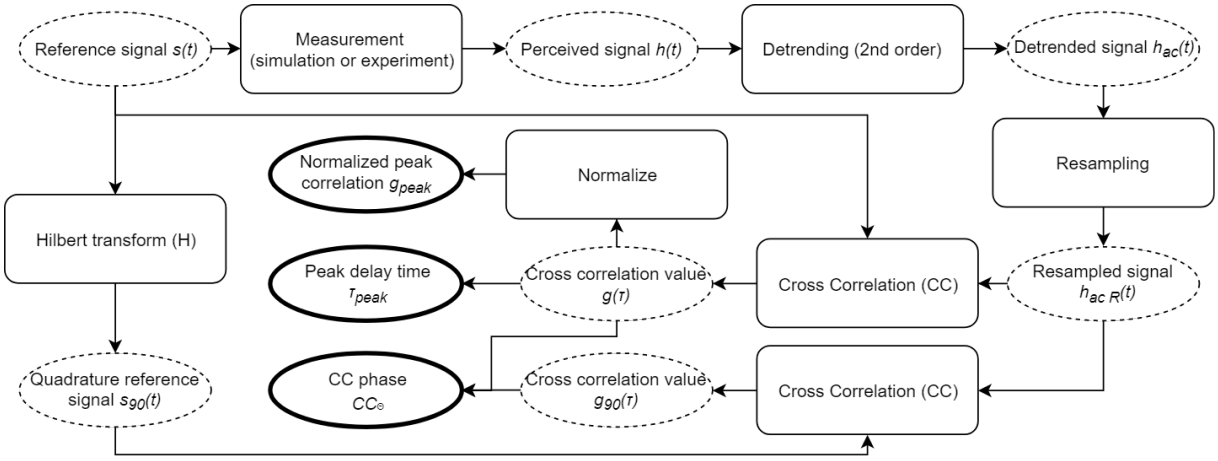

Figure 3.6: *The steps in the data processing of pulse compression analysis.*

Cross Correlation is a method to determine the similarity between two discrete signals as a function of the relative horizontal shift between the two signals. The horizontal shift in the case of time varying signals is equal to the time delay. An example of CC is given in subsection 2.3.3. The signals used in thermography for the CC correlate well at one time interval. At this time interval, the maximum correlation value occurs. The time delay at which this peak occurs and the magnitude of this peak are analysed for each pixel separately and are used for further analysis of the object. The CC signal requires processing to eliminate the dependence on the magnitude of the perceived signal. This can be done by determining the CC phase as is discussed in subsection 2.3.3.

In addition to the CC phase, a novel approach using normalization around the main lobe is applied to eliminate the dependence of the CC signal on the magnitude of the perceived signal. The correlation value is normalized around the peak with a window of plus and min two seconds. The normalization is done by setting the mean to zero and the standard deviation to one.

The objective of this research is to characterize defects with measurement data obtained with different thermography methods. Therefore part of the post-processing of the data is the characterisation of defects. The characterisation consists of determining the (depth)position, dimensions and type of defect. The different thermography methods are compared in the defect characterisation capabilities by determining the correlation between the defect depth, size and type and the obtained measurement data for each thermography method. The influence of each parameter from Figure 3.1 on the thermography results is determined after which boundaries of the thermography results are determined. By combining this range of thermography results resulting from the variation in all parameters from the lamps, camera, surface and material with the results for different types of defects, the characterisation capabilities of a method can be determined. These steps are performed for both the frequency domain analysis thermography and the pulse compression analysis thermography to determine which thermography method provides the most conclusive results about defect characters.

Chapter 4: Simulation validation

This chapter provides an overview of the method used for the validation of the numerical model. The numerical model is used to analyse the transient thermal behaviour of the sample, it is therefore not specific to a certain thermography method. The FEM model needs to be validated to check the validity and match the thermal properties of the sample. The validation of the model can be done by comparing the temperature of the sample during the experiment and the simulation. The acquisition of an accurate surface temperature is however not trivial. An IR camera obtains a Digital Intensity Level (D.I.L.) which after calibration can be used to obtain an accurate temperature measurement. The IR camera used in the experiments is not calibrated for the relevant temperature range. It is therefore decided to validate the simulation by comparing the results of the thermography process of the simulation and the experiments after data processing.

The impact damages on the NTP panels all have fibre fracture which distorts the heat flow. These impact damages are therefore easily detectable and recognizable from the cross like shape of the fibre fracture lines as can be seen in Figure 4.3. The focus in this research is on defects with a uniform thermography signature that does not allow identification based on the defects qualitative thermography signature, but requires quantitative analysis of the data. The teflon coated glass inserts of the NTP samples are defects that are not identifiable by their qualitative shape. These defects are therefore investigated in this research and used for the validation of the simulation model.

The front side of the NTP-A2 sample is used for the validation. The comparison is made with the frequency domain analysis and a sine wave signal (LT). The results of LT on 14 different frequencies are used: 0.8, 0.7, 0.6, 0.5, 0.4, 0.3, 0.2, 0.15, 0.1, 0.075, 0.05, 0.025, 0.01 and 0.005 Hz. For the validation, the three shallow defects of the NTP-A2 sample are used since these provide the biggest contrast with LT. Unfortunately the deeper located defect in the NTP-A1 and NTP-A2 panel were not detectable with the experimental set-up. An explanation for this is given in section 5.2. As discussed in section 3.1, the material thermal properties of the sample are only known within a certain range. The simulation is therefore performed with several different thermal properties to obtain a good fit. The results of the parameter fit is shown in Figure 4.1 and 4.2. This fit is obtained with the following properties; $k_l = 7$ W/mK, $k_t = 0.7$ W/mK, $\rho = 1528$ kg/m^3 and $c_p = 1100$ J/kgK. For the experiments, two measurements are performed (run 1 and run 2) and four reference regions are used as non defect region as is illustrated in Figure 4.3a, the mean of the 8 resulting lines is shown with the solid red line in Figure 4.1 and 4.2.

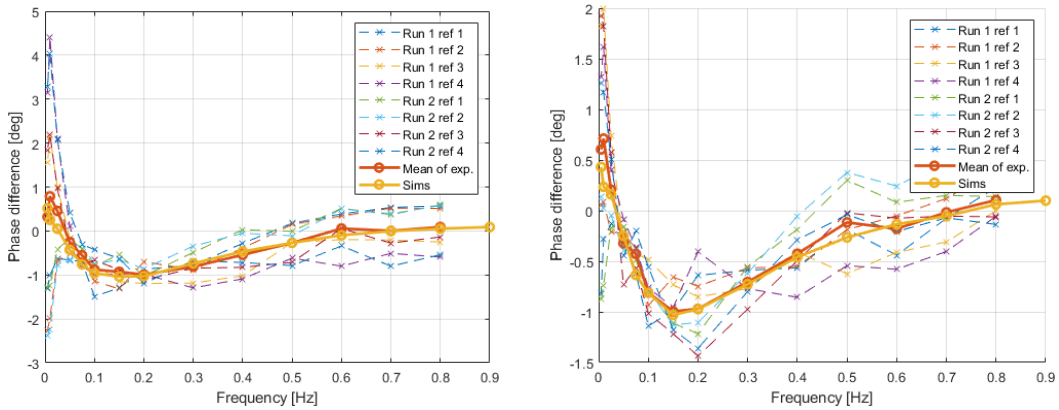

(a) *Defect $T_{3,1}$ on NTP-A2 (25.4 mm diameter at 0.7mm depth)*

(b) *Defect $T_{2,1}$ on NTP-A2 (12.7 mm diameter at 0.7mm depth)*

Figure 4.1: *Phase difference between defect and non defect regions of the coated surface at different LT frequencies, obtained with simulations and experiments. Two runs were performed with the experiment and four different reference regions are used as is shown in Figure 4.3a.*

The spread in the experimental results is a result of the noise and uneven phase over the sample in the experiment. By choosing different non defect regions as reference, the phase difference with the defect region differs due to the noise and edge effect. The four different regions used as reference for defect $T_{3,1}$ are shown in Figure 4.3a while Figure 4.3b shows the phase of the defect and non defect regions and the magnitude of the noise in the experimental results. At lower frequencies, the effect of the object edges on the heat flow and the uneven spread heat is clearly visible as can be seen in Figure 4.4. Due to this effect, selecting different reference regions results in different results. The outliers of the experimental results of defect $T_{1,1}$ (the smallest defect) in Figure 4.2 are a result of the defect being only 4-5 pixels in diameter and thus being more sensitive to noise. Overall, the trend of the simulation results and the average of the experimental results are very similar over the frequency range. It is therefore concluded that the numerical model is suited for simulating the optical thermography process.

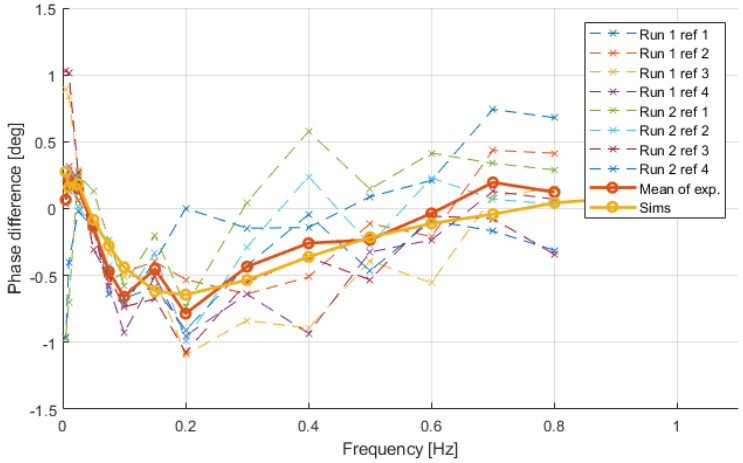

Figure 4.2: *Phase difference between healthy and defect regions of the coated surface at different LT frequencies, obtained with simulations and experiments (Defect $T_{1,1}$ on NTP-A2).*

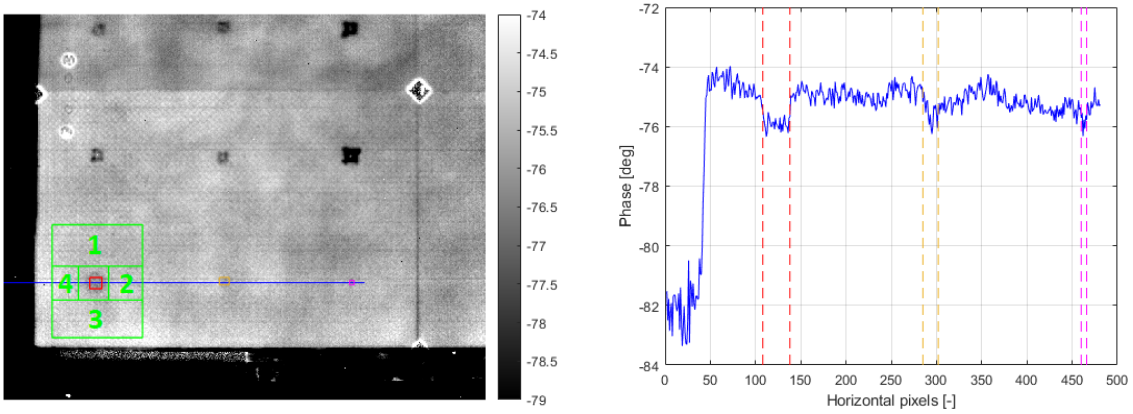

(a) *Phase image with the reference regions (1-4) for defect $T_{3,1}$, defect regions (red = $T_{3,1}$, orange = $T_{2,1}$, purple = $T_{1,1}$) and the cross-section line.*

(b) *Phase profile over blue line in Figure 4.3a with defect regions highlighted (red = $T_{3,1}$, orange = $T_{2,1}$, purple = $T_{1,1}$).*

Figure 4.3: *Experimental LT result at 0.3 Hz on the coated surface of the NTP-A2 sample (lower left quarter of the sample, cross like shape defects on the upper half of the image are impact damages).*

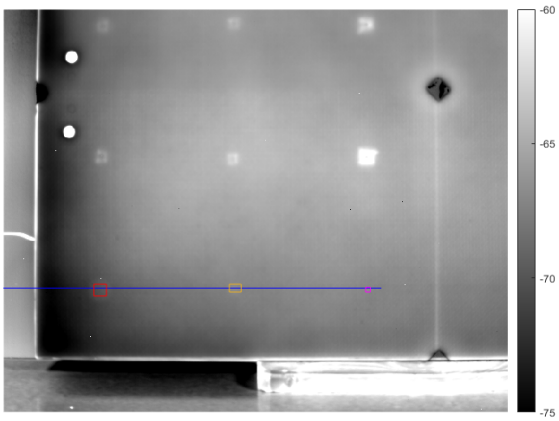

(a) *Phase image with the defect regions (red = $T_{3,1}$, orange = $T_{2,1}$, purple = $T_{1,1}$) and the cross-section line.*

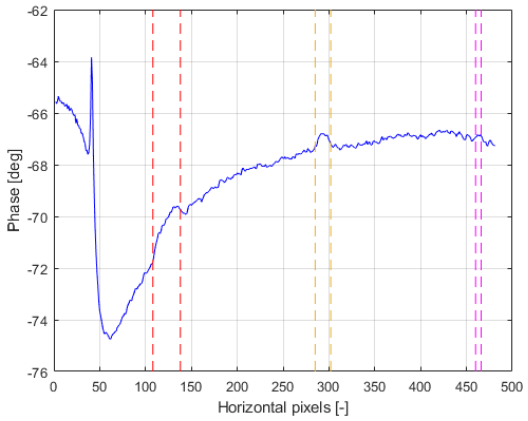

(b) *Phase profile over blue line in Figure 4.4a with defect regions highlighted (red = $T_{3,1}$, orange = $T_{2,1}$, purple = $T_{1,1}$).*

Figure 4.4: *Experimental LT result at 0.005 Hz showing the edge effect on the coated surface of the NTP-A2 sample (lower left quarter of the sample, cross like shape defects on the upper half of the image are impact damages).*

Chapter 5: Frequency domain analysis

This chapter shows the results obtained with simulations and experiments for the frequency domain analysis. The theory on frequency domain analysis thermography can be found in subsection 2.3.2. The characteristic result values are first introduced after which an analysis of the sensitivity to the parameters in chapter 3 is discussed and the discovered correlations between defect characteristics and the thermography results are shown. The final section of this chapter concludes on the findings on the thermography frequency domain analysis method and the characterisation capabilities of this method.

The data obtained from frequency domain analysis is the phase φ and the amplitude A for each pixel at the heat signal frequency. This can graphically be shown as phase or amplitude image for each frequency. Examples of phase images can be found in Figure 4.3a and Figure 4.4a at a frequency of 0.3 and 0.005 Hz respectively. The noise present in the experiments is omitted in the simulations. It is known that the amplitude data is sensitive to noise and uneven heating, therefore the amplitude data of the simulations is omitted and only the phase data is used for evaluation. LT (sine wave signal) is used for the frequency domain analysis since PPT (pulse signal) has less depth penetration capabilities and requires high power flash lamps.

It is known that the results are dependent on the frequency of the signal. By performing LT simulations at the frequencies 1.1, 0.9, 0.8, 0.7, 0.6, 0.5, 0.4, 0.3, 0.2, 0.15, 0.1, 0.075, 0.05, 0.025 0.01 and 0.005 Hz, a phase difference plot as shown in Figure 5.1a is obtained for each combination of parameters. This phase difference plot shows the phase difference with respect to a non defect region of CFRP. Although in theory a linear chirp signal would give the same results as LT, LT with a single wave is used as this provides more insight in the behaviour of the surface temperature. The phase difference obtained with a linear chirp signal is shown in Figure 5.1b.

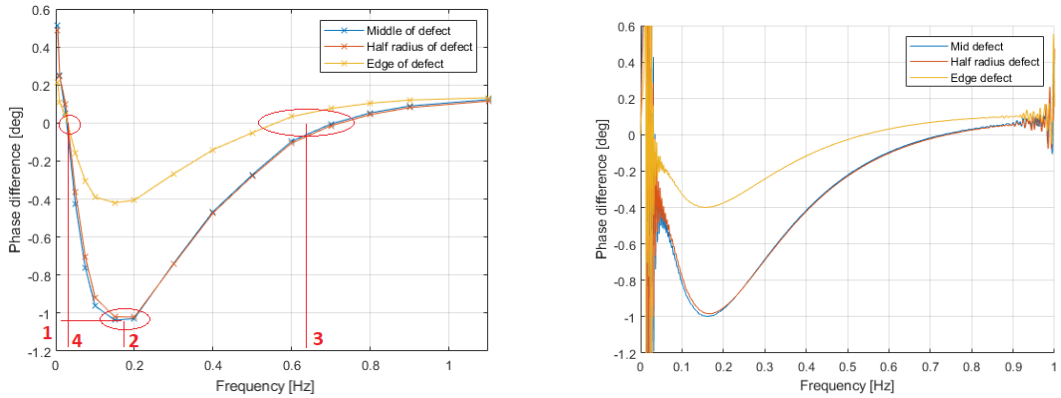

(a) *LT (sine wave signal)* (b) *FMTWI (Linear chirp signal)*

Figure 5.1: *Frequency domain thermography simulation results of defect $T_{3,1}$ of NTP-A2 (k_l = 7 W/mK, k_t = 0.7 W/mK ρ = 1,528 kg/m^3 and c_p = 1,100 J/kgK).*

Four characteristics can be obtained from the phase difference plot for each defect:

- **Peak phase difference**, max. phase difference between a defect and non defect region. (1 in Figure 5.1a)
- **Peak phase frequency**, frequency resulting in maximum phase difference. (2 in Figure 5.1a)
- **Blind frequency**, the frequency from where the defect is not detectable. Frequencies higher than the blind frequency result in a very small phase difference. (3 in Figure 5.1a)
- **Phase transition frequency**, lowest frequency resulting in zero phase difference. (4 in Figure 5.1a)

The response of these characteristics to variations of the parameters from Figure 3.1 is determined in the following paragraphs for each factor. The sensitivity of lock-in thermography to these properties is determined using the One-Factor-at-A-Time method (OFAT). The only factors that can be influenced by the set-up or the operator are the thermography method, the lamps and the camera as is graphically shown in Figure 3.1 with the green boxes. The thermography methods treated in this chapter are the frequency domain analysis methods with a long duration low peak power heat signal. The influence of the thermography method is determined by comparing the results of this chapter with the results of pulse compression thermography in chapter 7. The influence of the lamps and the camera on the characteristics listed above is determined first. The influence of the surface, the material and defect properties is determined secondly. With the sensitivity of the lock-in thermography results to all the parameters being known, the characterisation capabilities of the method are analysed in the final part of this chapter.

5.1 Effect of the lamp parameters

The parameters of the lamps that can be changed are the angle and the distance with respect to the test object and the power of the lamps. A variation in these parameters results in a different heat flux at the surface of the sample. In real world scenarios, bodies do not behave as black bodies as is treated in section 2.1. Taking into account the reflection, emissivity and absorption of bodies makes the calculation of the heat flow more complex. Determining the heat flux as a function of all variables is difficult due to its dependence on the emissivity of the halogen lamps and the absorbance and reflectance of the sample surface. Accurate measurements of these properties are far from trivial. It is therefore decided to obtain an estimate for the heat flux by measuring the temperature of the front and rear surface of the sample while heating the sample with 20 s pulses of the halogen lamps. The temperature of the front and rear surface is measured using thermocouples. The thermocouple on the front surface is covered with a small piece of insulating material and reflective tape to prevent radiation heat from the halogen lamp from directly heating the thermocouple.

The experiment is performed with varying power of the lamps, ranging from 500 W to 4,000 W in steps of 500 W. In the experiment the lamps are placed at a distance of 800 mm from the surface at an angle of 45 degree towards the surface to create an open view for the IR camera. By assuming a uniform temperature in the sample when the temperature of the front and rear surface are equal, the result in Figure 5.2 is obtained. The coating is only 30 µm thick, the thermal capacity of the coating is therefore neglected for the power estimation. By using the dimensions and thermal properties of the material, the energy absorbed by the object can be estimated. In reality the object will emit heat through both radiation and convection. However, this effect is omitted here to obtain a heat flux that results in representative temperature differences in the simulations because the natural convection and outward radiation are omitted from the simulations. In the rest of the experiments, 75% of the total lamp power is used to extend the service life of the halogen lamps. 3,000 W power of the lamps results in a representative heat flux of approximately 520 W. This heat flux reference is only valid for the coated surface of the NTP-A1 and NTP-A2 samples.

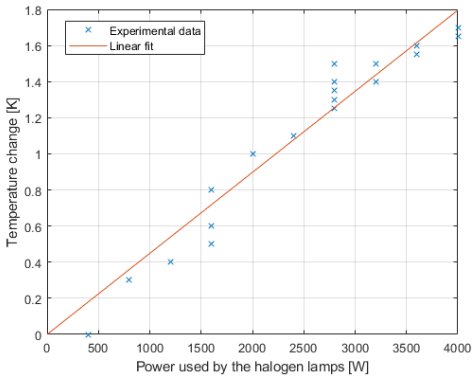

Figure 5.2: *Temperature change of the NTP-A2 panel due to a 20 s pulse heat deposition as a function of the lamp power.*

The influence of the heat flux variations on the thermography results is determined by performing simulations of one defect at three different power levels of the lamps, 75 %, 100 % and 150 %. It is trivial that the heat flux heavily influences the surface temperature as can be seen in Figure 5.3. However after processing the data, the same phase difference is obtained for all three excitation levels since the phase is independent of the magnitude. This is confirmed by performing experiments at 50 %, 75 % and 100 % lamp power. The results of these experiments are shown in Table 5.1. Increasing the power does result in a higher signal to noise ratio (SNR), which is determined by Equation 5.1.

$$SNR = |\frac{\mathrm{S}}{\sigma}| \tag{5.1}$$

In this equation S is the difference in phase between a defect and a non defect region and σ is the standard deviation of the non defect (reference) region. The SNR is an indicator for the detectability and contrast of a defect. For phase images with an even phase of the non defect regions, a threshold value could be used to identify defects. Using a threshold value would require a SNR larger than 1. In experiments this is however not trivial since the phase of non defect regions is not equal over the entire surface as can be seen from Figure 4.3b and 4.4b.

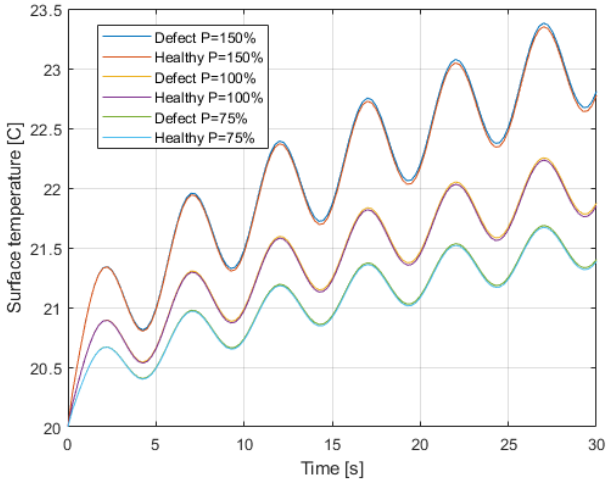

Figure 5.3: *The surface temperature as a function of time for the defect $T_{3,2}$ of NTP-A2 with k_l = 7 W/mK and k_t = 0.7 W/mK at three different heat flux with a frequency of 0.2 Hz and 6 cycles.*

Table 5.1: *Phase difference and SNR of 3 runs at 0.2 Hz with 6 cycles.*

	Power	***50%***			***75%***			***100%***		
⌀ [mm]		Run 1	Run 2	Run 3	Run 1	Run 2	Run 3	Run 1	Run 2	Run 3
25.4	**d**φ [deg]	-1.011	-0.951	-0.984	-0.942	-1.022	-0.975	-0.989	-1.061	-1.041
	SNR [-]	0.52	0.96	1.01	1.87	1.88	1.61	1.44	1.66	1.85
12.7	**d**φ [deg]	-0.949	-0.949	-0.898	-0.951	-0.904	-0.917	-0.995	-0.829	-0.957
	SNR [-]	0.62	1.19	1.38	2.24	1.60	1.64	2.52	2.12	2.42

5.2 Effect of the camera parameters

Both the spatial resolution and the thermal resolution of the camera used in thermography can influence the results. The spatial resolution mostly influences the ability to accurately determine the lateral size of defects, this parameter is treated later in this chapter. The thermal resolution of the camera used in a thermography set-up is a limiting factor for the detectability of deeper defects or defects with thermal properties very similar to the thermal properties of the material. Both cases result in a very low temperature difference between the top surface above a defect and a non defect region. By increasing the heat flux, a larger temperature difference can be obtained. In the simulations all defects up to 4.7 mm depth are detectable. With the small temperature difference, there is still a phase difference. Two sine-waves with a small phase difference, have a small difference in the instantaneous amplitude. The detectability limit of the difference in the instantaneous amplitude is the thermal resolution of the camera.

The mean and maximum temperature difference over 6 frequency periods (at 0.2Hz, similar to the temperature profile in Figure 5.3) is obtained and shown graphically in Figure 5.4. In this figure it can be seen that the temperature difference between the defect and non defect regions is very small. The FLIR SC7600 camera used in the experiments has a thermal resolution of < 20 mK which is shown as the threshold line in Figure 5.4. It can clearly be seen that both the mean and max temperature differences for most defects located deeper than 0.7 mm are below the 20 mK threshold. This means that difference in the surface temperature above a defect and a non-defect region is not identifiable with the IR camera. This results in an unidentifiable phase difference between defect and non defect regions.

The detectability in the experiments is also influenced by the noise reducing the detectability even further. This results in the poor detectability of the 25.4 mm defect at 1.4 mm in experiments even though the maximum temperature difference in the simulation exceeds 0.02 K at low frequencies.

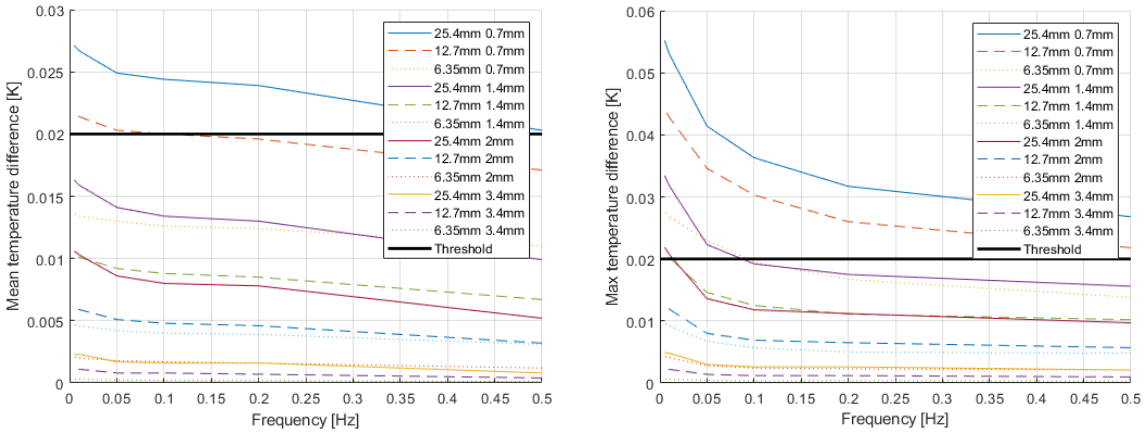

(a) *Mean temperature difference* (b) *Max temperature difference*

Figure 5.4: *The surface temperature difference between defect region and non defect regions obtained from simulations with a teflon coated glass insert of different sizes at different depths.*

The temperature difference can be increased by enlarging the power applied to the surface as can be seen in Figure 5.5 in which the power is varied on the 25.4 mm defect located at 1.4 mm depth.

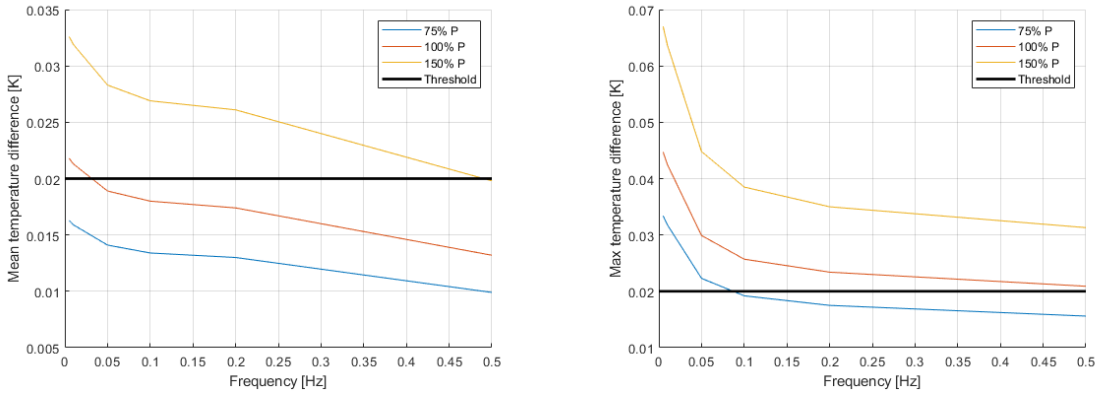

(a) *Mean temperature difference* (b) *Max temperature difference*

Figure 5.5: *The surface temperature difference between defect region and non defect regions obtained from simulations with a 25.4 mm teflon coated glass insert at 1.4 mm depth with varying lamp power.*

5.3 Effect of the surface parameters

The samples used for the experiments have a matte green military coating of 30 µm. Civil aircrafts in general use a thicker coating between 88.9 and 139.7 µm [79]. Since both coatings are in general Poly Urethane (PU) coatings, the influence of the coating thickness can be compared by increasing the coating thickness in the simulation model. The result of simulations with a coating layer of 30 µm and 115 µm is shown in Figure 5.6. From these results it can be concluded that a thicker coating results in a smaller peak phase difference which is also shifted to a lower frequency. However, the thickness of a coating can be measured using different methods, for example an ultrasonic thickness gauge [80].

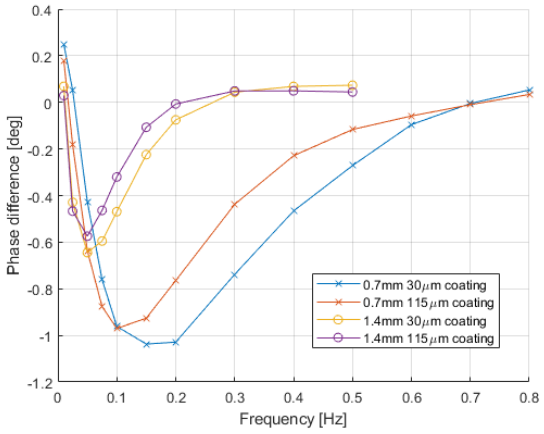

Figure 5.6: *The phase difference for a 25.4 mm teflon coated glass insert at 0.7 mm and 1.4 mm depth with 30 µm and 115 µm thick PU coating layer.*

Civil aircrafts generally have a reflective coating. This results in less heat being absorbed by the test object surface. As is discussed earlier in this section, lower heat deposition results in a lower SNR and thus a lower detectability of detects. A reflective coating thus might require more powerful lamps to obtain the same results.

When applying optical thermography on an object with a a reflective coating, the reflection of the lamps towards the camera can distort the results. The experimental set-up has a filter in front of the halogen lamps to filter the light for the detection bandwidth of the camera to prevent direct reflections. A reflective coating can also result in reflection of the environment behind the camera. This can be solved by covering the area behind the camera with a non IR translucent material. As discussed earlier in section 3.2, in the experimental set-up a large polycarbonate screen has been placed behind the set-up. Without this screen, significant disturbances were found in the results by for example a person moving behind the camera.

5.4 Effect of the material parameters

The material properties influence the lateral heat diffusion and the attenuation of the through-thickness heat diffusion. The material of the sample has four properties that can influence the results of thermography; the thermal conductivity in through-thickness (out-of-plane) direction k_t and in lateral (in-plane) direction k_l of the material, the specific heat capacity c_p and the mass density ρ. The exact material properties are often unknown in NDT applications and the spreading of the properties is relatively large as can be seen in Table 5.2 which is a summarized copy of Table 3.1. The range for the four material parameters differs significantly in magnitude. The range is 49% of the maximum value for ρ, 17% for c_p, 83.3% for k_l and 70% for k_t. The influence of the material properties is determined by varying the four parameters (k_t, k_l, c_p and ρ) in the ranges from Table 5.2 one at a time (OFAT). By combining the influences of the four parameters, sets of parameters resulting in minimum and maximum thermography results can be composed. These sets can then be used to determine the boundaries of the thermography results for a certain type of defect as a result of the spread of CFRP material properties. The influence is determined for a 25.4 mm diameter teflon coated glass insert at different depths. The influence of different defects is treated in section 5.5.

Table 5.2: *Material properties from literature and the NTP samples.*

Material	Property	Min.	Nom./sample	Max.	Unit
CFRP [65][66][67] [68][69][70][71]	Density	1,150	1,528	2,250	kg/m^3
	Thermal capacity	1,000	1,100	1,200	J/kgK
	Thermal conductivity in-plane	2	7	12	W/mK
	Thermal conductivity out-of-plane	0.3	0.7	1	W/mK
Teflon coated glass [66][72]	Density		2,200		kg/m^3
	Thermal capacity		1,000		J/kgK
	Thermal conductivity		0.26		W/mK
Top coating	Density		1,600		kg/m^3
	Thermal capacity		1,800		J/kgK
	Thermal conductivity		0.35		W/mK

The thermal conductivity in the out-of-plane direction k_t is varied in 5 steps within the range given in Table 5.2 for CFRP; 0.3, 0.5, 0.7, 0.9 and 1 W/mK. Simulations have been performed at a series of frequencies for each combination of defect and thermal properties. Figure 5.7 shows the increasing trend of all four characteristics of the phase difference as a function of the frequency with increasing k_t. The influence of k_t on the thermography results is rather large. The lowest value of k_t (0.3 W/mK) results in a positive phase difference. However, this result is combined with a very small temperature difference (<< 20 mK). In an experiment this would therefore most likely result in an undetectable defect while highest value of k_t results in a peak phase difference of -1.89 degree for a teflon coated glass insert at 0.7mm depth.

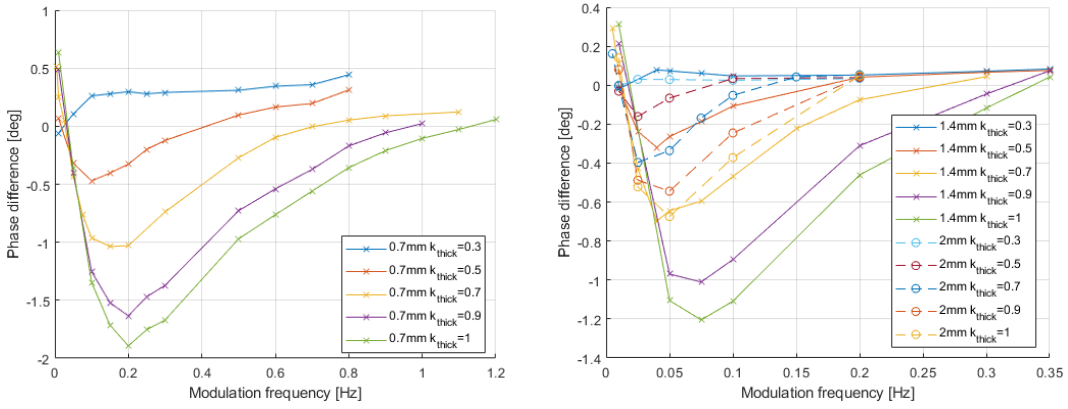

(a) *Depth of 0.7 mm* (b) *Depth of 1.4 mm and 2.0 mm*

Figure 5.7: *The phase difference as a function of the frequency for 25.4 mm teflon coated glass inserts with varying out-of-plane thermal conductivity k_t.*

The lateral heat conductivity k_l is varied in 5 steps within the range in Table 5.2: 2, 4.5, 7, 9.5 and 12 W/mK. Even though the range is significantly larger in comparison with the through-thickness conductivity k_t, the influence k_l is relatively small as can be seen in Figure 5.8. The blind frequency is not significantly influenced, however the peak phase difference is clearly influenced by the lateral thermal conductivity. At 0.7 mm depth the difference in results is small, with increasing depth the influence increases as more heat travels in lateral direction.

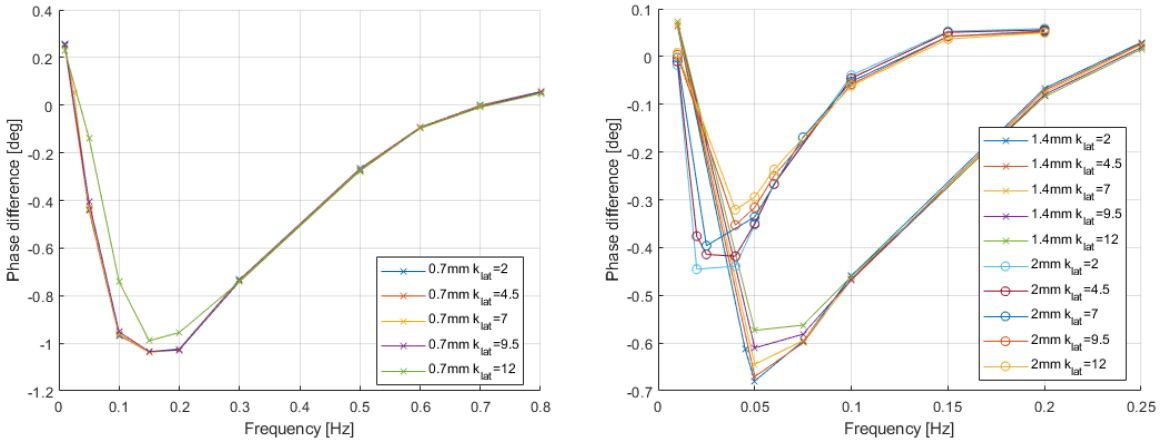

(a) *Depth of 0.7 mm* (b) *Depth of 1.4 mm and 2.0 mm*

Figure 5.8: *The phase difference as a function of the frequency for 25.4 mm teflon coated glass inserts with varying lateral thermal conductivity k_l.*

Both the specific heat capacity c_p and the mass density ρ are varied in 3 steps. The results of these simulations are shown in Figure 5.9. Increasing either c_p or ρ results in the same trends, the peak phase difference increases while the phase transition-, peak- and blind frequency decrease. The magnitude of the variation of the thermography results is proportional with the range of the values for both properties. Since ρ has a wider range, this property results in a larger variation of the thermography results.

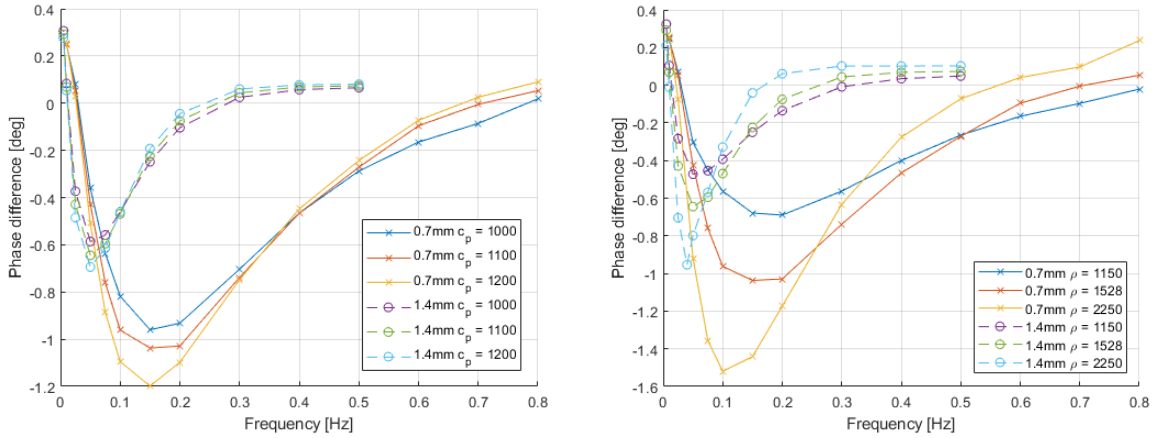

(a) *Varying specific heat capacity c_p of the CFRP* (b) *Varying mass density ρ of the CFRP*

Figure 5.9: *The phase difference as a function of the frequency for 25.4 mm teflon coated glass inserts.*

The material properties can be combined in the thermal diffusivity α_t and α_l for the two orthogonal directions respectively. The thermal diffusivity α_i is described by Equation 5.2.

$$\alpha_i = \frac{k_i}{\rho c_p} \tag{5.2}$$

The thermal diffusivity α of a material is a measure for the rate of heat transfer from hot to cold inside a material. Since the through-thickness direction of heat travel is the most important for defect detection with thermography, the influence of the k_t, c_p and ρ on the thermography results is determined as a function of α_t. By varying the thermal properties of the material, the thermal diffusivity changes. The thermal diffusivity for each of the parameter combinations used in the simulations of Figure 5.7, 5.8 and 5.9 is given in Table 5.3. The combination of k_t = 0.7 W/mK, c_p = 1,100 J/kgK and ρ = 1,528 kg/m^3 is the combination fitted to the NTP-A1 and NTP-A2 samples in chapter 4.

Table 5.3: *The thermal diffusivity variations from the simulations.*

	k_t [W/mK]	c_p [J/kgK]	ρ [kg/m^3]	α_t [10^{-6} m^2/s]	
Varying k_t	**0.3**	1,100	1,528	0.179	
	0.5	1,100	1,528	0.298	
	0.7	1,100	1,528	0.417	Fit (ref)
	0.9	1,100	1,528	0.536	
	1	1,100	1,528	0.595	
Varying c_p	0.7	**1,000**	1,528	0.458	
	0.7	**1,100**	1,528	0.417	Fit (ref)
	0.7	**1,200**	1,528	0.382	
Varying ρ	0.7	1,100	**1,150**	0.553	
	0.7	1,100	**1,528**	0.417	Fit (ref)
	0.7	1,100	**2,250**	0.283	

The correlation between the four characteristic values of LT and the thermal diffusivity α_t is shown in Figure 5.10 and 5.11. These figures provide a more clear overview of the trend in the data from Figure 5.7 and 5.9. Each line in Figure 5.10 and 5.11 represents a variation in one of the three parameters; thermal conductivity k_t, thermal capacity c_p and mass density ρ. The values for α_t for each of these variations can be found in Table 5.3. The main trend that can be observed in Figure 5.10 and 5.11 is the increasing value of the characteristics with increasing thermal diffusivity α_t. There is however a deviation from this trend with the influence of the thermal capacity c_p and the mass density ρ on the peak phase difference in Figure 5.10a. While c_p and ρ have a negative correlation with the thermal diffusivity α while the thermal diffusivity α has a positive correlation with the peak phase difference. The peak phase difference is clearly not only a function of the thermal diffusivity α. An explanation for this is given later in this section.

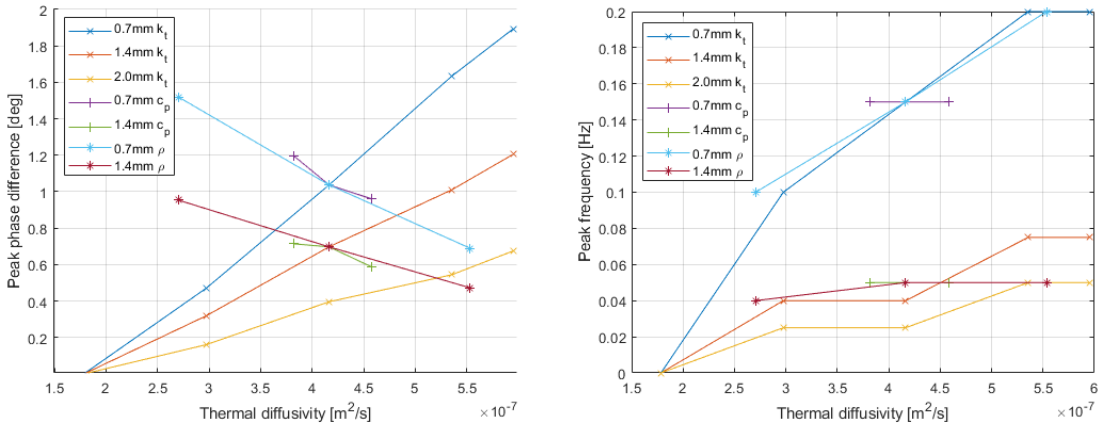

(a) *Peak phase difference* (b) *Peak phase frequency*

Figure 5.10: *The characteristics for 25.4 mm teflon coated glass inserts with varying thermal diffusivity α_t as a result of varying k_t, ρ and c_p (the values of α_t can be found in Table 5.3).*

It must be noted that the frequencies in Figure 5.10b, 5.11a and 5.11b are based on discrete steps in frequency as a result of the LT process being bounded to a single frequency resulting in discrete steps in the frequencies.

The blind frequency correlates to approximately 1.5 to more than 2 times the penetration depth μ as is discussed in section 2.3 (see Equation 2.21). Since the penetration depth is a function of α, there is a relation between the blind frequency f_b and the thermal diffusivity α. This relation and the results from the simulation can be seen in Figure 5.11a. The limited difference in thermal properties of the defect material and the CFRP material results in the deviation of the theoretical value at low thermal diffusivity values as this is similar to the diffusivity of the teflon coated glass ($= 0.182 \cdot 10^{-6}$ m^2/K) resulting in an undetectable defect. The influence of the defect properties is described later in section 5.5.

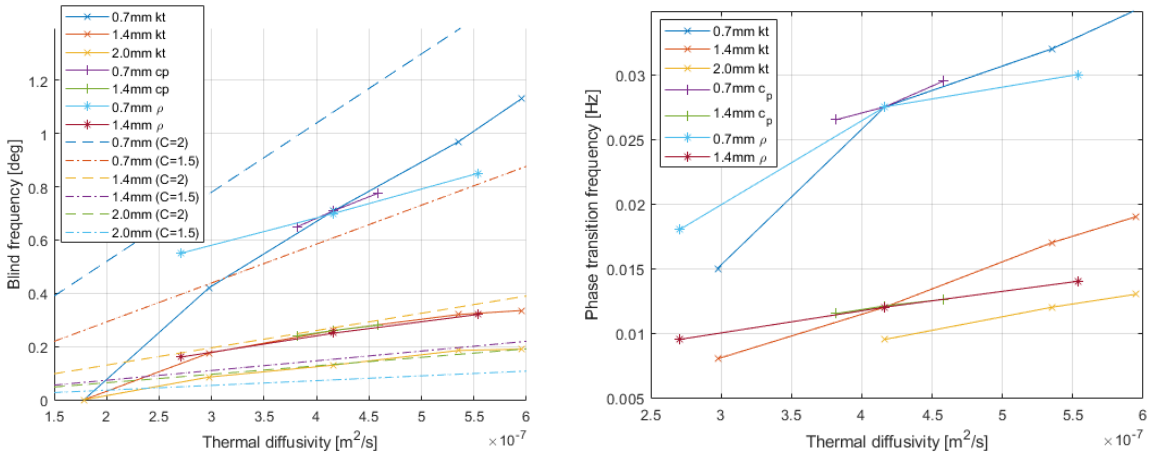

(a) *Blind frequency, the dotted lines represent the theoretical values from Equation 2.21.*

(b) *Phase transition frequency*

Figure 5.11: *The characteristics for 25.4 mm teflon coated glass inserts with varying thermal diffusivity α_t as a result of varying k_t, ρ and c_p (the values of α_t can be found in Table 5.3).*

The opposite trend of the peak phase difference with respect to increasing k_t and c_p and ρ in Figure 5.10a suggests that it might be related to the thermal effusivity e which is described by Equation 5.3 as is discussed in section 2.2.

$$e = \sqrt{k\rho c_p} \tag{5.3}$$

The effusivity of the material and the effusivity of the defect determine the reflection of the thermal waves. The percentage of thermal waves reflecting while travelling from material 1 to material 2 is described by Equation 5.4 as is discussed in section 2.2.

$$R_{12} = \frac{e_1 - e_2}{e_1 + e_2} = \frac{\sqrt{k_1\rho_1 c_{p1}} - \sqrt{k_2\rho_2 c_{p2}}}{\sqrt{k_1\rho_1 c_{p1}} + \sqrt{k_2\rho_2 c_{p2}}} \tag{5.4}$$

The relation between the peak phase difference and the effusivity e and the reflection R can be seen in Figure 5.12a and 5.12b respectively. The important difference between the effusivity e of the CFRP material and the reflection coefficient R is the dependence on the defect material properties of the latter.

The combination of all four material parameters leads to the boundaries of the spread in the thermography results for a certain type of defect. Since in NDT scenarios the exact material parameters are often not known, it must be determined in what range a defect can be characterized with the characteristics of a series of LT measurements without the exact CFRP material properties. Since two different trends are observed in the behaviour of the characteristics with varying material properties, two different sets of boundary CFRP material properties can be determined.

The first set of boundaries is based on the peak phase difference. The peak phase difference is the main result obtained from lock-in thermography as it determines the detectability of a defect. The maximum phase difference is obtained with the lowest k_l and the highest k_t, ρ and c_p. The minimum phase difference is obtained with the opposite properties. These parameter sets are shown in Table 5.4.

The second set of boundaries is based on the window of frequencies with which the defect can be detected. This window is determined by the blind frequency. The lowest blind frequency and thus the smallest detection window is obtained with the lowest thermal conductivities k_l and k_t and the highest ρ and c_p. The highest blind frequency is obtained with the opposite of these properties. These parameter sets can be found in Table 5.5.

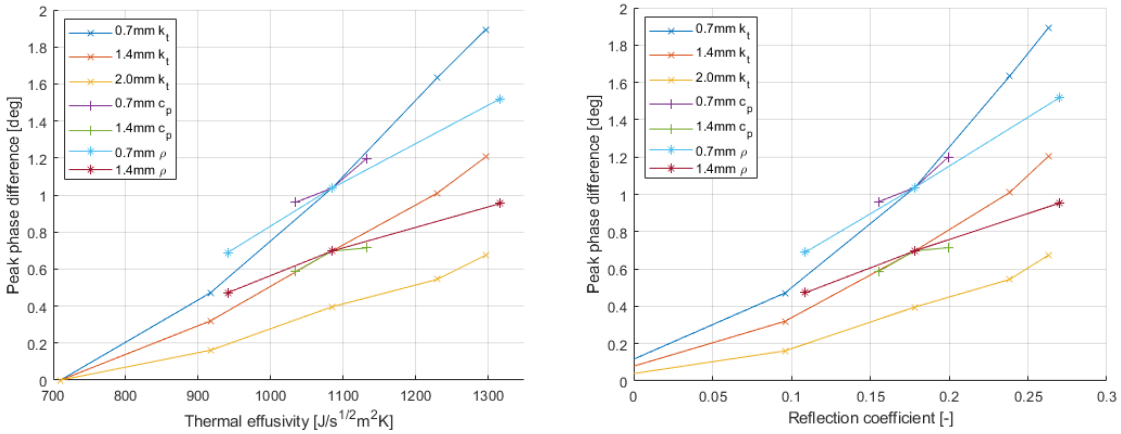

(a) *As a function of the effusivity e.* (b) *As a function of the reflection coefficient R.*

Figure 5.12: *The peak phase difference for 25.4 mm teflon coated glass inserts varying k_t, c_p and ρ.*

Table 5.4: *The parameters resulting in minimum and maximum detectability of a teflon coated glass insert.*

Parameter	k_t	k_l	ρ	c_p
Unit	[W/mK]	[W/mK]	[J/kgK]	[kg/m^3]
Min. detectability	0.3	12	1,150	1,000
Fitted parameters (NTP-A1 and NTP-A2 panels)	0.7	7	1,528	1,100
Max. detectability	1	2	2,250	1,200

Table 5.5: *The parameters resulting in the narrowest and widest detection window of a teflon coated glass insert.*

Parameter	k_t	k_l	ρ	c_p
Unit	[W/mK]	[W/mK]	[J/kgK]	[kg/m^3]
Narrow window	0.3	2	2,250	1,200
Fitted parameters (NTP-A1 and NTP-A2 panels)	0.7	7	1,528	1,100
Wide window	1	12	1,150	1,000

Simulations are performed with the range from Table 5.4, resulting in maximum and minimum phase difference. By evaluating the maximum absolute phase difference for each combination of the 3 different defect sizes and 4 depths, the data in Figure 5.13 is obtained. It can clearly be seen that there is a correlation between increasing defect depth and the decreasing phase difference. The phase difference however is also heavily influenced by the material properties, the phase difference for a teflon coated glass insert located at 0.7 mm depth varies between 0 and 2.46 degree depending on the material properties. The difference between the phase difference with properties leading to maximum detectability and the nominal properties (that are fitted to the NTP samples) is approximately a factor 2 to 3 depending on the defect size and depth. This dependence on the material properties can be seen in Figure 5.13b in which the maximum phase difference is plotted against the reflection coefficient R from Equation 5.4.

Since all simulations are performed with the same defect, the only variation is in the material properties of the CFRP. The lower value of R corresponds to the minimum detectability properties in Table 5.4 while the highest value of R corresponds to the maximum detectability properties in the table. It is clear that no decisive conclusion about the defect can be drawn solely based on the maximum absolute phase difference without knowledge on the exact CFRP material properties of the object.

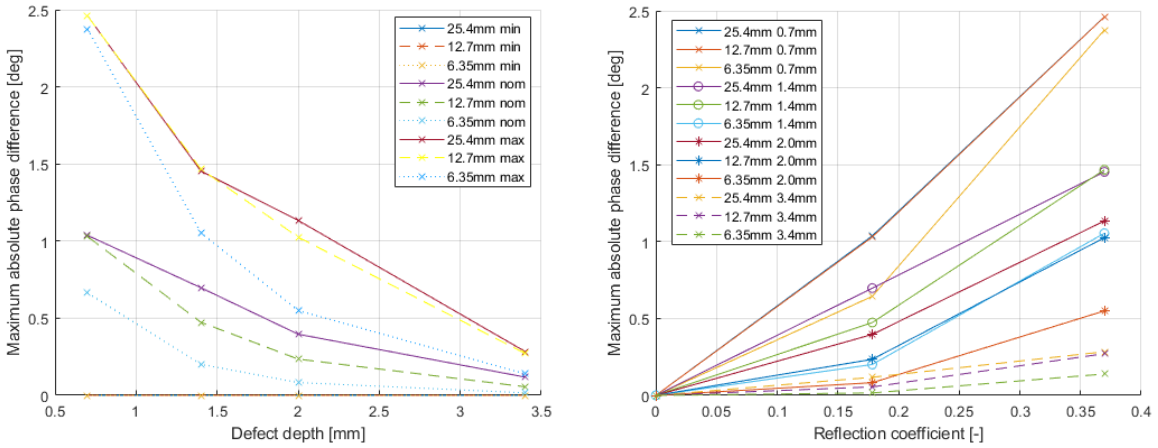

(a) *As a function of the depth d.* (b) *As a function of the reflection coefficient R.*

Figure 5.13: *Peak phase difference with different teflon coated glass defect sizes, depths and CFRP properties from Table 5.4.*

By performing simulations with the properties resulting in the narrowest and the widest detection windows (as is defined in in Table 5.5), the minimum and maximum blind frequency f_b for a glass coated teflon insert of 0.075 mm can be determined. The results of these simulations is shown in Figure 5.14. The evaluation of Equation 2.21 with C is 1.5, 2, 2.1 and 2.2 in combination with the minimum and maximum α_t respectively is added to Figure 5.14a. The simulation results clearly follow a similar trend as a function of the defect depth. A depth range can be obtained from this figure for a certain blind frequency f_b. The blind frequency is linearly dependent on the thermal diffusivity of the CFRP material as can be seen in Figure 5.14b. The highest thermal diffusivity α corresponds to the wide detection window properties in Table 5.5.

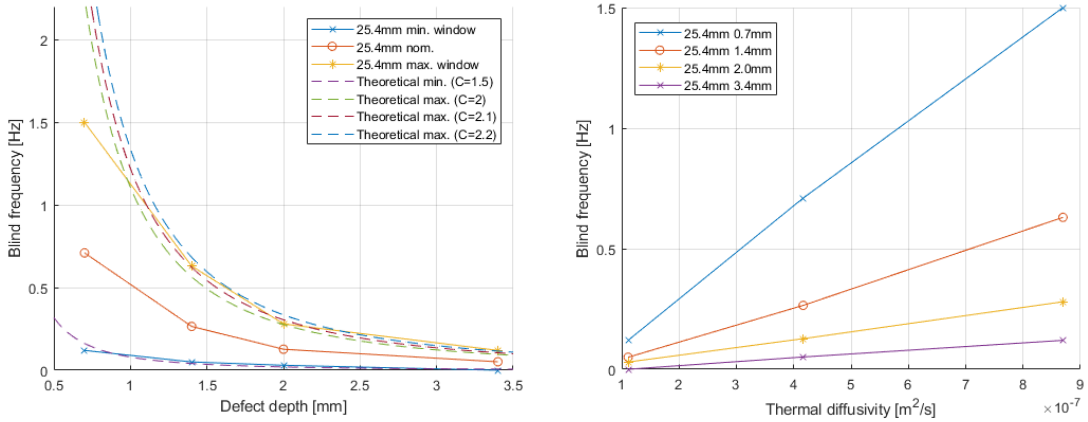

(a) *As a function of the depth d.* (b) *As a function of the thermal diffusivity α_t.*

Figure 5.14: *The blind frequency with different teflon coated glass defect depths and the CFRP properties from Table 5.4.*

Both the peak frequency and the phase transition frequency show a similar trend as the blind frequency with respect to the defect depth d and the thermal diffusivity α_t. These results are shown in Figure 5.15 and 5.16 for the peak frequency and the phase transition frequency respectively. Since these frequencies are smaller than the blind frequency, accurate determination of these frequencies is more time consuming since multiple measurements at different frequencies are required. To limit the computational effort, the simulations are done with a frequency of 0.5, 0.4, 0.3, 0.2, 0.15, 0.1, 0.075, 0.05, 0.025, 0.01 and 0.005 Hz. Additional frequencies are applied in order to determine the outliers. After these simulations the characteristic frequencies are approximately known. This results in the discrete character of Figure 5.15 and 5.16.

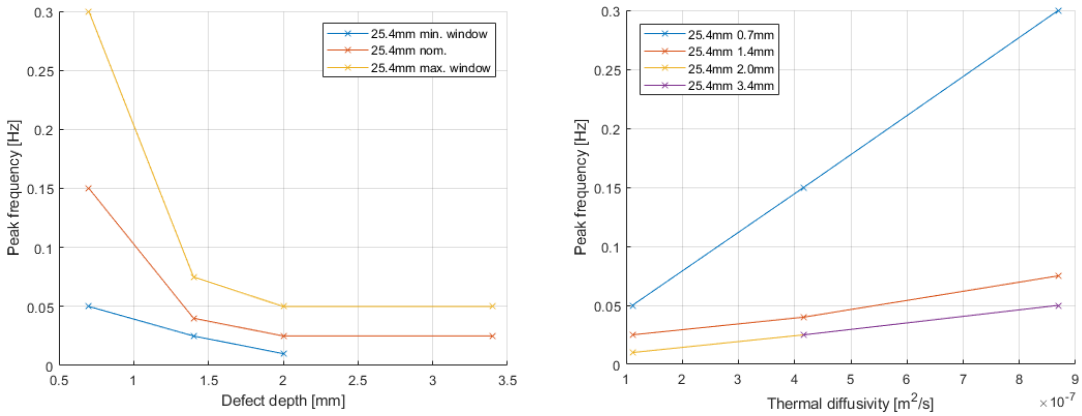

(a) *As a function of the depth d.* (b) *As a function of the thermal diffusivity α_t.*

Figure 5.15: *The peak frequency with different teflon coated glass defect depths and the CFRP properties from Table 5.5.*

The phase transition frequency is very time consuming to determine since it is the lowest characteristic frequency. Measurements at low frequencies by nature require longer measurement durations. Since accurate determination of the phase transition frequency requires multiple measurements at very low frequencies, this frequency is harder to use as a characteristic value. The peak frequency and the blind frequency are easier to determine since these frequencies are significantly higher making it far less time consuming to perform multiple measurements with frequencies around these characteristics.

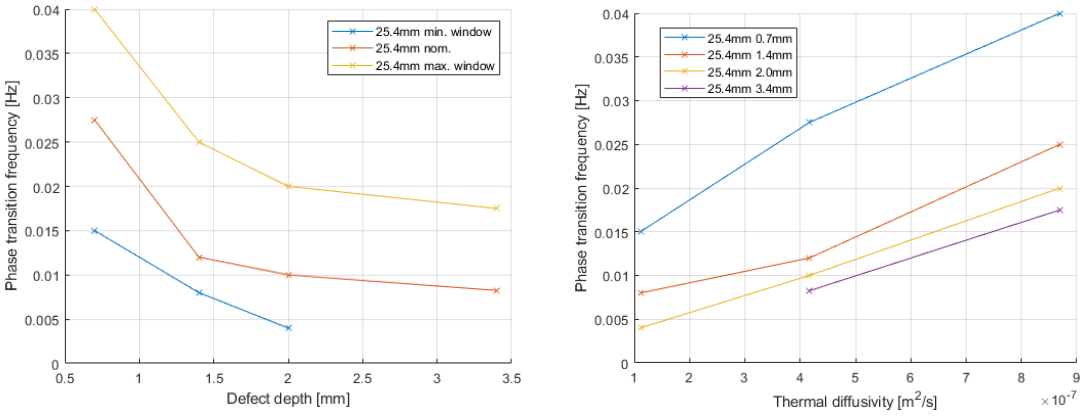

(a) *As a function of the depth d.* (b) *As a function of the thermal diffusivity α_t.*

Figure 5.16: *The phase transition frequency with different teflon coated glass defect depths and the CFRP properties from Table 5.5.*

Concluding, the material properties have a significant influence on the thermography results. Resulting in a phase difference between zero (undetectable defect) and a maximum value for a teflon coated glass insert. To determine the possibility of differentiating different types of defects with the thermography results, the influence of different types of defects is determined next.

5.5 Effect of the defect parameters

A defect in a composite panel has four parameters that can influence the thermography results. The depth with respect to the front surface, the lateral size, the material of the defect and the thickness of the defect. The simulations are based on the Teflon coated glass insert in the NTP-A1 and NTP-A2 samples. These defects are located at 0.7, 1.4, 2.0, 3.4 and 4.7 mm depth and have a lateral size of 1", 0.5" and 0.25" (25.4 mm, 12.7 mm and 6.35 mm respectively). Firstly, the influence of the depth and lateral size is shown. After which the influence of the defect material is shown with simulation results for two different types of defects. The first defect type is a kapton tape insert representing a tape accidentally left behind between plies in the production. The second type is a thin air gap to simulate a gas pocket formed in the production process or a delamination originated during in-service life. Lastly, the thickness of the defect is varied to determine the influence of this parameter.

The depth of a defect has been varied in the simulations used to determine the influence of material properties. These results can be found in Figure 5.13a, 5.14a, 5.15a and 5.16a for the peak phase difference, the blind frequency, the peak frequency and the phase transition frequency respectively. All four characteristics of the frequency domain analysis decrease with increasing defect depth, however the spread in the material properties is so large that no decisive conclusion can be drawn on the defect depth after a measurement without detailed knowledge on the material properties of the object. Only a maximum defect depth can be retrieved when the defect is known to be a teflon coated glass insert of 25.4mm diameter and a thickness of 75 µm.

The lateral size of defects influences the thermography results as becomes clear from the experimental results in Figure 4.1 and 4.2 used for the simulation validation. More defects of different lateral sizes and at different depths have been evaluated using numerical simulations. The results of these simulations are shown in Figure 5.17. The lateral size of defects influences mainly the maximum phase difference. An increasing lateral size results in an increase of maximum absolute phase difference and a decrease in peak frequency, blind frequency and phase transition frequency as can be seen in Figure 5.18.

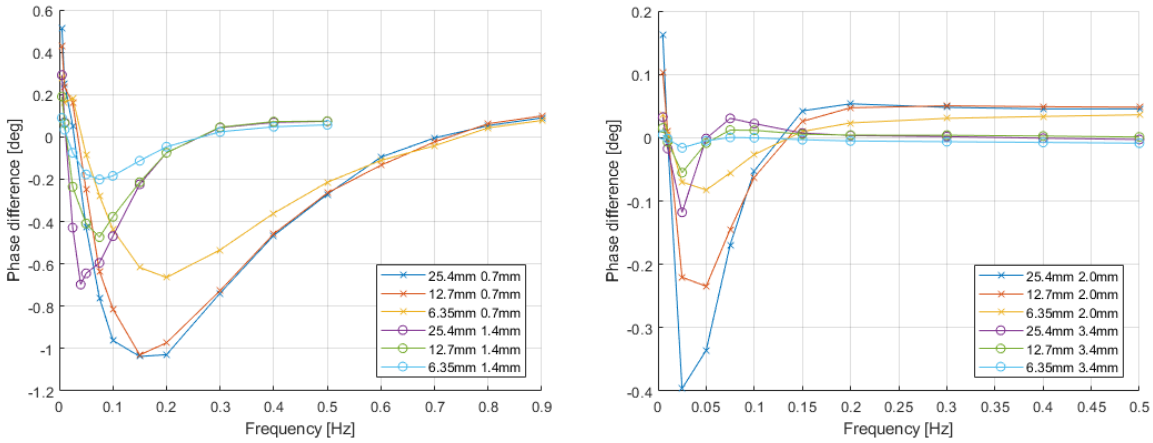

(a) *At 0.7 and 1.4 mm depth d.* (b) *At 2.0 and 3.4 mm depth d.*

Figure 5.17: *The phase difference as a function of the frequency for different defect sizes at different depths.*

The lateral size of defects can be determined to correct for the influence on the results. The lateral size of defects can be determined by manually selecting the boundaries. The boundaries are however not always very clear since the lateral heat conductivity k_l reduces the contrast at the defect edges. The effect of this can best be seen in Figure 5.1a where the phase difference of the middle and the edge of a defect are shown.

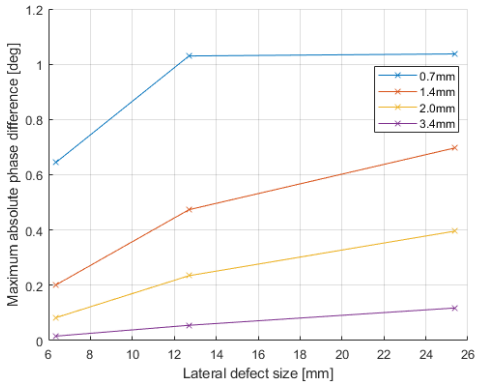

(a) *Maximum absolute phase difference*

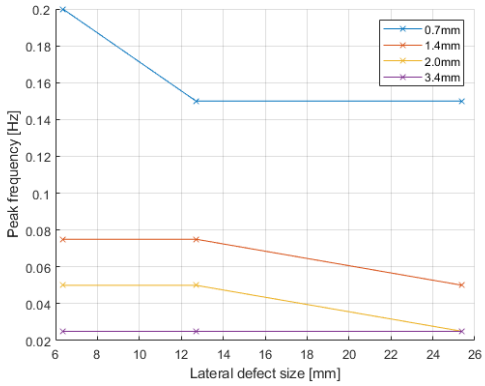

(b) *Peak phase frequency*

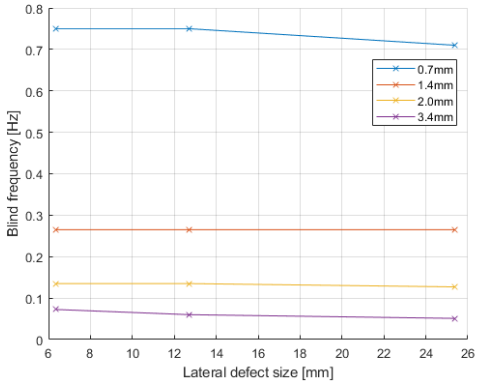

(c) *Blind frequency*

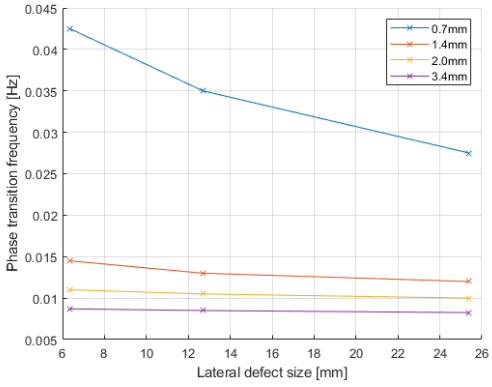

(d) *Phase transition frequency*

Figure 5.18: *The influence of the lateral size of a teflon coated glass insert on the characteristics.*

An alternative method for determining the lateral size of defects from thermography images is shifting the phase image several pixels and determining the gradient as is suggested by Choi et al. [40]. The results obtained by shifting the image 5 pixels horizontally and substracting it from the original image is shown in Figure 5.19a. The peaks in gradient in Figure 5.19b are located at the edges of the defects. An identical operation is performed vertically for the teflon coated glass inserts.

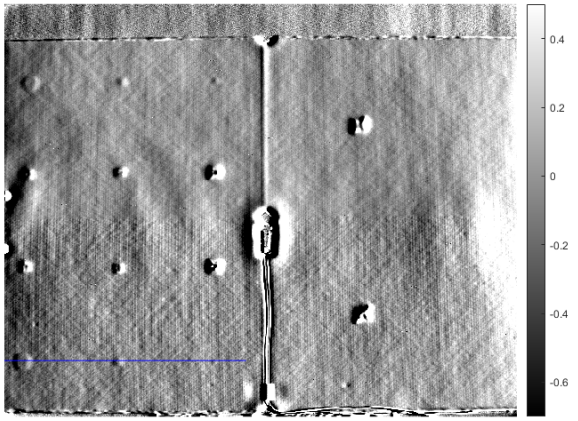

(a) *Resulting image of 5 pixel horizontal shift and substraction from the original.*

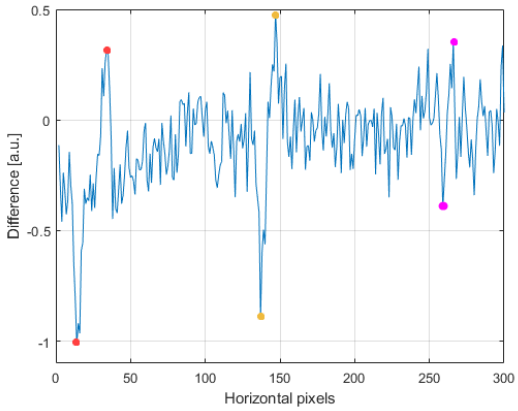

(b) *Profile of the blue line in Figure 5.19a (red = $T_{3,1}$, orange = $T_{2,1}$ and purple = $T_{1,1}$).*

Figure 5.19: *Horizontal image shift of phase image with a frequency of 0.005 Hz.*

The obtained size in pixels is shown in Table 5.6. To determine the actual size of the defects, the size of the pixels needs to be determined. Since the samples are flat, this can be done by assuming there is no lens distortion and the IR camera is arranged perpendicular to the object surface. During the measurement, the IR camera was placed at a distance of approximately 2,250 mm from the test surface. The field of view of the IR camera is 20.16 degree horizontally. At a distance of 2,250 mm, this results in a pixel size of approximately 1.341 mm. The resulting estimated size of the defects is shown in Table 5.6. It is clear that the lateral defect size of defects at 0.7 mm depth can be determined with an error smaller than the pixel size. More accurate measurements can be obtained by decreasing the effective pixel size by decreasing the distance between the camera and the test object. However, this narrows the effective field of view, significantly reducing the inspection speed of large surface areas.

Table 5.6: *Size of the defects in pixels and millimeters.*

Diameter [mm]	Hor. size	Vert. size	Average	Measured size [mm]	Error [mm]	Error [%]
25.4	19	20	19.5	26.15	0.75	2.95
12.7	9	9	9	12.07	0.63	4.96
6.35	4	5	4.5	6.04	0.31	4.88

The material of a defect that can be expected in a component depends on the life stage of the component. A defect emerged during the production process can consist of spurious material inclusions such as foils and tapes while this is impossible to happen during the in-service life of a CFRP component. These tapes can be for example the teflon coated glass inserts as used in the previous simulations and NTP samples. Another type of foil/tape used in the production environment of CFRP materials is kapton. Kapton has significantly different properties in comparison with Teflon coated glass as can be seen in Table 3.1. The thermal diffusivity α is 7.75e-8 m^2/s and the thermal effusivity e is 430.97 $J/m^2Ks^{1/2}$ in comparison with 1.18e-7 m^2/s and 756.31 $J/m^2Ks^{1/2}$ respectively for teflon coated glass. A delamination can occur both during production and in-service. This type of defect contains an air or gas pocket. The thermal properties of air vary significantly from foils or tapes such as kapton and teflon. The thermal diffusivity α of a thin air gap is 5.81e-5 m^2/s and the thermal effusivity e is 9.19 $J/m^2Ks^{1/2}$. Since the thermal properties of a thin air gap differ the most from the CFRP properties, this type of defect likely results in the best detectability. In order to detect a delamination, there has to be a gap between the two layers of the delamination. If the two layers are touching, the thermal conductivity differs far less from the CFRP and the detectability is drastically reduced.

Unfortunately no calibrated sample with real delaminations is available, therefore simulations are conducted. Identical parameters for the CFRP are used in simulations while the teflon insert is replaced by a kapton layer and an air layer respectively with a thickness of 0.075 mm. This thickness is equal to the thickness of the teflon coated glass used in the NTP samples and the previous simulations. The results of the simulations with kapton and air can be seen in Figure 5.20. It is important to note that the plots have different scales on the vertical axis.

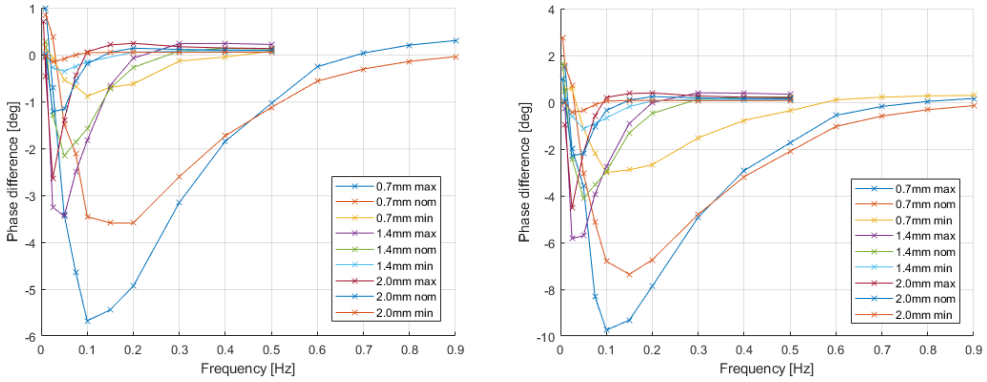

(a) *25.4 mm kapton tape of 0.075 mm thickness.*

(b) *25.4 mm delamination of 0.075 mm thickness filled with air.*

Figure 5.20: *The phase difference as a function of the frequency for different defect types and depths and the material properties from Table 5.4.*

It is clear that the defect material has a significant influence on the peak phase difference. However, this is not the only significant influence. The influence of the defect material, the CFRP material and the defect depth on the peak phase difference is shown in Figure 5.21. The influence of both materials is processed in the reflection coefficient R. The three different defect materials are marked with coloured squares. The R for an air layer inside the material is significantly larger than teflon and kapton since the emissivity value for this type of defect is very low. This figure also includes defects at different depths with the marked areas bounded by the results with the minimum and maximum detectability properties from Table 5.4 according to the colors in the legend. The data points with an equal defect depth are connected with linear interpolation to obtain the bounded areas for defects at 0.7, 1.4, 2.0 and 3.4 mm depth.

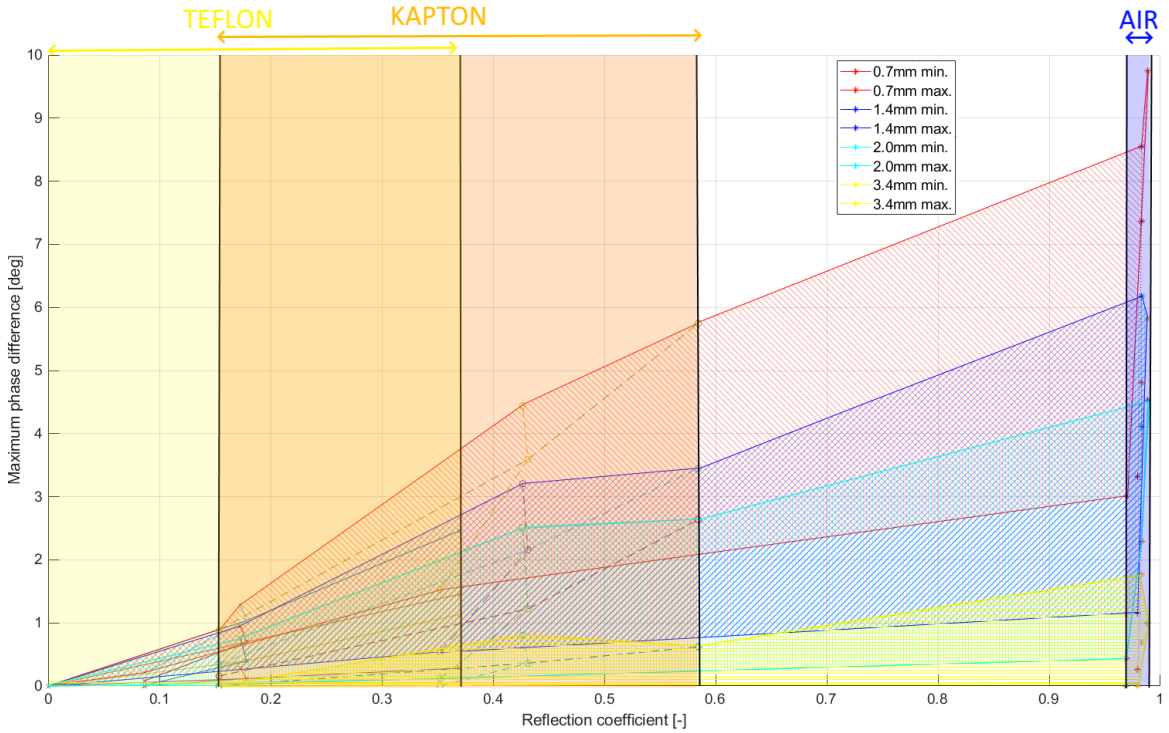

Figure 5.21: *The influence of the reflection coefficient R (and thus of the defect material and CFRP material) and the defect depth d on the peak phase difference. The three coloured squares indicate the results regions for different defect materials and the four highlighted areas indicate the result regions for different defect depths.*

The influence of the defect material on the frequency characteristics is not as large as influence on the peak phase difference, however it is still large enough to be significant to the thermography results. Since the peak frequency and the phase transition frequency have similar trend as the blind frequency and the blind frequency is more easily determined, the peak frequency and the phase transition frequency plots are omitted here. The blind frequency is plotted against the defect depth in Figure 5.22 for the three different materials. The theoretical blind frequency (see Equation 2.21) has also been added to this plot.

The combined effect of the defect depth, the defect material and the CFRP material properties in Figure 5.21 does not result in a decisive conclusion on the defect properties due to the wide spread of thermography results. This spread is a result of the spread in CFRP material properties. A depth range can however directly be obtained from the blind frequency using Figure 5.22. Higher blind frequencies result in a more confined depth window. For example, a blind frequency of 1 Hz results in a defect depth between 0.28 mm and 1.24 mm. With this knowledge, only the red and blue marked sections (for 0.7 and 1.4 mm depth respectively) are of interest in Figure 5.21. A phase difference value of for example 4 degrees, limits the reflection coefficient to approximately 0.39 or larger. Combining this knowledge leads to a defect that is located between 0.28 and 1.24 mm deep and has material properties similar to either kapton or air.

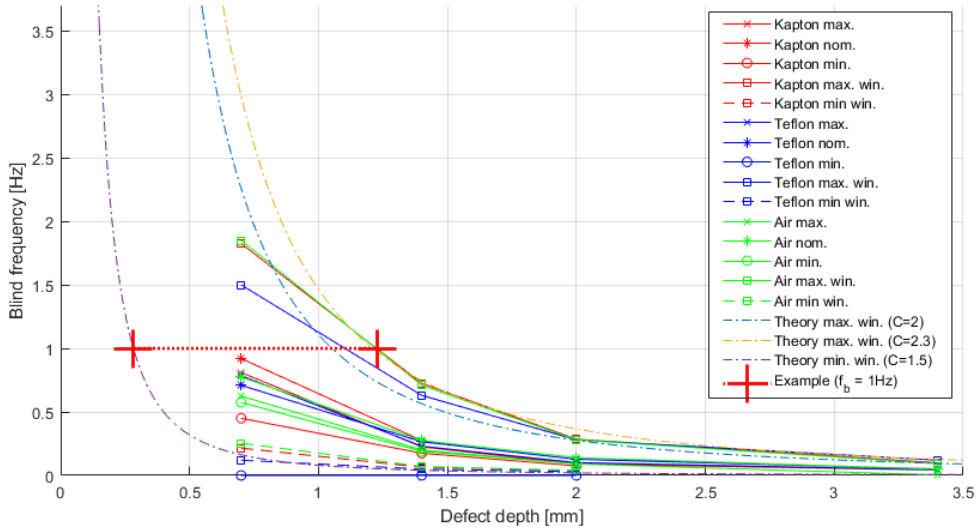

Figure 5.22: *The blind frequency f_b as a function of depth for the 5 scenarios from Table 5.4 and 5.5 for three different 25.4 mm defect materials (teflon, kapton and air) of 0.075 mm thickness. Combined with the theoretical (empirically determined) minimum and maximum.*

A more confined conclusion can be drawn by combining the peak phase difference and the blind frequency results, this combination is shown in Figure 5.23. The coloured areas in this plot are obtained by connecting the minimum and maximum detectability and the minimum and maximum window simulation results for each defect material. The previously used example of a defect with a phase difference of 4 deg and a blind frequency op 1 Hz is highlighted in this figure. This defect would be a kapton tape. Combined with the depth location knowledge from Figure 5.22, the approximate depth (between 0.28 and 1.24 mm) and the defect material (kapton) can be determined. The higher the phase difference and the blind frequency, the more decisive a conclusion on the defect properties can be since the regions of the different defect materials overlap for lower blind frequencies and peak phase differences.

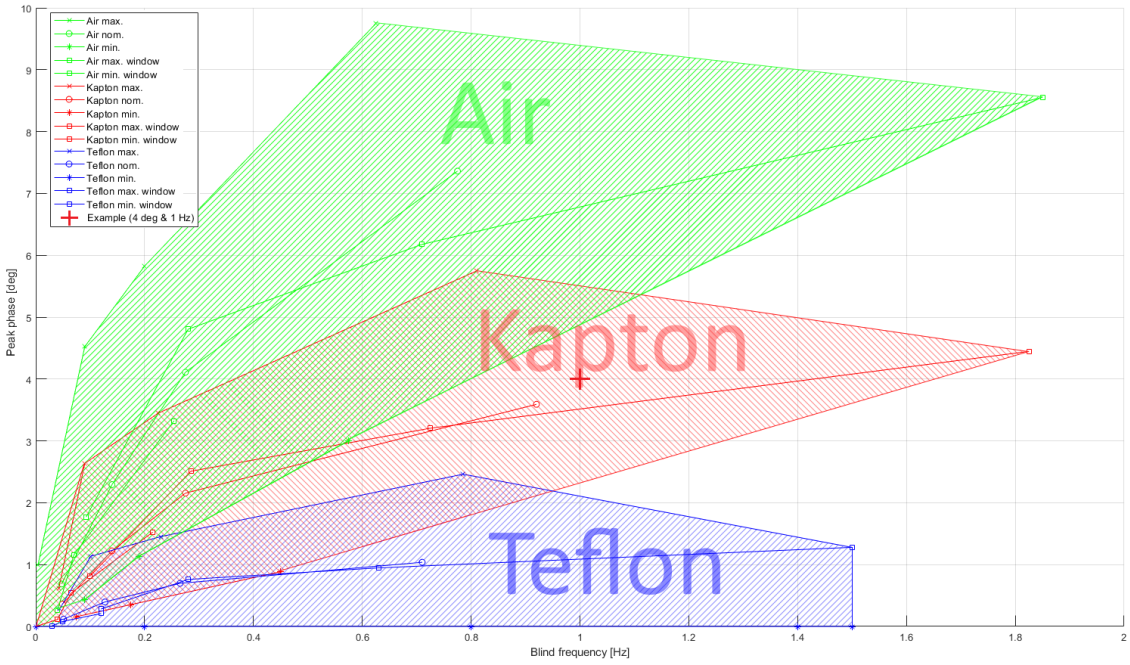

Figure 5.23: *The peak phase difference as a function of the blind frequency f_b for the 5 scenarios from Table 5.4 and 5.5 for three different 25.4 mm defect materials (teflon, kapton and air) of 0.075 mm thickness at different depths (0.7 - 3.4 mm).*

The data in Figure 5.21, 5.22 and 5.23 are based on simulations with a defect thickness of 75 µm and a lateral size of 25.4 mm and a PU coating of 30 µm thick. It is known that the lateral size and the coating have an influence on the thermography results. However both the lateral size and the coating thickness can be determined and the influence of these factors can thus be corrected with respect to the results in Figure 5.23.

To determine the influence of thicker and thinner defects, simulations have been performed with a thickness of 37.5 µm and 150 µm. This is half and double the defect thickness used in the previous simulations. The results of the thinner, normal (75 µm) and thicker defect is shown in Figure 5.24 for a teflon coated glass insert and a delamination filled with air. It is important to note that the plots have different scales on the vertical axis.

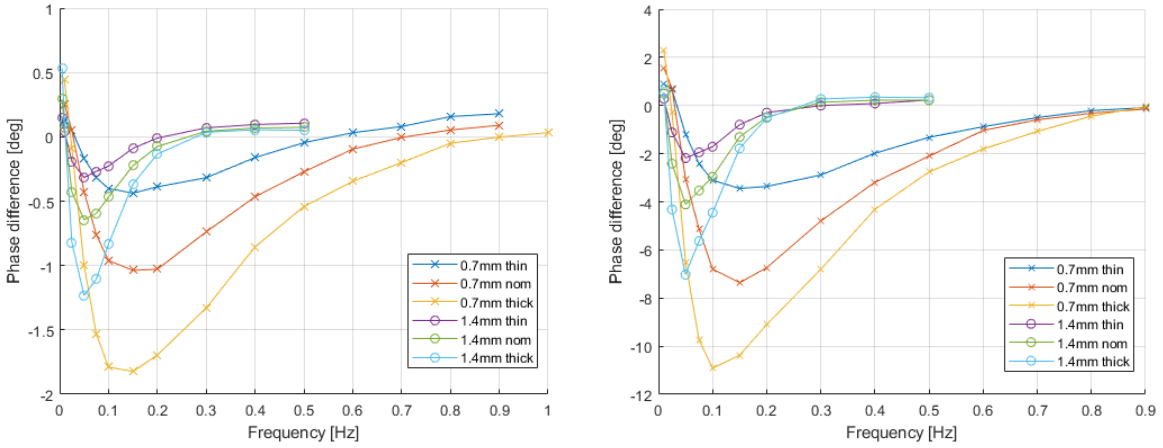

(a) *Teflon coated glass (25.4 mm diameter).* (b) *Delamination filled with air (25.4 mm diameter).*

Figure 5.24: *Lock-in thermography simulation results with different defect thickness (thin = 37.5 µm, nom = 75 µm and thick = 150 µm).*

It can be concluded that the effect of the defect thickness is very important. In a production environment, only certain types of foils and tapes are used. The thickness of these foils is always known. If for example teflon foil with a thickness of 50 µm and kapton foil with a thickness of 25 µm are used in a production environment, calibration panels and measurements can be made. This is however an expensive process. With prior knowledge of the materials that can potentially be included in a laminate, an alternative method is to perform simulations and create a production environment specific version of the peak phase difference versus blind frequency plot (Figure 5.23). In a production environment, measurements of the thermal diffusivity might also be possible since the sample is accessible from both sides which is most often not possible in a MRO environment. Using through transmission measurement, the thermal diffusivity can be determined [81]. With the combination of knowledge on the thermal conductance of the CFRP material and the thermography results, the plot in Figure 5.23 can be created with much narrower regions for each type of defect resulting in more decisive defect characterisation.

In MRO one is not interested in finding tapes or foils inside the laminate as these foreign material inclusions originate during manufacturing and are detected in the production inspection. The thickness of an air filled delamination influences the thermography results significantly. The blind frequency is however only marginally influenced for an air filled delamination. For application in a MRO environment, the blind frequency versus peak phase difference plot (Figure 5.23) can be made for different delamination (air gap) thicknesses.

5.6 Summary

In this chapter four characteristics are identified in the phase difference data obtained with frequency domain analysis thermography; peak phase difference, peak phase frequency, blind frequency and the phase transition frequency. The value of these characteristics is based on the difference between the phase of a defect and a non defect region. The experiments on the NTP samples showed the limited capability of frequency domain analysis thermography to detect deeper located defects. This is confirmed in the numerical simulations to be a result of the limited difference in thermal properties of the defect (teflon coated glass) and the CFRP. The influence of all factors and their parameters from Figure 3.1 on the four characteristics is determined by varying the parameters OFAT using numerical simulations.

The factors can be split in two categories, the first consists of the factors that can be influenced by the operator; the lamps and the camera. Although these factors are found to limit the detectability of deeper defects and defects with similar thermal properties to the CFRP material such as teflon coated glass, these factors do no influence the magnitude of the characteristics.

The second category consists of the factors that can not be influenced by the operator; the surface, the material and the defect. These factors have a significant influence on the four characteristics. The surface influences the SNR of the experiments as it influences the heat deposition. The coating thickness does influence the characteristics. The coating thickness can however be determined and corrected for. The CFRP material thermal properties can vary largely depending on the manufacturing process and the constituents. The largest spread in the results is caused by the spread in CFRP material properties, therefore more knowledge on the CFRP material properties of the sample results in an increased ability to perform defect characterisation.

Three defect materials have been simulated; teflon coated glass, kapton tape and an air filled delamination. In combination with the outer values of the CFRP material parameters, a window of possible thermography results for a selection of defects is obtained. This results in the ability to make a partly decisive conclusion on the defect type based on the peak phase difference and the blind frequency without detailed knowledge on the properties of the test object material. The defect thickness however plays an important role on this ability. In a production environment the thickness of all tapes and foils are known, making defect characterisation with frequency domain analysis possible. In MRO, the thickness of a defect (delamination) can vary. However with varying air gap thickness, the blind frequency only changes marginally. This makes the combination of the blind frequency and the peak value suitable for determining a range of defect depth and defect thickness in a MRO environment.

5.7 Conclusion

The decisiveness of the frequency domain analysis thermography results on the defect properties is promising. In a production environment the thickness and thermal properties of all tapes and foils that can potentially be included in the composite are known. With this knowledge, the material of the defect can be determined from the blind frequency and the peak phase difference. The approximate depth can be determined with the blind frequency characteristic, resulting in a depth range. This range can be narrowed if the CFRP material properties are known. The lateral size of a defect can be evaluated from the phase image. This results in a decisive characterisation of most defects with the results from frequency domain analysis thermography measurements in a production environment. Deeper located defects or defects with material properties similar to the CFRP may result in indecisive conclusions on the defect properties.

In a MRO environment the thickness of a defect (air filled delamination) can vary. With varying air gap thickness, the blind frequency only changes marginally. This makes it possible to determine a defect depth range from this characteristic. The lateral size of air filled defects can be evaluated from the phase image, similar to a production environment. This makes frequency domain analysis thermography suited for defect characterisation in a MRO environment. In both environments (production and MRO), the main source of the indecisiveness on defect characters is the spread in the CFRP material properties. Therefore more knowledge on these properties would result in a more decisive characterisation.

Chapter 6: Pulse compression analysis

In this chapter the pulse compression analysis thermography results are presented. The theory on pulse compression analysis thermography can be found in subsection 2.3.3. Firstly, an example of pulse compression using CC with a linear chirp signal is shown to introduce the characteristic results of a pulse compression analysis. Next to a linear chirp signal, other signals can be used for pulse compression as is discussed in subsection 2.3.3. The results of the different signals are discussed secondly after which an analysis of the sensitivity to the factors and their parameters discussed in chapter 3 and the discovered correlations between defect characteristics and the thermography results are presented. Section 6.8 concludes on the characterisation capabilities of pulse compression analysis thermography.

The CC of a linear chirp signal can be seen in Figure 6.1. Two main characteristics can be obtained from the cross correlation signal. The first is the peak correlation value of the main peak and second is the delay time τ at which the main peak occurs. The difference in peak value and delay time between a defect and a non defect region are the characteristic values for a defect. The peak value requires normalisation as discussed in section 3.4. An example of this normalisation can be seen in Figure 6.1b.

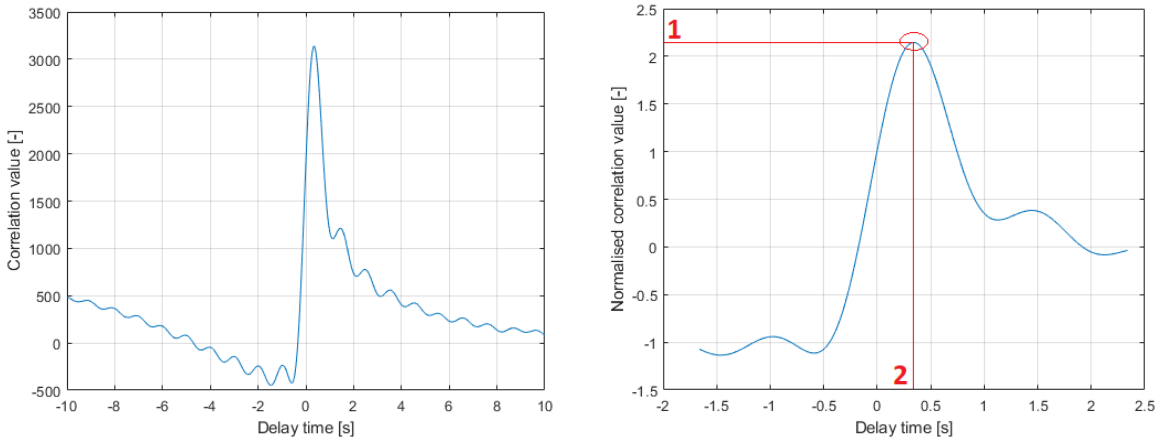

(a) *Not normalised* (b) *Normalised*

Figure 6.1: *Cross correlation of the reference signal and the temperature profile of a pixel in an undamaged region of the NTP-A2 panel subjected to heat with a chirp signal of 1-0.01Hz (in 250s).*

The third characteristic that can be obtained from CC is the CC phase as discussed in section 3.4. In the remainder of this chapter, the difference in normalised peak value, peak delay time and CC phase between defect and non defect regions will be referred to as just the peak value, the peak delay time and the CC phase to improve readability. The three characteristics are listed below:

- **Peak value**, the peak value of the normalised correlation function (1 in Figure 6.1b).
- **Peak delay time**, the delay time at which the peak correlation value is obtained (2 in Figure 6.1b).
- **CC phase**, the CC divided by the CC with the quadrature of the reference signal.

Experiments are used to determine the influence of the different signals firstly while numerical simulations are performed to determine the sensitivity of the three cross correlation characteristics to the influencing factors and their parameters in Figure 3.1.

6.1 Effect of the heat signal

The results are dependent on the signal that is used for the heat deposition. Different signals can be used for pulse compression as is discussed in subsection 2.3.3. Experiments have been performed with a linear chirp signal, quadratic chirp signal and a barker code signal. The experiments are limited by the sampling frequency of the camera at 100 Hz resulting in a sampling time of 0.01 s. Resampling has been performed on the experiment data to obtain a sufficiently small time resolution.

In a linear chirp signal, the signal length, the starting- and the end frequency can be changed. Experiments are performed with different signal lengths and frequency ranges. The resulting values can be found in Table 6.1. In a quadratic chirp signal, the same parameters can be changed. Experiments are performed with different signal lengths and frequency ranges. The resulting values can be found in Table 6.2. The SNR obtained with both the linear chirp and the quadratic chirp signal for the CC phase and peak value are much larger than the SNR obtained for the phase difference with LT (see Table 5.1).

Table 6.1: *Results for the $T_{3,1}$ defect (25.4 mm at 0.7 mm depth) of the NTP-A2 panel with linear chirp signals.*

$\mathbf{f_0}$ [Hz]	$\mathbf{f_1}$ [Hz]	**T** [s]	**B** [-]	$\mathbf{CC}_{norm}$ [-]	$\mathbf{CC}_{norm}$ **SNR** [-]	τ [-]	τ **SNR** [-]	$\mathbf{CC}_{\varphi}$ [-]	$\mathbf{CC}_{\varphi}$ **SNR** [-]
0.2	0.1	100	0.1	-0.0004	1.57	0.0025	1.31	-0.7373	2.66
		150	0.1	-0.0005	1.99	0.0028	1.19	-0.8700	3.42
0.5	0.05	150	0.45	-0.0105	4.63	0.0060	1.02	-0.9725	3.32
		200	0.45	-0.0106	5.20	0.0061	1.15	-1.0357	3.78
		250	0.45	-0.0105	4.81	0.0060	1.95	-1.0652	3.38
1	0.01	250	0.99	-0.0232	3.98	0.0015	1.02	-0.5802	3.17

Table 6.2: *Results for the $T_{3,1}$ defect (25.4 mm at 0.7 mm depth) of the NTP-A2 panel with quadratic chirp signals.*

$\mathbf{f_0}$ [Hz]	$\mathbf{f_1}$ [Hz]	**T** [s]	**B** [-]	$\mathbf{CC}_{norm}$ [-]	$\mathbf{CC}_{norm}$ **SNR** [-]	τ [-]	τ **SNR** [-]	$\mathbf{CC}_{\varphi}$ [-]	$\mathbf{CC}_{\varphi}$ **SNR** [-]
0.2	0.1	100	0.1	-0.0023	3.23	0.0206	3.63	-1.5068	3.68
		150	0.1	-0.0019	3.63	0.0223	4.09	-1.6282	4.11
0.5	0.05	150	0.45	-0.0027	2.89	0.0051	1.52	-0.6246	1.59
		200	0.45	-0.0022	2.48	0.0054	1.65	-0.7681	2.11
		250	0.45	-0.0022	2.53	0.0052	1.64	-0.8989	2.31
1	0.01	250	0.99	-0.0080	2.74	0.0004	0.16	-0.2308	0.83

The last two signals applied in thermography in combination with pulse compression analysis are the digital chirp signal and the barker signal. The halogen lamps in the experimental set-up however proved to be not very suitable for these type of binary signals. Since the pulses with a barker coded signal are relatively long, this works better with halogen lamps than the digital chirp signal. Experiments have been performed with a 7-bit Barker code signal length of 100, 150, 200 s. The resulting values can be found in Table 6.3.

Table 6.3: *Results for the $T_{3,1}$ defect (25.4 mm at 0.7 mm depth) of the NTP-A2 panel with 7-bit Barker code signals.*

T [s]	$\mathbf{CC}_{norm}$ [-]	$\mathbf{CC}_{norm}$ **SNR** [-]	τ [-]	τ **SNR** [-]	$\mathbf{CC}_{\varphi}$ [-]	$\mathbf{CC}_{\varphi}$ **SNR** [-]
100	0.0052	0.94	-0.0772	0.18	0.424	1.26
150	0.0050	1.10	-0.1166	0.86	0.524	1.93
200	0.0019	1.12	-0.2496	0.42	0.837	1.23

From Table 6.1, 6.2 and 6.3 it can be concluded that a linear chirp signal results in the highest SNR on the NTP samples. From the linear chirp signals tested, the signal with a frequency range from 1 to 0.01 Hz has been selected for the sensitivity analysis of the other parameters from Figure 3.1 since this frequency range is wide enough to cover the frequencies required on the samples in the frequency domain analysis as is discussed in chapter 5.

The peak value without normalisation and the three CC characteristics images from experimental results on the NTP-A2 panel with a linear chirp signal of 250 s from 1 to 0.01 Hz are shown in Figure 6.2. The experimental results of the linear chirp signal of 250 s from 0.5 to 0.05 Hz, the quadratic chirp signal of 250 s from 0.5 to 0.05 Hz, the quadratic chirp signal of 250 s from 1 to 0.01 Hz and the Barker code signal with a length of 150 s can be found in appendix D.

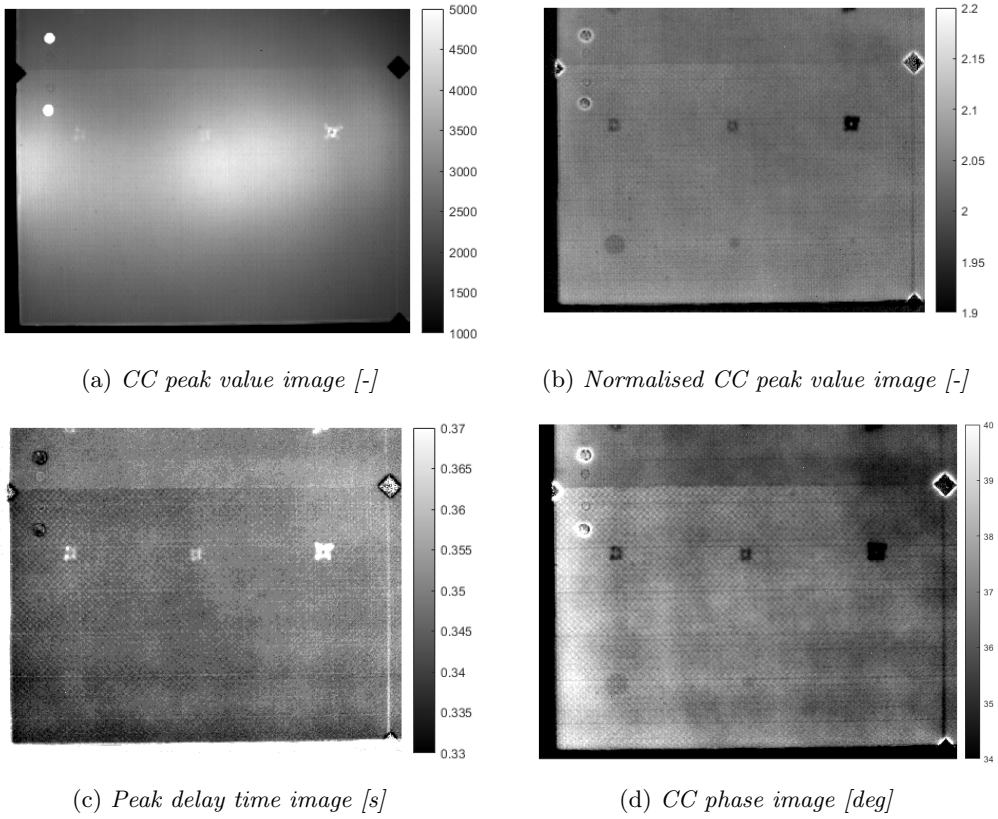

(a) *CC peak value image [-]*

(b) *Normalised CC peak value image [-]*

(c) *Peak delay time image [s]*

(d) *CC phase image [deg]*

Figure 6.2: *Experimental results of the linear chirp signal (1 - 0.01 Hz in 250 s) on the NTP-A2 sample.*

The experimental results of the linear chirp (from 1 to 0.01 Hz in 250 s) are compared with the simulation of the 25.4 mm teflon coated glass insert at 0.7 mm depth. The results of the simulation and the experiment are very similar as can be seen in Table 6.4.

Table 6.4: *Comparison of experiment and simulation of the 25.4 mm Teflon coated glass insert at 0.7 mm in the NTP-A2 sample.*

	Peak value [-]	**Peak delay time** [s]	**CC phase** [deg]
Experiment	-0.0232	0.0015	-0.5802
Simulation	-0.0228	0.0014	-0.5742

6.2 Effect of the lamp parameters

In the simulations, the difference in heat flux resulting from different lamp parameters does not influence the results. The non-normalized peak value increases with increasing heat deposition as the magnitude of the AC component of the perceived signal increases resulting in a higher correlation value. The normalized peak value, the peak delay time and the correlation phase differences are not influenced by the heat flux. The SNR however does increase with increasing lamp power as can be seen in Table 6.5. It can be concluded that a higher heat flux results in a higher SNR but does not influence the relevant thermography results.

Table 6.5: *Results for the $T_{3,1}$ defect (25.4 mm at 0.7 mm depth) of the NTP-A2 panel with a chirp signal from 0.5 - 0.05 Hz in 150 s for varying lamp powers.*

Lamps power [%]	**CC**$_{norm}$ [-]	**CC**$_{norm}$ **SNR** [-]	τ [-]	τ **SNR** [-]	**CC**$_{\varphi}$ [-]	**CC**$_{\varphi}$ **SNR** [-]
50	-0.0101	3.22	0.0066	0.97	-0.9580	2.03
75	-0.0105	4.63	0.0060	1.02	-0.9725	3.32
100	-0.0105	4.76	0.0066	1.35	-0.9453	3.37

6.3 Effect of the camera parameters

In the experiments, only the teflon coated glass inserts at 0.7 mm depth are detectable. Since the camera is not calibrated for the temperature range used in thermography, no absolute temperature measurements can be performed. However the thermal resolution of the camera is < 20 mK. The temperature difference between defect and non defect regions is determined for the teflon coated glass inserts using numerical simulations. The results of these simulations can be found in Table 6.6. With a maximum temperature difference of 20.6 mK, the temperature signal of the area above a teflon coated glass insert at 1.4 mm is barely to non distinguishable from the temperature signal of a non defect region.

Table 6.6: *The mean and maximum temperature difference for a 25.4 mm teflon coated glass insert with a chirp signal from 0.5 - 0.05 Hz in 150 s.*

Diameter [mm]	**Depth** [mm]	**dT mean** [mK]	**dT max.** [mK]
25.4	*0.7*	26.5	38.3
25.4	*1.4*	16.1	20.6
25.4	*2.0*	9.6	11.7

6.4 Effect of the surface parameters

Two different coating thicknesses are considered. The first coating thickness is 30 µm PU coating which is the thickness of the coating on the NTP-A1 and NTP-A2 panels and is representative for military composite applications. The second coating thickness is 115 µm which is representative for civil aircrafts [79]. The coating layers have been simulated for a 25.4 mm teflon coated glass insert at 0.7 and 1.4 mm deep. The results of these simulations can be found in Table 6.7. It is clear that increasing coating thickness results in a decrease of the three characteristics. The coating thickness can however be measured and corrected for. The surface roughness and colour also influence the heat absorbed and emitted by the object through radiation, this influences heat flux of which the influence on the characteristics is covered in section 6.2.

Table 6.7: *The CC characteristics with different coating thickness for a 25.4 mm teflon coated glass insert.*

Diameter [mm]	**Depth** [mm]	**Coating thickness** [µm]	**Norm. peak** [-]	**Time delay** [s]	**CC phase** [deg]
25.4	*0.7*	*30*	-0.0228	0.0014	-0.5742
25.4	*0.7*	*115*	-0.0165	0.0010	-0.5038
25.4	*1.4*	*30*	-0.0034	0.0000	-0.1715
25.4	*1.4*	*115*	-0.0020	0.0000	-0.1508

6.5 Effect of the material parameters

The influence of the four material parameters; k_l, k_t, c_p and ρ is determined using the OFAT approach. The trends are used to determine the combinations of material parameters resulting in boundaries of the thermography results. This approach is similar to the approach taken for determining the material influence on the frequency domain analysis thermography results in chapter 5. The plots that show the trends in the influence of the material parameters on the pulse compression thermography results can be found in appendix E.

The lateral thermal conductivity k_l is considered separately from the through thickness conductivity k_t, the mass density ρ and the thermal capacity c_p of the CFRP material since the influence of k_l on the thermography results is relatively small. The peak delay time τ is not influenced beyond the sampling frequency. It can be concluded that the influence of k_l on the thermography results is relatively small (see Figure E.1 in appendix E).

The out-of-plane thermal conductivity k_t, the thermal capacity c_p and the mass density ρ can be combined in the thermal diffusivity α_t and the reflection coefficient R. The plots of the three characteristics against the thermal diffusivity α_t and the reflection coefficient R can be found in appendix E. From these plots a set of parameters that result in minimum and maximum results can be obtained. The peak value and the CC phase both increase with increasing reflection coefficient R while the peak time delay increases with increasing thermal diffusivity α_t. The maximum reflection coefficient R is achieved with a maximum k_t, ρ and c_p. The maximum thermal diffusivity α_t is achieved with a maximum k_t and a minimum ρ and c_p . Although the influence of the lateral thermal conductivity is small, it is taken into account in the boundary material parameters. This results in the combinations of material parameters shown in Table 6.8 and 6.9. These parameters are equal to the boundary material parameters obtained for the frequency domain analysis in chapter 5 with the exception of the k_l for the minimum and maximum delay time. Since the influence of k_l is negligible on the delay time, this parameter is set equal to the fitted parameters at 7 W/mK. These parameters are used in numerical simulations to obtain the boundaries of the pulse compression analysis thermography results for a teflon coated glass insert of 25.4 mm.

Table 6.8: *The parameters resulting in minimum and maximum peak value and CC phase for a teflon coated glass insert.*

Parameter	k_t	k_l	ρ	c_p
Unit	[W/mK]	[W/mK]	[J/kgK]	[kg/m^3]
Minimum detectability	0.3	12	1,150	1,000
Fitted parameters (NTP-A1 and NTP-A2 panels)	0.7	7	1,528	1,100
Maximum detectability	1	2	2,250	1,200

Table 6.9: *The parameters resulting in the smallest and largest peak delay time for a teflon coated glass insert.*

Parameter	k_t	k_l	ρ	c_p
Unit	[W/mK]	[W/mK]	[J/kgK]	[kg/m^3]
Small delay	0.3	7	2,250	1,200
Fitted parameters (NTP-A1 and NTP-A2 panels)	0.7	7	1,528	1,100
Large delay	1	7	1,150	1,000

The simulations with the material properties in Table 6.8 and 6.9 result in the minimum and maximum values of the CC characteristics for a 25.4mm teflon coated glass insert of 75 µm thickness. The three characteristics are plotted as a function of the defect depth in Figure 6.3. Although the minimum material properties result in very small positive values for the peak value and the CC phase, in this figure these values are set to zero since these results have a very small temperature difference ($<$ 5 mK) between the defect and a non defect region. In reality this would result in undetectable defects.

The range of the characteristics resulting from the range in CFRP material properties is quite large. If it is known that there is a teflon coated glass insert of 75 µm and 25.4 mm diameter inside the material, the data in Figure 6.3 can only be used to obtain a depth range of the defect. To determine the possibility of differentiating different types of defects with the thermography results, the influence of different types of defects is determined in section 6.6.

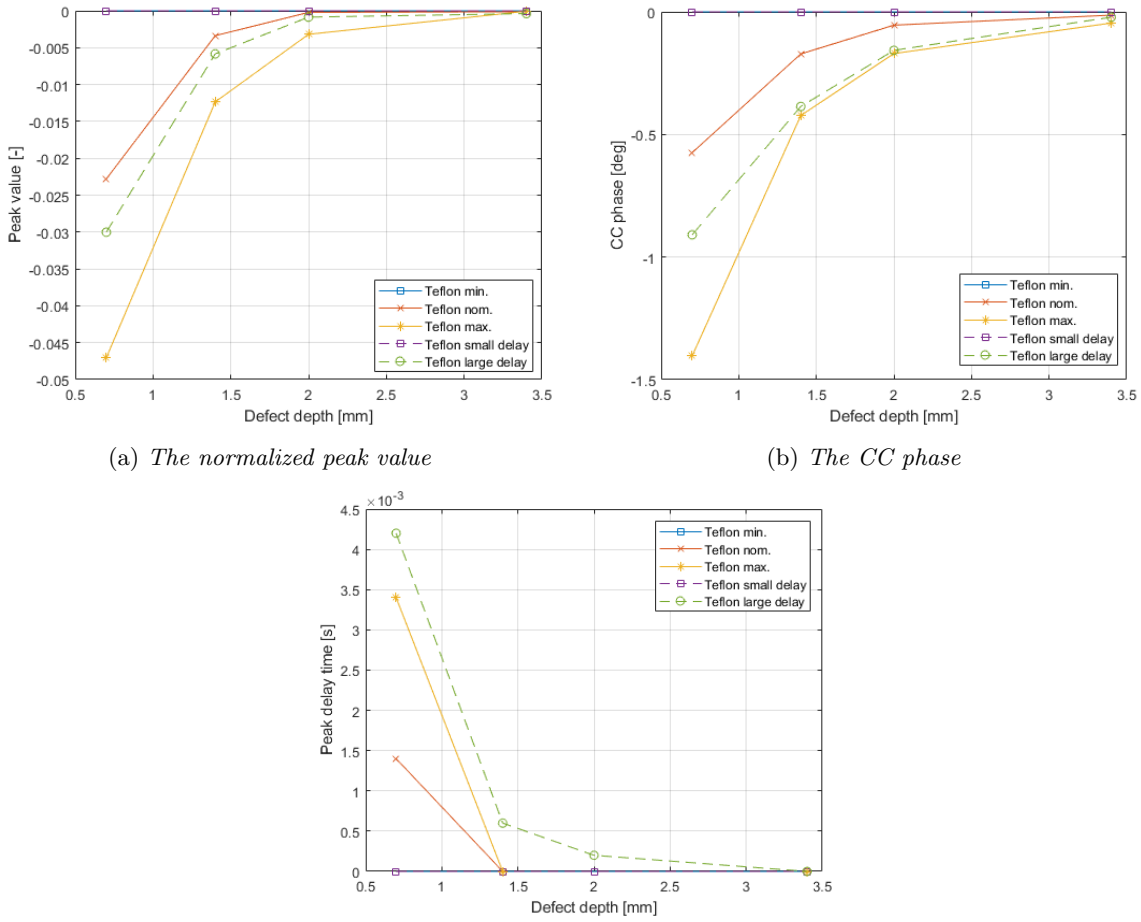

(a) *The normalized peak value*

(b) *The CC phase*

(c) *The peak delay time*

Figure 6.3: *The CC characteristics as a function of the defect depth for a 25.4 mm teflon coated glass insert with the CFRP material properties from Table 6.8 and 6.9.*

6.6 Effect of the defect parameters

The previous part of this chapter showed the influence of all the parameters not related to the defect on the thermography results. A window of thermography results has been determined for a 25.4 mm teflon coated glass insert at different depths. Besides all the influences treated in this chapter, the defect in a CFRP panel has four parameters that influence the thermography results. The depth with respect to the front surface, the lateral size, the material of the defect and the thickness of the defect. The influence of the depth and the lateral size is shown firstly. After that the influence of the defect material is shown by simulation of two other types of defects. The first defect is a kapton tape insert representing a tape accidentally left behind between plies in the production. The second is a thin air gap to simulate a gas pocket formed during production or a delamination originated during in-service life. Lastly the thickness of the defect is varied to determine the influence of this parameter on the thermography results.

The defect depth has a decreasing influence on all three characteristics as can be seen in Figure 6.3 and 6.4. This is due to the highly dissipative behaviour of the heat flow. This makes it possible to determine a maximum depth of a defect with the thermography values obtained with a measurement.

The lateral size of a defect is of importance since the lateral heat flow reduces the difference between a defect and a non defect region. Simulations have been performed for 25.4, 12.7 and 6.35 mm diameter defects. The results of these simulations can be found in Table 6.10. A laterally larger defect decreases the impact of the lateral heat flow on the contrast of the defect area with respect to the non defect areas around it, resulting in larger differences as can be seen in the table. The lateral size of a defect can be evaluated from the thermography result image. This can be done from either the peak value image, the peak delay time image or the CC phase image. The experimental results however show that the peak value image has the highest SNR and thus the best identifiable defects (see Figure 6.2 and Table 6.1 and 6.5).

Table 6.10: *The influence of the lateral size on the CC characteristics for a glass coated teflon insert (k_l = 7 W/mK, k_t = 0.7 W/mK, ρ = 1,528 kg/m^3 and c_p = 1,100 J/kgK).*

Diameter [mm]	**Depth** [mm]	**CC**$_{norm}$ [-]	τ [s]	**CC**$_{\varphi}$ [deg]
25.4	*0.7*	-0.0228	0.0014	-0.5742
12.7	*0.7*	-0.0216	0.0014	-0.5140
6.35	*0.7*	-0.0144	0.0012	-0.3195
25.4	*1.4*	-0.0034	0.0000	-0.1715
12.7	*1.4*	-0.0026	0.0000	-0.1145
6.35	*1.4*	-0.0013	0.0000	-0.0379

The defect material can have a significant impact on the thermography results since the defect detection is based on a difference in thermal properties between the defect and the CFRP. For example a teflon coated glass insert has very similar properties to the CFRP while a thin air gap has significantly different properties. To determine the influence of different defect materials, three different materials are simulated; teflon coated glass, kapton and air. The thickness of the defects has been set at 75 µm and is varied later in this section. By performing the simulations with the boundary CFRP material parameters from Table 6.8 and 6.9, the outer limits of the thermography results for the 3 types of defects can be determined. The results from these simulations can be found in Figure 6.4. Each of the three CC characteristics has been plotted as a function of the defect depth. A clear distinction can be made in the magnitude of the thermography results for the three different materials. However there is a significant overlap between the results for the different defect materials, making it hard to get a decisive conclusion on the defect properties from the thermography results.

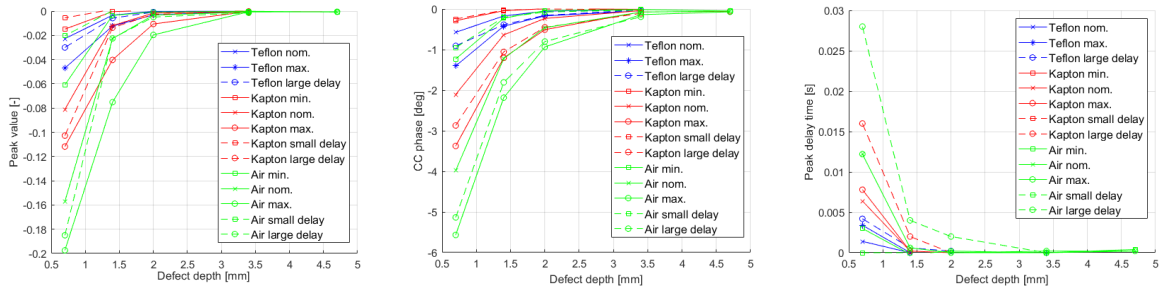

(a) *Peak value* (b) *CC phase* (c) *Peak delay time*

Figure 6.4: *The simulation results showing the CC characteristics for the three different defect materials (with a thickness of 75 µm and a diameter of 25.4 mm) and the CFRP material properties from Table 6.8 and 6.9 as a function of the defect depth.*

The overlap and the difference between the results obtained with the different defect materials can more clearly be seen in Figure 6.5. In this figure the areas bounded by the minimum and maximum values are highlighted. For each of the three highlighted regions, the defects with lower values (thus in the upper right of Figure 6.5) correspond to deeper located defects. This is the main trend that can be observed from Figure 6.4.

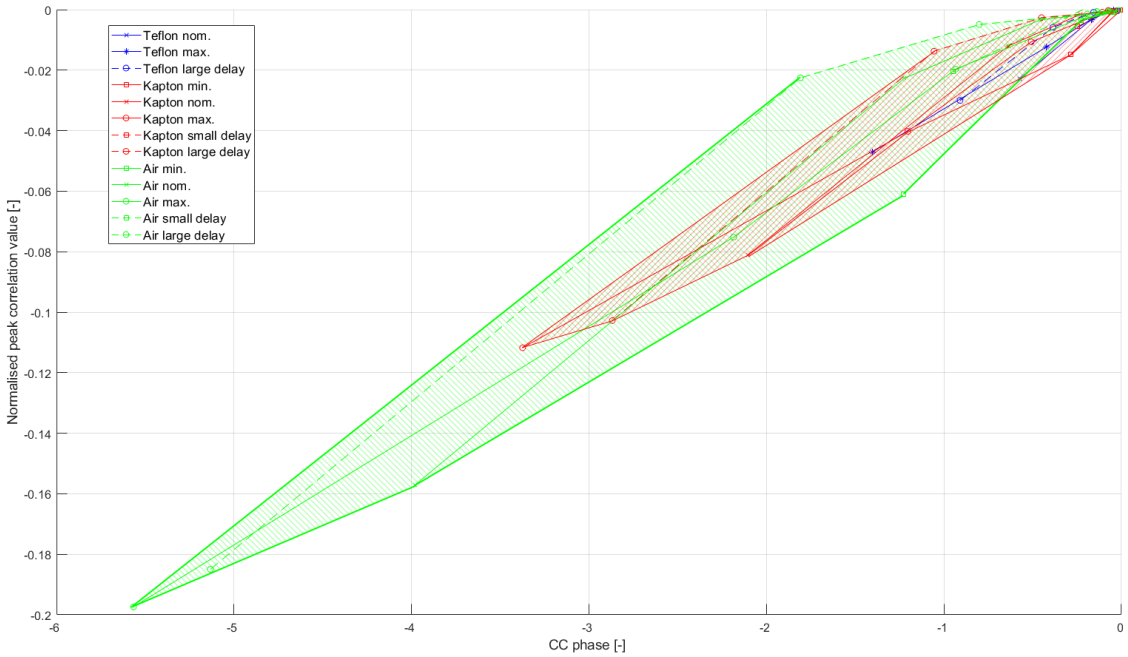

Figure 6.5: *The normalised peak correlation value as a function of the CC phase with the regions for 25.4 mm teflon coated glass, kapton and air inclusions with a thickness of 75 µm and the CFRP material properties from Table 6.8 and 6.9.*

The information in all previous figures of this chapter is based on a defect thickness of 75 µm. In a production environment the thickness of all foils and tapes that are used is known, making it possible to determine areas in Figure 6.5 specific for each type of foil. In a MRO environment, the thickness of defects is not known since a delamination can have different thickness. The influence of the defect thickness is determined by performing simulations with defects of 37.5 and 150 µm thick with a teflon coated glass insert and a air filled delamination. The results of these simulations can be found in Table 6.11 and Table 6.12 for teflon coated glass and air respectively.

Table 6.11: *The influence of the defect thickness on the CC characteristics for a glass coated teflon insert (simulation with CFRP properties: k_l = 7 W/mK, k_t = 0.7 W/mK, c_p = 1,100 J/kgK and ρ = 1,528 kg/m^3).*

Diameter [mm]	**Depth** [mm]	**Defect thickness** [µm]	**CC**$_{norm}$ [-]	τ [s]	**CC**$_{\varphi}$ [deg]
25.4	*0.7*	37.5	-0.0108	0.0004	-0.2214
25.4	*0.7*	75	-0.0228	0.0014	-0.5742
25.4	*0.7*	150	-0.0429	0.0032	-1.1868
25.4	*1.4*	37.5	-0.0009	0.0000	-0.0289
25.4	*1.4*	75	-0.0034	0.0000	-0.1715
25.4	*1.4*	150	-0.0066	0.0000	-0.3758

Table 6.12: *The influence of the defect thickness on the CC characteristics for an air filled defect (simulation with CFRP properties: k_l = 7 W/mK, k_t = 0.7 W/mK, c_p = 1,100 J/kgK and ρ = 1,528 kg/m^3).*

Diameter [mm]	**Depth** [mm]	**Defect thickness** [µm]	**CC**$_{norm}$ [-]	τ [s]	**CC**$_{\varphi}$ [deg]
25.4	*0.7*	37.5	-0.0865	0.0060	-2.1867
25.4	*0.7*	75	-0.1571	0.0122	-3.9804
25.4	*0.7*	150	-0.2527	0.0180	-6.4193
25.4	*1.4*	37.5	-0.0127	0.0000	-0.6243
25.4	*1.4*	75	-0.0227	0.0006	-1.2237
25.4	*1.4*	150	-0.0346	0.0000	-2.0124

It is clear that the defect thickness has a significant influence on the characteristics. As is discussed in section 5.5 and on the previous page, the thickness of foils and tapes that may be accidentally included in a CFRP laminate during production is known. Therefore the areas in Figure 6.5 can be corrected with the corresponding thickness for each type of foil and tape used in a certain production environment. In a MRO environment, the defect thickness is not known making the defect thickness a parameter that creates a range of uncertainty in the characteristics with a similar trend as the defect depth. This results in similar thermography results for a thinner but shallower located defect and a thicker but deeper located defect.

6.7 Summary

In this chapter three characteristics are identified in the data obtained from a pulse compression analysis thermography measurement; the peak value, the peak delay time and the CC phase. The value of these characteristics is based on the difference in values between a defect and a non defect region. The influence of all factors and their parameters from Figure 3.1 on the three characteristics is determined by varying the parameters OFAT using numerical simulations.

The factors are split in two categories, the first consists of the factors that can be influenced by the operator; the heat signal, the lamps and the camera. Different heat signals have been tested experimentally. The linear chirp resulted in the highest SNR. A linear chirp signal with a frequency range from 1 to 0.01 Hz and a duration of 250 s has been used to determine the influence of the other parameters on the characteristics using numerical simulations. The experiments failed to detect glass coated teflon inserts at 1.4 mm and deeper due to the limited difference in thermal properties with respect to the CFRP material. The lamps and the camera limit the detectability of deeper defects and defects with similar thermal properties to the CFRP material such as teflon coated glass. However the lamps and the camera do not influence the magnitude of the characteristics.

The second category consists of the factors that can not be influenced by the operator; the surface, the material and the defect. These factors have a significant influence on the three characteristics. The surface influences only the SNR but the coating thickness influences the characteristics. The coating thickness can however be determined and corrected for.

The CFRP material thermal properties can vary largely depending on the manufacturing process and the constituents. This spread in properties results in a large spread in the possible values of the characteristics for a certain defect type. Different types of defect materials have been simulated in combination with the outer ranges of the CFRP material properties.

The resulting values of the characteristics are overlapping for all three defects due to the spread in CFRP material properties. The magnitude of the characteristics increases with an increasing difference in thermal properties between the defect and the CFRP material. The defect depth and defect thickness however have a similar influence on the magnitude of the characteristics. Therefore making a decisive conclusion on the defect material, depth and thickness is not possible without knowledge on the CFRP material properties and the potential defect materials since multiple different defects can results in the same values of the characteristics.

6.8 Conclusion

The decisiveness of the pulse compression analysis thermography results on the defect properties is limited. In a production environment the thickness and thermal properties of all tapes and foils are known. This does however not result in decisive characterisation of a defect in the lower regions of the characteristics since all defect materials can have small values for the characteristics, although for defects with properties that differ more from the CFRP material properties have to be located deeper or be thinner in order to result in small values of the characteristics.

In a MRO environment the thickness of a defect (air filled delamination) can vary. This makes characterisation of the defect using pulse compression analysis thermography in MRO not possible without knowledge on the CFRP material properties.

In both environments (production and MRO), the main source of the indecisiveness on defect characters is the spread in the CFRP material properties. Therefore more knowledge on these properties would result in a more decisive characterisation.

Chapter 7: Conclusion

This research shows that it is possible to determine defect characters with optical thermography. Therefore allowing optical thermography to be applied as a NDT method without the need of additional NDT techniques for more detailed inspections.

The spread in potential CFRP material properties on the thermography results is of significant influence on the defect characterisation capabilities. This spread results in overlapping thermography results for different types of defects, limiting the decisiveness of the defect characterisation.

The three different types of defects investigated in this research show different thermography results due to the difference in material properties of the defects. Deeper located defects and defects with properties similar to the CFRP are harder to detect with optical thermography due to the dissipative nature of heat transfer. Also the characterisation capabilities of thermography are better for shallower defects with properties that differ a lot with respect to properties of the CFRP material. The best detectable and characterizable defects are air filled delaminations since the properties vary largely from the CFRP properties. Teflon coated glass inclusions in the composite are harder to detect since the material properties of teflon coated glass are relatively similar to the CFRP properties.

The noise is significant for harder to detect defects such as teflon coated glass inserts. It is found that the noise is decreased by increasing the lamp power used to deposit heat on the test object surface. The thermography method also influences the noise. The SNR obtained with pulse compression analysis thermography is significantly larger than the SNR obtained with frequency domain analysis.

The defect characterisation with frequency domain analysis thermography can be performed based on the blind frequency and the peak phase difference characteristics. These two characteristics in combination with knowledge on the potential defect materials and defect thickness can give a defect depth range and potentially a conclusion on the type of material included depending on the similarity between the potential materials. Without the knowledge on defect thickness and potential defect materials in a MRO environment, the characterisation is still possible since the blind frequency only changes marginally with varying air filled delamination thickness.

The defect characterisation with pulse compression analysis thermography, based on the normalized peak correlation value and the CC phase, results in undistinguishable results for different types of defects at different depths. This makes it difficult to make a decisive conclusion on the defect characters with pulse compression analysis thermography.

Concluding, it can be stated that the best suited thermography method for defect characterisation is frequency domain analysis thermography with a low peak power, long duration heat signal. A defect characterisation with frequency domain analysis consists of five steps. The first step is to perform measurements on the object with suspected damage at multiple different frequencies. The second step is localization of the defects by manually analyzing the phase images obtained from the measurement. From the phase images, the phase difference between a defect and the non defect region surrounding the defect can be obtained. The third step is finding the trend in the phase difference data as a function of the frequency to approximately determine the blind- and the peak phase frequency. The fourth step is performing measurements around the expected blind- and peak phase frequency respectively. Finally, the blind frequency and the peak phase difference can be obtained and used to determine the depth range and the type of defect with the results from this report. The lateral defect size can be determined from the phase image obtained with the peak phase difference.

Chapter 8: Recommendations

A basis for defect characterisation with optical thermography has been set up in this research. However there are a number of subjects that could potentially increase the defect characterisation capabilities of optical thermography:

- The greatest obstacle for characterisation of a defect with optical thermography are accurate composite material properties. The range of these properties is so large that it heavily influences the characterisation capabilities of thermography. Fast and easy to perform one-sided measurement of the thermal diffusivity α and thermal effusivity e would increase the characterisation capabilities of thermography. A method that can be applied to determine the thermal diffusivity α is the single side flash method [81]. This method does require flash lamps. Alternative methods might be applicable.
- The thickness of air filled delaminations needs to be investigated to determine whether the simulated values of 37.5, 75 and 150 µm are representative for real defects. Obtain samples with real delaminations or gas pockets and determine the thickness of these delaminations. This might require destructive testing. Air filled delaminations with a thickness of more than 6.4 µm are represented accurately with the Fourier's heat law, thinner defects are influenced by the temperature jump effect.
- The difference in results with different heat signals in pulse compression analysis shows the influence of this signal. More work could be put into determining the optimum signal parameters for the cross correlation signals used for pulse compression analysis thermography measurements on CFRP materials.
- The source of noise in experiments can be further investigated as it influences the detectability of harder to detect defects.
- The validation of the simulation model in this research is based on the processed data. By calibrating the IR camera for the temperature range of 20 to 40 °C, a more direct validation of the simulation model could be performed.

References

[1] Royal Netherlands Aerospace Centre. *History - NLR*. URL: https://www.nlr.org/about-us/history/.

[2] PhD A. Fahr. *Aeronautical applications of non-destructive testing*. DEStech Publications, Inc., 2014. Chap. 9. ISBN: 978-1-60595-120-1.

[3] E. Phil and C. Soutis. *Polymer composites in the aerospace industry*. 50. Elsevier, 2014.

[4] R.H. Bossi. *ASNT Industry Handbook: Aerospace NDT*. The American Society for Nondestructive Testing, Inc., 2014. ISBN: 978-1-57-57117-339-3.

[5] R. Slayton and G. Spinardi. "Radical innovation in scaling up: Boeing's Dreamliner and the challenge of socio-technical transitions". In: *Technovation* 47 (2016), pp. 47–58.

[6] V.V. Silberschmidt. *Dynamic deformation, damage and fracture in composite materials and structures*. Woodhead Publishing, 2016.

[7] S. Nguyen et al. "Low, medium and high velocity impact on composites". In: *16th International Conference on Composite Structures*. 2013.

[8] J. Bieniaś et al. "Low-energy impact behaviour and damage characterization of carbon fibre reinforced polymer and aluminium hybrid laminates". In: *Archives of Civil and Mechanical Engineering* 15.4 (2015), pp. 925–932.

[9] B. Vieille, V.M. Casado, and C. Bouvet. "About the impact behavior of woven-ply carbon fiber-reinforced thermoplastic-and thermosetting-composites: a comparative study". In: *Composite structures* 101 (2013), pp. 9–21.

[10] T. Rice D. Roach S. Neidigk. *Inspection Options for Detecting Various Types ofImpact Damage in Composite Structures*. 2013.

[11] C. Fauldes and E. Morteau. *Composites @ Airbus, Damage Tolerance Methodology, Presentation at the FAA Workshop for Composite Damage Tolerance and Maintenance*. July 19-21, 2006.

[12] Deparment for Business Innovation and Skills. *BIS RESEARCH PAPER NUMBER 275, UK Aerospace Maintenance, Repair, Overhaul and Logistics Industry Analysis*. 2016.

[13] Harry A Kinnison and Tariq Siddiqui. *Aviation maintenance management*. 2012.

[14] Transport Studies Group University of Westminster London. *Innovative Cooperative Actions of R&D in EUROCONTROL Programme CARE INO III - Technical Discussion Document 9.0*. 2008.

[15] P.V. Kassel. *3D optical scanning for fast and accurate hail damage assessment*. 2014.

[16] S. Kappert. "Multi-domain inspection technique for composite aerostructures". MA thesis. Hanze University of Applied Science Groningen, June 2019.

[17] D. Wu et al. "Lock-in thermography for nondestructive evaluation of aerospace structures". In: *NDT.net* 3.9 (1998).

[18] C. Meola and G.M. Carlomagno. "Recent advances in the use of infrared thermography". In: *Measurement science and technology* 15.9 (2004), R27.

[19] V.S. Ghali, R. Mulaveesala, and M. Takei. "Frequency-modulated thermal wave imaging for non-destructive testing of carbon fiber-reinforced plastic materials". In: *Measurement Science and Technology* 22.10 (2011), p. 104018.

[20] R. Mulaveesala and S. Venkata Ghali. "Coded excitation for infrared non-destructive testing of carbon fiber reinforced plastics". In: *Review of Scientific Instruments* 82.5 (2011), p. 054902.

[21] D. Atkins. *Infrared Spectrum*. [Online; accessed February 25, 2019]. 2013. URL: https://openei.org/wiki/File:Infrared_Spectrum.PNG.

[22] M. Bahrami. *E&CE 309*. 2005. Chap. 12: Radiation heat transfer.

[23] X.P.V. Maldague. *Theory and practice of infrared technology for nondestructive testing*. John Wiley & sons, inc., 2001. ISBN: 0-471-18190-0.

[24] R.D. Hudson. *Infrared system engineering*. Vol. 1. Wiley-Interscience New York, 1969.

[25] R.D. Parker. "Thermic balance or radiometer." In: (1914). United States patent US 1,099,199.

[26] G.A. Barker. "Apparatus for detecting forest fires". In: (1934). United States patent US 1,958,702.

[27] P. Vernotte. "La mesure du coefficient d'arrachement thermique des isolants par la méthode du touchau". In: (1937).

[28] R. Naughton. *the PIONEERS. Aviation and Aeromodelling - Interdependent Evolutions and Histories*. 2004. URL: `http://www.ctie.monash.edu.au/hargrave/tihanyi.html`.

[29] P. Wahl: Instrumentation group. *The Evolution of Thermal Imaging Cameras*. 2007.

[30] *FLIR Company History*. URL: `https://www.flir.eu/about/company-history/`.

[31] Maskim (user). *Atmosfaerisk spredning*. [Online; accessed February 25, 2019]. 2006. URL: `https://commons.wikimedia.org/wiki/File:Atmosfaerisk_spredning.png`.

[32] E. Marín. "Thermal wave physics: principles and applications to the characterization on liquids". In: *RECEN-Revista Ciências Exatas e Naturais* 6.2 (2004), pp. 145–169.

[33] J. Opsal. *FUNDAMENTALS OF THERMAL WAVE PHYSICS*. Therma-Wave, Inc., 1987.

[34] A. Salazar. "Energy propagation of thermal waves". In: *European journal of physics* 27.6 (2006), p. 1349.

[35] E. Marín, L.S. Vaca-Oyola, and O. Delgado-Vasallo. "On thermal waves' velocity: some open questions in thermal waves' physics". In: *Revista mexicana de física E* 62.1 (2016), pp. 1–4.

[36] R. Montanini and F. Freni. "Non-destructive evaluation of thick glass fiber-reinforced composites by means of optically excited lock-in thermography". In: *Composites Part A: Applied Science and Manufacturing* 43.11 (2012), pp. 2075–2082.

[37] G. Busse. "Lockin-Thermography: Principles, NDE-applications, and trends". In: *Qirt 2014 Proceedings* (2014).

[38] B. Bonev A. Stoynova. "Practical Consideration for Lock-in Thermography Effective Spatial Resolution". In: *WSEAS TRANSACTIONS on ELECTRONICS* 8 (2016).

[39] R. Arndt. "Square pulse thermography in frequency domain". In: *Proceedings of SPIE - The International Society for Optical Engineering* 6939 (Mar. 2008). DOI: `10.1117/12.777697`.

[40] M. Choi et al. "Quantitative determination of a subsurface defect of reference specimen by lock-in infrared thermography". In: *Ndt & E International* 41.2 (2008), pp. 119–124.

[41] G. Giorleo, C. Meola, and A. Squillace. "Analysis of defective carbon-epoxy by means of lock-in thermography". In: *Journal of Research in Nondestructive Evaluation* 12.4 (2000), pp. 241–250.

[42] S. Ekanayake, S. Gurram, and R.H. Schmitt. "Depth determination of defects in CFRP-structures using lock-in thermography". In: *Composites Part B: Engineering* 147 (2018), pp. 128–134.

[43] F. Wagner et al. "Analysis of Thermal Diffusivity of Metals using Lock-in Thermography". In: (2016).

[44] W. Bai and B.S. Wong. "Evaluation of defects in composite plates under convective environments using lock-in thermography". In: *Measurement science and technology* 12.2 (2001), p. 142.

[45] K. Chatterjee and S. Tuli. "Prediction of blind frequency in lock-in thermography using electro-thermal model based numerical simulation". In: *Journal of Applied Physics* 114.17 (2013), p. 174905.

[46] G. Busse and A. Rosencwaig. "Subsurface imaging with photoacoustics". In: *Applied Physics Letters* 36.10 (1980), pp. 815–816.

[47] G. Busse. "Optoacoustic and photothermal material inspection techniques". In: *Applied optics* 21.1 (1982), pp. 107–110.

[48] R.L. Thomas et al. "Subsurface flaw detection in metals by photoacoustic microscopya". In: *Journal of Applied Physics* 51.2 (1980), pp. 1152–1156.

[49] R. Mulaveesala and S. Tuli. "Implementation of frequency-modulated thermal wave imaging for non-destructive sub-surface defect detection". In: *Insight-Non-Destructive Testing and Condition Monitoring* 47.4 (2005), pp. 206–208.

[50] R. Mulaveesala, J.S. Vaddi, and P. Singh. "Pulse compression approach to infrared nondestructive characterization". In: *Review of Scientific Instruments* 79.9 (2008), p. 094901.

[51] N. Tabatabaei, A. Mandelis, and B.T. Amaechi. "Thermophotonic radar imaging: An emissivity-normalized modality with advantages over phase lock-in thermography". In: *Applied Physics Letters* 98.16 (2011), p. 163706.

[52] R. Mulaveesala, V.S. Ghali, and V. Arora. "Applications of non-stationary thermal wave imaging methods for characterisation of fibre-reinforced plastic materials". In: *Electronics Letters* 49.2 (2013), pp. 118–119.

[53] J.A. Siddiqui et al. "Infrared thermal wave imaging for nondestructive testing of fibre reinforced polymers". In: *Experimental Mechanics* 55.7 (2015), pp. 1239–1245.

[54] R. Mulaveesala and S. Tuli. "Digitized frequency modulated thermal wave imaging for nondestructive testing". In: *Materials Evaluation* 63.10 (2005).

[55] G. Dua and R. Mulaveesala. "Thermal wave imaging for non-destructive testing and evaluation of reinforced concrete structures". In: *Insight-Non-Destructive Testing and Condition Monitoring* 60.5 (2018), pp. 252–256.

[56] G. Dua and R. Mulaveesala. "Applicability of active infrared thermography for screening of human breast: a numerical study". In: *Journal of biomedical optics* 23.3 (2018), p. 037001.

[57] R.Y. Chiao and X. Hao. "Coded excitation for diagnostic ultrasound: A system developer's perspective". In: *IEEE transactions on ultrasonics, ferroelectrics, and frequency control* 52.2 (2005), pp. 160–170.

[58] M. O'Donnell. "Coded excitation system for improving the penetration of real-time phased-array imaging systems". In: *IEEE transactions on ultrasonics, ferroelectrics, and frequency control* 39.3 (1992), pp. 341–351.

[59] G.V. Subbarao and R. Mulaveesala. "Quadratic frequency modulated thermal wave imaging for non-destructive testing". In: *Progress In Electromagnetics Research* 26 (2012), pp. 11–22.

[60] R. Mulaveesala and S. Tuli. "Theory of frequency modulated thermal wave imaging for nondestructive subsurface defect detection". In: *Applied Physics Letters* 89.19 (2006), p. 191913.

[61] Qianzhu Shi et al. "Barker-coded modulation laser thermography for CFRP laminates delamination detection". In: *Infrared Physics & Technology* 98 (2019), pp. 55–61.

[62] F. Wang, O. Liu J.and Mohummad, and Y. Wang. "Experimental Study on GFRP surface cracks detection using truncated-correlation photothermal coherence tomography". In: *International Journal of Thermophysics* 39.4 (2018), p. 49.

[63] Q. Shi et al. "Study on the detection of CFRP material with subsurface defects using barker-coded thermal wave imaging (BC-TWI) as a nondestructive inspection (NDI) tool". In: *International Journal of Thermophysics* 39.8 (2018), p. 92.

[64] V. Arora et al. "Digitised Frequency Modulated Thermal Wave Imaging for Non-destructive Testing and Evaluation of Glass Fibre Reinforced Polymers". In: *Nondestructive Testing and Evaluation* 34.1 (2019), pp. 23–32. DOI: 10.1080/10589759.2018.1546304. eprint: https://doi.org/10.1080/10589759.2018.1546304. URL: https://doi.org/10.1080/10589759.2018.1546304.

[65] T. Tian. "Anisotropic thermal property measurement of carbon-fiber/epoxy composite materials". In: (2011).

[66] M. Villière et al. "Experimental determination and modeling of thermal conductivity tensor of carbon/epoxy composite". In: *Composites Part A: Applied Science and Manufacturing* 46 (2013), pp. 60–68.

[67] W.P. Adamczyk, S. Pawlak, and Z. Ostrowski. "Determination of thermal conductivity of CFRP composite materials using unconventional laser flash technique". In: *Measurement* 124 (2018), pp. 147–155.

[68] M. Srinivasan et al. “Out of plane thermal conductivity of carbon fiber reinforced composite filled with diamond powder”. In: *Open Journal of Composite Materials* 6.02 (2016), p. 41.

[69] MatWeb Material property data. *Overview of materials for Epoxy/Carbon Fiber Composite*. URL: http://www.matweb.com/search/datasheet.aspx?matguid=39e40851fc164b6c9bda29d798bf3726.

[70] W. Swiderski. “NONDESRUCTIVE TESTING OF COMPOSITE MATERIALS FOR MILITARY APPLICATIONS BY IR THERMOGRAPHY METHODS”. In: ().

[71] R. Joven et al. “Thermal properties of carbon fiber-epoxy composites with different fabric weaves”. In: *SAMPE, Charleston, SC* (2012).

[72] D.M. Price and M. Jarratt. “Thermal conductivity of PTFE and PTFE composites”. In: *Thermochimica acta* 392 (2002), pp. 231–236.

[73] DuPont. *DUPONT KAPTON Summary of properties*.

[74] V.P. Vavilov. “Physical Basics of Thermal Techniques of Nondestructive Evaluation”. In: *Handbook of Advanced Non-Destructive Evaluation* (2018), pp. 1–21.

[75] S. Huth et al. “Lock-in IR-thermography-A novel tool for material and device characterization”. In: *Diffusion And Defect Data Part B Solid State Phenomena*. Citeseer. 2002, pp. 741–746.

[76] Hexcel Corporation. *HexPly M18/1 180°C curing epoxy matrix*. 2015.

[77] 2017 Dassault Systemes. *Abaqus CAE 2018*. Version 2017-11-07 - 18.21.41 127140.

[78] C.V. Madhusudana. *Thermal contact conductance*. Springer, 1996.

[79] The Boeing Company. *Painting versus Polishing of Airplane Exterior Surfaces*. URL: https://www.boeing.com/commercial/aeromagazine/aero_05/textonly/fo01txt.html.

[80] P. Hammond. “On resolution, accuracy and calibration of digital ultrasonic thickness gauges”. In: *NDTnet-The e-Journal of Nondestructive Testing* 2.10 (1997).

[81] F. Cernuschi et al. “Comparison of thermal diffusivity measurement techniques”. In: *Quantitative InfraRed Thermography Journal* 28 (2002), pp. 211–221.

[82] Xavier E. Gros Ph.D. *Applications of NDT data fusion*. Kluwer Academic Publishers, 2001. ISBN: 0-7923-7412-6.

[83] Ph.D. Rick S. Blum Ph.D. Zheng Liu. *Multi-Sensor Image Fusion and Its Applications*. Taylor & Francis group, 2005. ISBN: 0-8493-3417-9.

[84] G. Ranzuglia et al. “MeshLab as a complete tool for the integration of photos and color with high resolution 3D geometry data”. In: *CAA 2012 Conference Proceedings*. Pallas Publications - Amsterdam University Press (AUP), 2013, pp. 406–416. URL: http://vcg.isti.cnr.it/Publications/2013/RCDCS13.

[85] E.M. Lee. “Geomorphological mapping”. In: *Geological Society, London, Engineering Geology Special Publications* 18.1 (2001), pp. 53–56.

[86] A. Sheffer, E. Praun, K. Rose, et al. “Mesh parameterization methods and their applications”. In: *Foundations and Trends® in Computer Graphics and Vision* 2.2 (2007), pp. 105–171.

[87] N. Pietroni, M. Tarini, and P. Cignoni. “Almost isometric mesh parameterization through abstract domains”. In: *IEEE Transactions on Visualization and Computer Graphics* 16.4 (2010), pp. 621–635.

[88] T. Franken et al. “Minimizing user intervention in registering 2D images to 3D models”. In: *The Visual Computer* 21.8-10 (2005), pp. 619–628.

[89] M. Corsini et al. “Image-to-geometry registration: a mutual information method exploiting illumination-related geometric properties”. In: *Computer Graphics Forum*. Vol. 28. 7. Wiley Online Library. 2009, pp. 1755–1764.

[90] M. Callieri, P. Cignoni, and R. Scopigno. “Reconstructing Textured Meshes from Multiple Range RGB Maps.” In: 2002.

[91] N. Bannai, A. Agathos, and R.B. Fisher. “Fusing multiple color images for texturing models”. In: *Proceedings. 2nd International Symposium on 3D Data Processing, Visualization and Transmission, 2004. 3DPVT 2004.* IEEE. 2004, pp. 558–565.

[92] S. Zhang. “High-resolution, real-time 3-D shape measurement”. PhD thesis. Stony Brook University, May 2005.

[93] M. Abdel. *3D LASER SCANNERS: HISTORY, APPLICATIONS, AND FUTURE*. 2011.

[94] W. Boehler and A. Marbs. “3D scanning instruments”. In: *Proceedings of the CIPA WG* 6 (2002), pp. 9–18.

[95] M. Pieraccini, G. Guidi, and C. Atzeni. “3D digitizing of cultural heritage”. In: *Journal of Cultural Heritage* 2.1 (2001), pp. 63–70.

[96] K. Sharma, S.G. Kim, and M.P. Singh. “An improved feature matching technique for stereo vision applications with the use of self-organizing map”. In: *International Journal of Precision Engineering and Manufacturing* 13.8 (2012), pp. 1359–1368.

[97] GOM GmbH. *Acquisition basic GOM Software 2018 Photogrammetry*. 2018.

[98] Terabee France. *Technology overview - Time-of-Flight principle*. URL: `https://www.terabee.com/time-of-flight-principle/`.

[99] L. Li. “Time-of-flight camera–an introduction”. In: *Technical white paper* SLOA190B (2014).

[100] B. Buttgen et al. “CCD CMOS lock-in pixel for range imaging: Challenges, limitations and state-of-the-art”. In: *1st range imaging research day* (2005), pp. 21–32.

[101] O. Choi M. Hansard S. Lee and R. Horaud. “Time of Flight Cameras: Principles, Methods and Applications”. In: *SpringerBriefs in Computer Science* (2012).

Appendix A: Multi domain inspection

No single NDT technique of method can fully assess the structural integrity of a material or structure. The combined application of multiple NDT methods is widely used. This combination can be done by looking at multiple separate data sources and comparing data manually. However the active fusion of the data is a thoroughly researched subject. In 1999, a section exclusively dedicated to data fusion for NDT was organised at the Progress in Quantitative Nondestructive Evaluation conference (QNDE) [82]. Research on the subject of NDT data fusion has been primarily focussed on combining two dimensional NDT data into two dimensional images with more details and three dimensional depth reconstruction of flaws.

The data fusion of two dimensional NDT data is commonly performed at pixel level. The aim of this data fusion can be to provide additional information about the structural integrity of the material, enhance the interpretation, provide extra defect dimensionality, provide reliable information about defect location and size, reduce noise and increase Probability of Detection (POD) [82].

Several methods are available for the two dimensional data fusion as listed below, no further details will be provided on these methods. For more details, the reader is referred to [23][82][83].

- Maximum amplitude
- Pyramid Transform
- Discrete Wavelet Transform
- Discrete Wavelet Frame
- Pixel level weight averaging
- Artificial neural networks

In the context of this research, multi domain inspection refers to the combination of two dimensional IR data and three dimensional geometry data. No present research has been conducted on this topic specifically for NDT. It is known that the visualisation of information about a component is best understood within the context of the part geometry [82]. Combining the NDT data obtained using thermography with the three dimensional geometry obtained using an optical three-dimensional data acquisition method, results in increased understanding of the information. As mentioned earlier, the capabilities of thermography and optical three dimensional data acquisition methods complement each other nicely resulting in information about surface deviations and information about damages inside the object.

A lot of research has been conducted on combining two and three dimensional in the cultural heritage field, geographical research field, medical visualization and 3D detailing for computer applications [84][85][86]. These applications have in common that a 3D scan is usually combined by high resolution photographs. Combining these two data sets effectively to generate useful and practical information is still one of the most problematic steps in three dimensional data scanning.

One commonly used method for combining this information is to use images as a source of colour information for the 3D surface. Digital photographs are essentially a dataset containing colour values for a certain raster. Three difficulties arise when one tries to combine the datasets. The first difficulty is how to store the colour information. The second difficulty is the photographic alignment while the last is how to deal with multiple candidates for a colour caused by the overlap of certain photographs on the 3D surface. These difficulties are treated in the upcoming paragraphs.

The problem of storing the colour information for a 3D surface effectively is based on the question where to store the information on the 3D surface. Three main methods can be used, the first is per-vertex, the second is per-element and the last is texture mapping. Per-vertex storage of colour information gives each mesh vertex an RGB (or grey scale) value while per-element gives each element an RGB value. Both per-vertex and per-element are very compact methods of storing the data. However both these methods are limited by the resolution of the mesh. These methods therefore only work when the mesh is very fine relative to the resolution of the photograph. A more robust alternative is texture mapping which is independent of the mesh size. Texture mapping however requires a correspondence between points on the 2D photograph and the 3D surface. 3D surfaces acquired by 3D scanning commonly consist of unorganized triangles which makes the parametrization more difficult. Several algorithms and methods have been developed for the parametrization on triangular mesh 3D surfaces [86][87].

The photographic alignment requires several processing steps for correct projection on a 3D surface. Distortion of the lenses, focal length, camera position and orientation. Several algorithms have been derived to align photographs using correspondences between the 3D surface and the photograph and derive the parameters needed [88][89].

The impact of discontinuities at overlapping images depends on the different applications. For NDT purposes, a region of blurred or even incorrect colour display may results in a false detection or undetected defects. It is therefore important to rectify artefacts in the overlapping regions of projected photographs. Common methods for treating the colour information when multiple candidates are available are; using a specific criterion as the orthogonality between the 3D surface and the colour source (the photograph), blending by weighing the contribution of the available sources, colour correction and the use of several algorithms as the Maximum A Posteriori (MAP) probability algorithm [83][90][91].

Several commercial software packages are available to complete a number of the tasks described above. An example of such a software package is the open course MeshLab software which is capable of all the steps described above and can even apply different layers of photographic data on a 3D surface [84].

Appendix B: Optical 3D data acquisition

Manual visual inspection of large surface areas is a time consuming task due to the administrative activities for logging all defects. Using digital data acquisition has the potential to automate these administrative activities by documenting the findings automatically. In order to define surface deviations, a two-dimensional image is not sufficient. To distinguish depth, the human body uses stereo vision. Similar techniques are available to acquire three-dimensional data digitally. Three-dimensional measurements can be obtained using both contact and non-contact techniques. For application in NDT, non-contact techniques are well preferred. Therefore techniques requiring contact with the object are not further evaluated in this report.

Over the past two decades, a lot of technological advances have been made in the field of three-dimensional geometry acquisition [92]. This development led to a range of applications including, amongst other, product design, automotive and milling industry, medical science, civil surveying, reverse engineering, archaeology and dentistry [92][93].

The methods for optical three-dimensional data acquisition and modelling that are applicable to large surfaces can be categorised in the three techniques based on the principle the methods use [92][94][95]. These three categories are discussed in the following three subsections.

B.0.1 Image-based techniques

Using stereo vision, depth information can be retrieved from images, this works similar to the human eyes. The principle is based on the focal length and a known distance between two camera's. With this information, the simplified geometry in Figure B.1a and the known information can in theory be used to determine the position of a certain point that is captured by both cameras using Equation B.1 which after rewriting yields equation Equation B.2 [96]. In the geometry, $P(x, y, z)$ is the position of the point on the surface, C_1 and C_2 are the position of camera 1 and 2 respectively, f is the focal length, B is the distance between the two cameras and x_1 and x_2 are the horizontal positions of the images in camera 1 and 2 respectively. Expansion of these equations to three-dimensions in straightforward and omitted here for clarity. By repeating this process for every common point (pixel) in the field of view of both cameras, a geometry can be obtained. Since real camera lenses create a distortion, calibration is needed for the camera setup. Real difficulties arise, however, in finding the common points on the two images. A commonly used method for solving these difficulties is the projection of structured light as is discussed in subsection B.0.2.

$$\frac{Z+f}{Z} = \frac{x_1 + x_2 + B}{B} \tag{B.1}$$

$$Z = \frac{fB}{x_1 + x_2} \tag{B.2}$$

When a small portion of a geometry is scanned, the absolute position of the geometry cannot be determined using just two cameras. To obtain this information, reference points on or around the object are required. These reference points can be used to combine multiple scans into a single geometry. This method is referred to as photogrammetry. Photogrammetry works by obtaining the positions of the reference points using a high resolution camera. At least three reference points have to be within the field of view of the camera to determine the camera position by triangulation. Several images need to be obtained from different positions with respect to the object as can be seen in Figure B.1b. This yields a three dimensional point cloud containing all the reference marker positions. Using these reference points, the separate surface scans can be combined. A surface scan consists of a finer point cloud that can be polygonised to create a surface mesh. This surface can finally be used for evaluation of the scanned object.

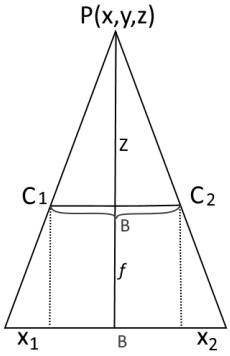

(a) *Simplified stereo vision geometry*

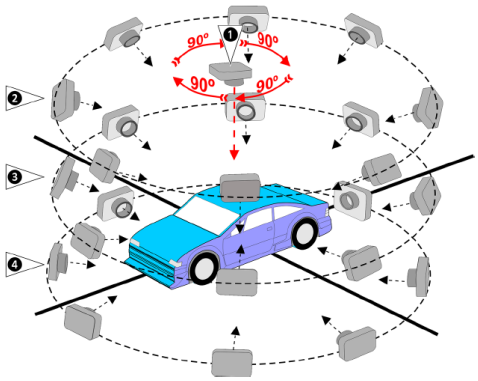

(b) *Photo sequence needed for large object scanning [97]*

Figure B.1: *Image based technique illustrations.*

B.0.2 Structured light scanning techniques

Finding the correspondence between two images used in stereo vision is a fundamental problem. By projecting a certain spatially varying intensity pattern on the surface, this pattern provides the images with easily recognizable features that can be used for the correspondence. This method is referred to as structured light scanning [95]. This pattern theoretically can be used to distract a three-dimensional geometry using only one camera by detecting distortions in the pattern indicating the surface geometry. In practice, using two cameras provides far more accurate measurements. By using two cameras, the distortion of the pattern can be analysed using both cameras separately while also using stereo vision. This effectively provides three simultaneous measurements which can be used to reduce the effect of reflection.

B.0.3 Time-of-Flight based techniques

Time-of-Flight (ToF) is a method that is capable of measuring the distance between the sensor and an object by measuring the time difference between the outgoing signal and the receiving of the reflected signal. Different kind of signals can be used for the ToF principle, the most common are sound and light [98]. In 3D scanning applications the latter is used because of the higher travel speed of the signal. Two types of ToF scanning are possible with a light signal, the first is pulse based scanning and the second is phase based scanning [99][100].

Pulse based scanning sends out a short pulse signal and measures the time between the transmission and the detection. The signal travels the distance between the sensor and the object twice, the distance d can therefore be determined using Equation B.3 in which c is the speed of light [100]. The limitation of this technique is the discrete character of the process.

$$d = \frac{1}{2}ct \tag{B.3}$$

Phase based scanning makes use of a modulated signal to determine the phase difference between the transmitted and the received signal [101]. The phase difference can be converted to a time difference by dividing it by the frequency of the modulated signal. Equation B.3 can then be used to calculate the distance. The phase difference must however be within one period of the modulated signal, limiting the distance of the scanner to the surface and the modulation frequency to prevent ambiguity.

Appendix C: IR Camera specifications

Table C.1: *FLIR SC7600 Infrared Radiation camera specifications.*

Property	**Description**
Sensor model	FLIR SC7600
Sensor serial number	159286
Waveband	Lens, filter, detector combined: 3.4 - 4.9 µm Detector: 1.5 - 5.1 µm Lens: 1.75 - 4.9 µm
Filter bandwidth/spectral bands	BB MWIR filter: 3.42 - 5.15 µm
Detector parameters	Detector material: InSb Aperture F/3 Pitch 15 µm Detector S/N PL0712264 Pixel Clock 40 MHz
Detector resolution (pixels)	640x512 elements
Bit depth per pixel	14 bit (16384 digital levels)
Integration time	20-2500 µm (approximately)
Sample rate	Full frame: 100 Hz 48x4 pixels: up to 3400Hz
Lens focal length	25 mm (FLIR L0709)
Field of view (deg)	21.74x17.45 degree

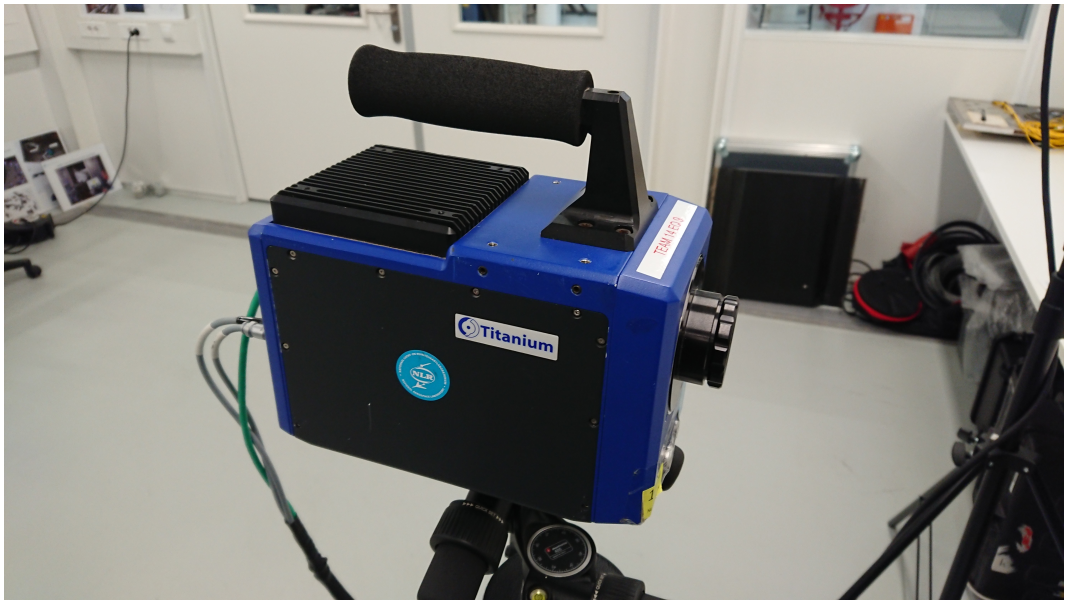

Figure C.1: *The FLIR SC7600 on the camera stand.*

Appendix D: Experimental results pulse compression analysis

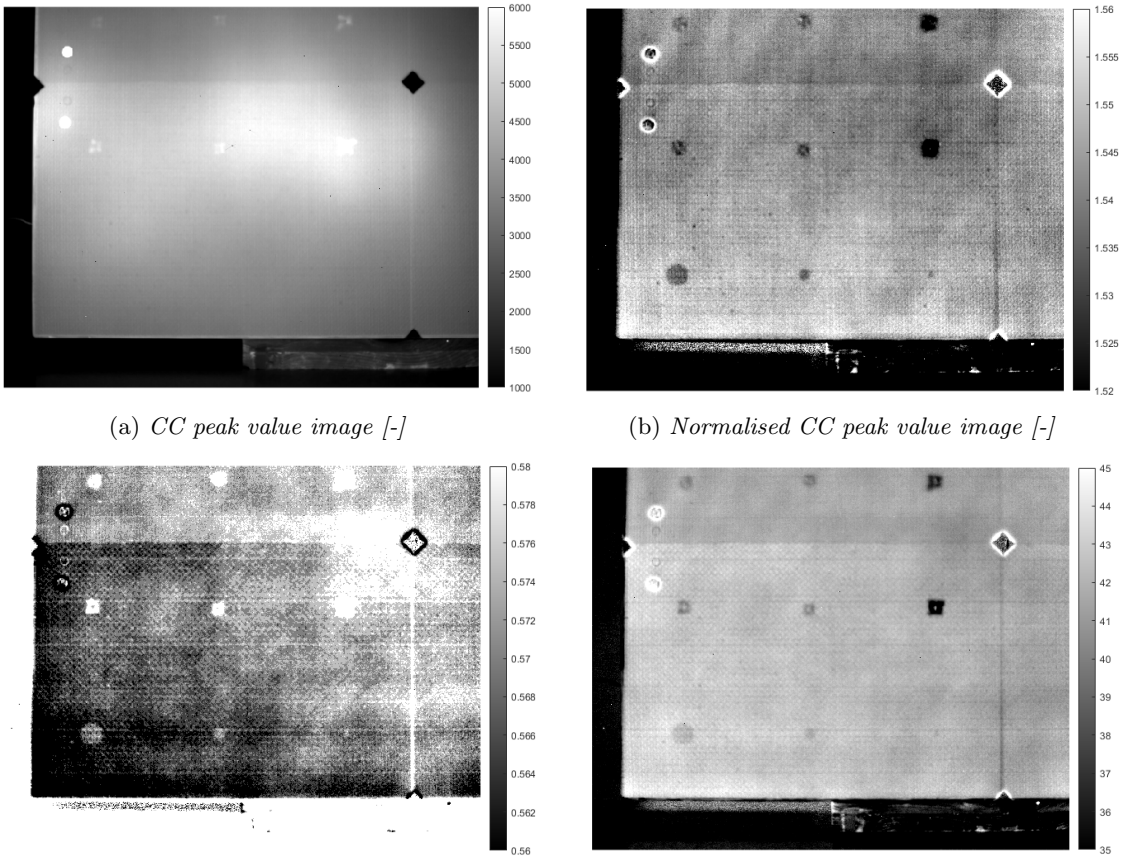

(a) *CC peak value image [-]*

(b) *Normalised CC peak value image [-]*

(c) *Peak delay time image [s]*

(d) *CC phase image [deg]*

Figure D.1: *Experimental results of the NTP-A2 sample with a linear chirp signal (0.5 - 0.05 Hz in 250 s).*

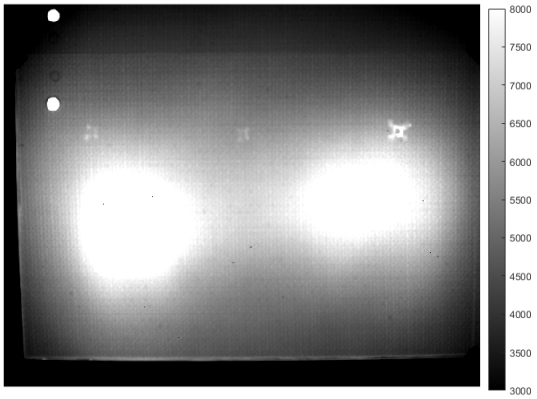

(a) *CC peak value image [-]*

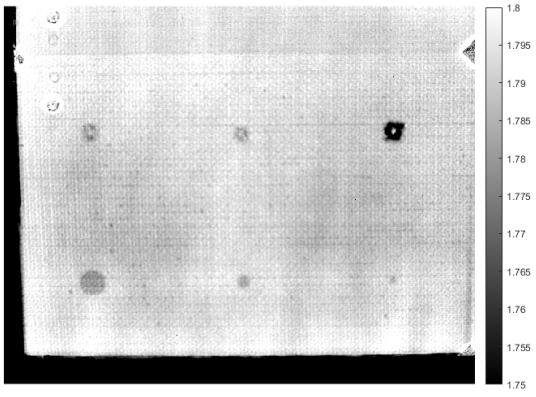

(b) *Normalised CC peak value image [-]*

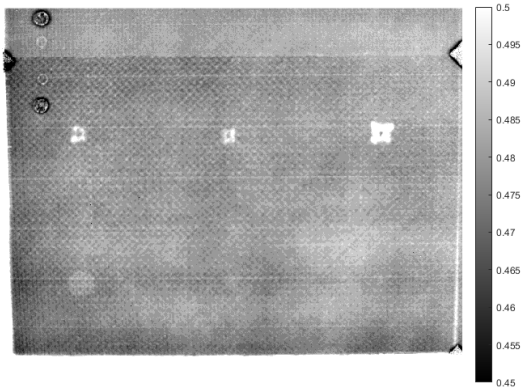

(c) *Peak delay time image [s]*

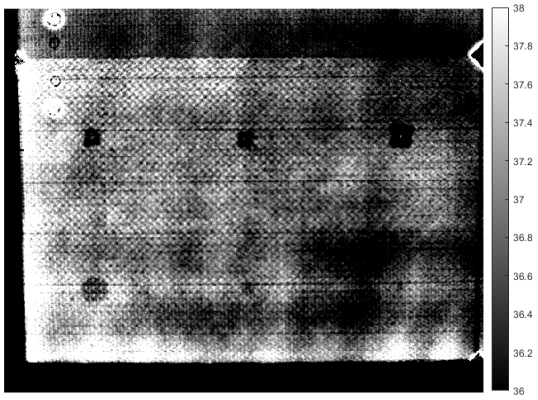

(d) *CC phase image [deg]*

Figure D.2: *Experimental results of the NTP-A2 sample with a quadratic chirp signal (0.5 - 0.05 Hz in 250 s).*

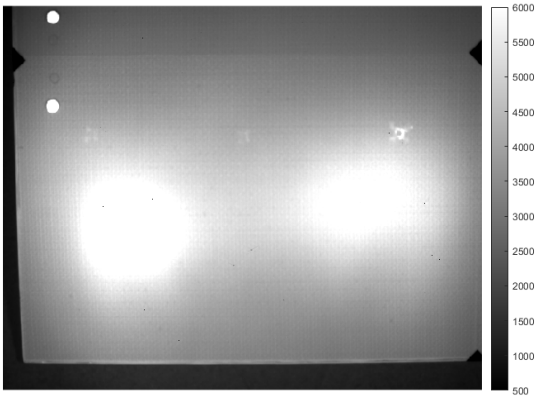

(a) *CC peak value image [-]*

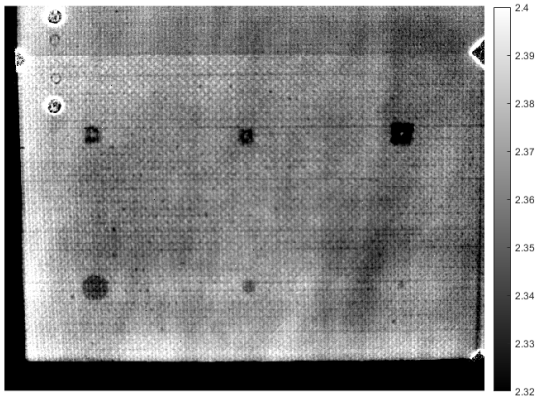

(b) *Normalised CC peak value image [-]*

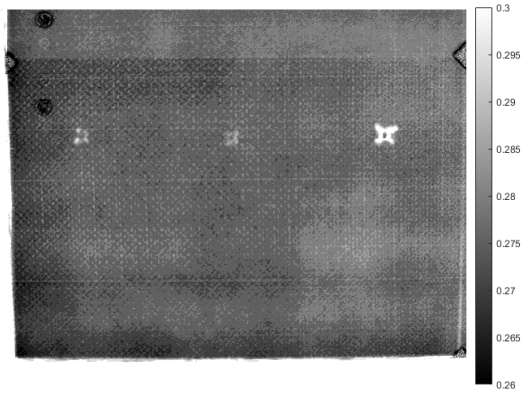

(c) *Peak delay time image [s]*

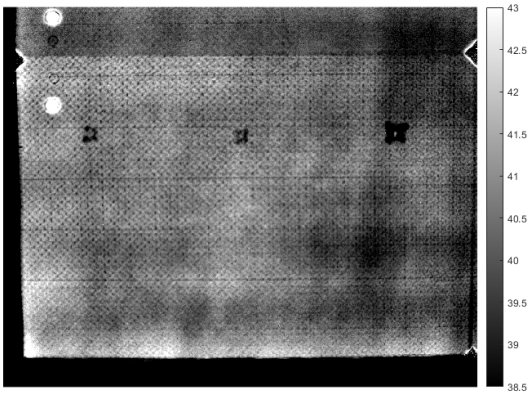

(d) *CC phase image [deg]*

Figure D.3: *Experimental results of the NTP-A2 sample with a quadratic chirp signal (1 - 0.01 Hz in 250 s).*

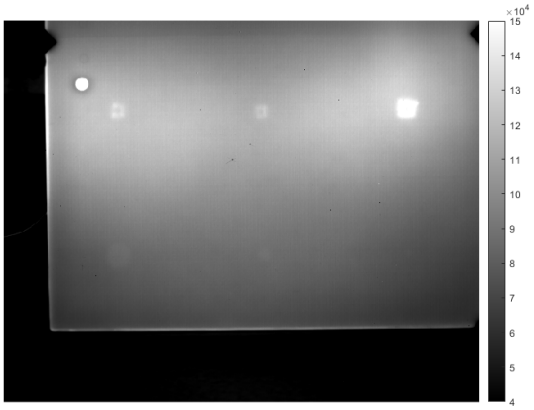

(a) *CC peak value image [-]*

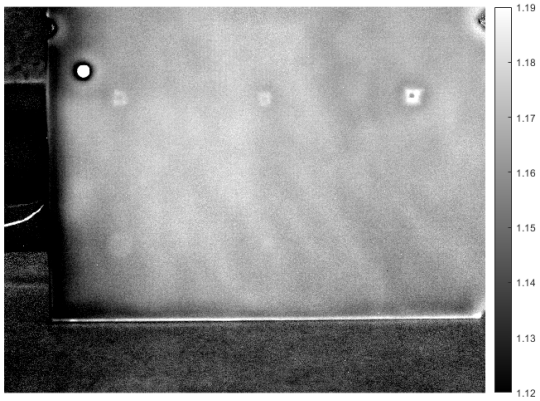

(b) *Normalised CC peak value image [-]*

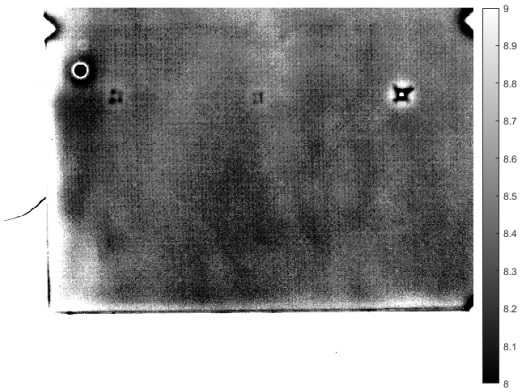

(c) *Peak delay time image [s]*

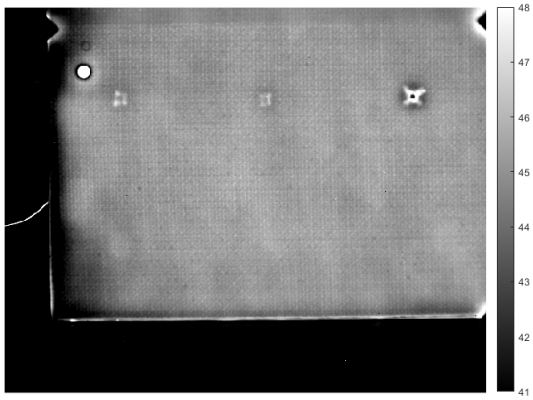

(d) *CC phase image [deg]*

Figure D.4: *Experimental results of the NTP-A2 sample with a 7-bit Barker code signal of 150 s.*

Appendix E: The influence of material parameters on pulse compression analysis thermography

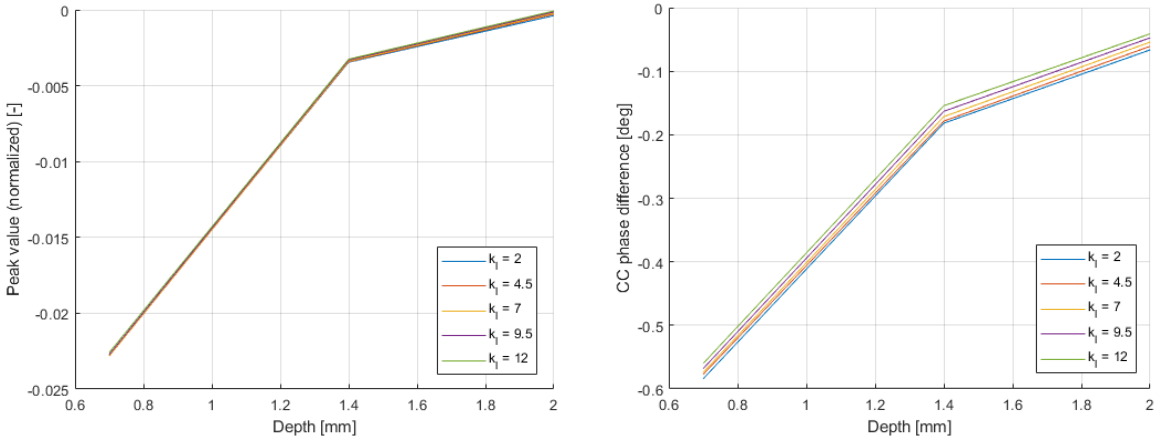

(a) The normalised peak CC value

(b) The CC phase CC_{φ}

Figure E.1: *The influence of the lateral heat conduction k_l on FMTWI results for a 25.4 mm teflon coated glass insert at different depths.*

The influence of the out-of-plane thermal conductivity k_t, the thermal capacity c_p and the mass density ρ of the CFRP material are combined in Figure E.2 and E.3 as a function of the defect depth, thermal diffusivity α and reflection coefficient R. From Figure E.2 it is clear that increasing defect depth results in decreasing characteristic values.

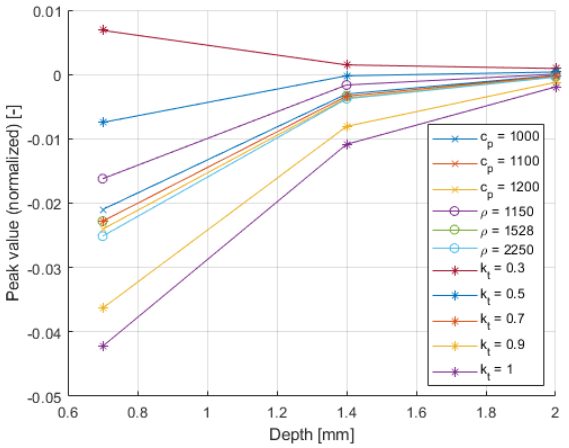

(a) *Peak value*

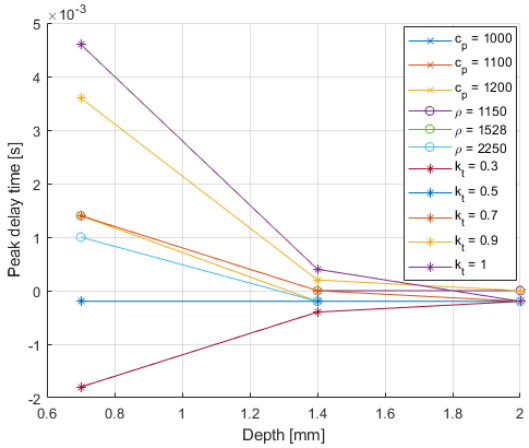

(b) *Peak delay time*

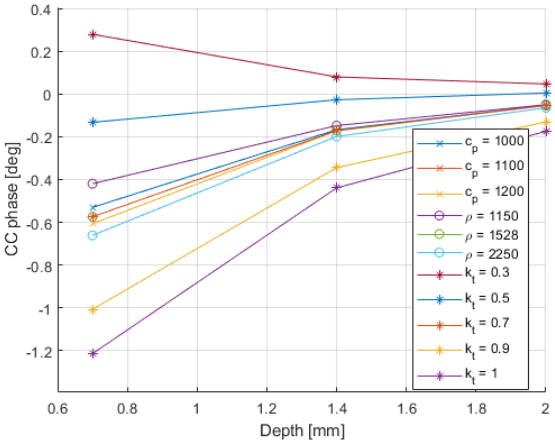

(c) *CC phase*

Figure E.2: *The influence of the out-of-plane thermal conductivity k_t, the mass density ρ and the thermal capacity c_p on the thermography results for a 25.4mm diameter teflon coated glass insert, as a function of the defect depth.*

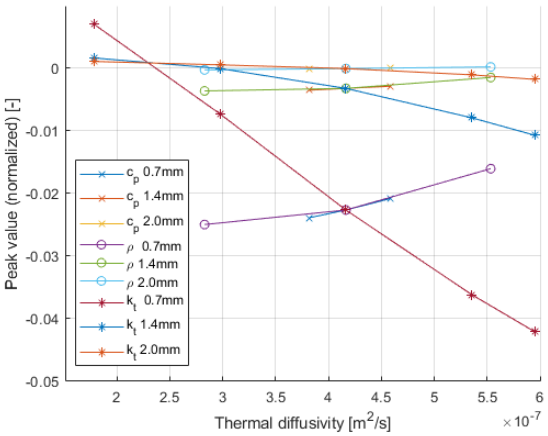

(a) *Peak value*

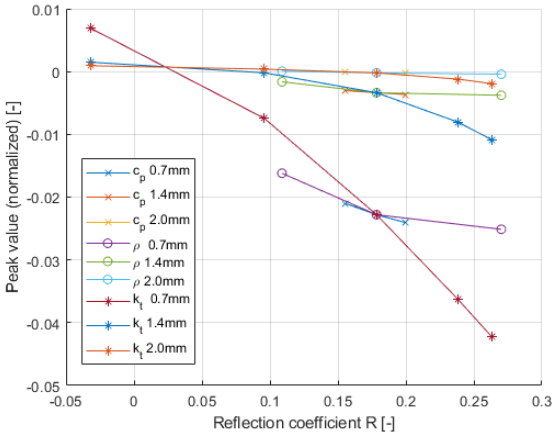

(b) *Peak value*

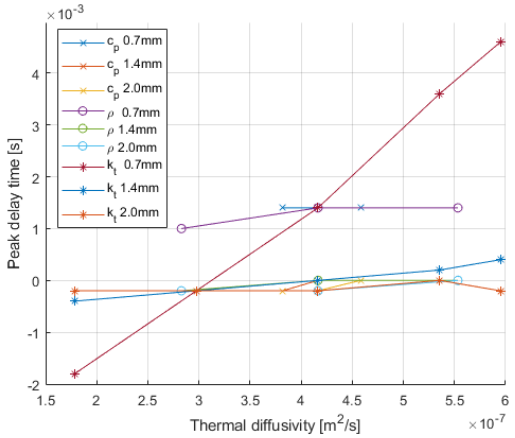

(c) *Peak delay time*

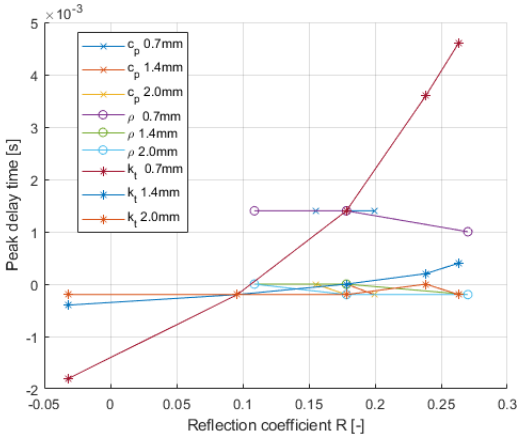

(d) *Peak delay time*

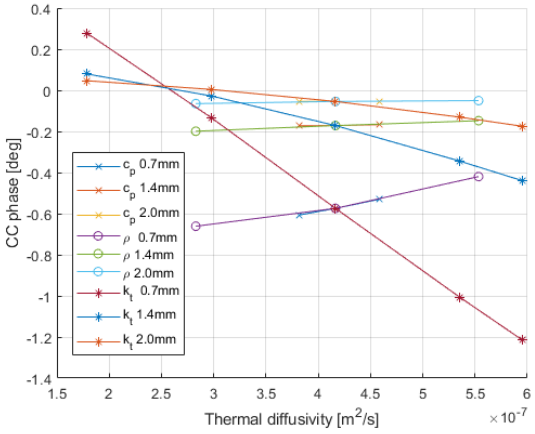

(e) *CC phase*

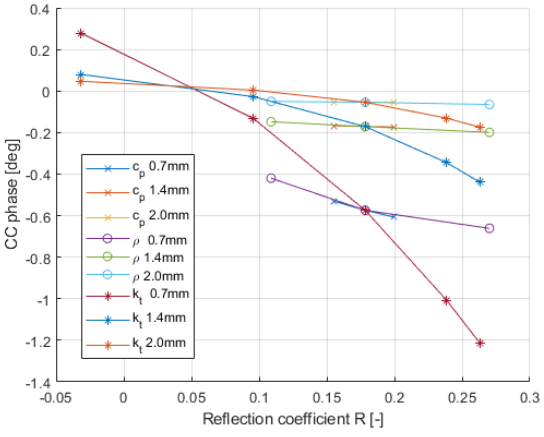

(f) *CC phase*

Figure E.3: *The influence of the through thickness conductivity k_t, mass density ρ and thermal capacity c_p on the thermography results for a 25.4mm teflon coated glass insert, as a function of the thermal diffusivity α_t (a,c and e) and the reflection coefficient R (b,d and f).*